

## Abstract

MARSTON, ZACHARY CLAUDE. An Accessory Device for the Automatic Alignment of Precision Turned Parts on a Vacuum Chuck. (Under the direction of Thomas A. Dow.)

One of the first steps in most machining processes involves aligning the workpiece with respect to the machine used for manufacturing. For a lathe, this usually involves centering the workpiece with respect to the center of rotation by reducing workpiece runout. This centering process is necessary to ensure the desired final shape of the part can be achieved. The manual centering process can be laborious, time-intensive, and prone to human error. Introducing automation into the part alignment process can yield time, labor, and cost savings. Automation is even more beneficial in a glove box machine.

The purpose of this research was to develop an accessory device (Thumper II) that automatically performs the task of part alignment. This device must be compact to fit inside of a turning machine. This device must be able to measure workpiece runout as well as displace the workpiece to reduce runout. Thumper II has been tested for reducing an initial misalignment of up to 1.25 mm to a final misalignment less than 2.5  $\mu\text{m}$ . Thumper II operates with very little operator interaction and no signal connection to the turning machine.

As the spindle rotates at a low constant speed (e.g. 16 RPM), Thumper II measures the runout of the part, locates the eccentricity, and impacts the part in the appropriate location to move it towards the center of rotation. The location and magnitude of the impact is determined by an adaptive algorithm which must account for variables such as friction, vacuum pressure, and part weight. The measurement and impact cycles continue until the workpiece is sufficiently aligned. Thumper II is robust to aligning parts weighing 1-35 lbs over a wide vacuum pressure range. The overall process consistently aligns parts to the desired misalignment target of 2.5  $\mu\text{m}$ . Depending on initial runout and other conditions such as part weight, the process time for Thumper II ranges from 45 seconds to 4 minutes.

An Accessory Device for the Automatic Alignment of Precision Turned Parts on a Vacuum  
Chuck

by  
Zachary Claude Marston

A thesis submitted to the Graduate Faculty of  
North Carolina State University  
in partial fulfillment of the  
requirements for the Degree of  
Master of Science

Mechanical Engineering

Raleigh, NC  
2012

APPROVED BY:

---

Jeff Eischen

---

Paul Ro

---

Thomas Dow  
Advisory Committee Chair

## **Biography**

Zack was born in Charlotte, NC in 1988. He graduated from South Mecklenburg High School in 2006 where he played soccer all four years. He received his BS in Mechanical Engineering from NCSU in December 2010. As an undergraduate he fulfilled a co-op at McKenney's, Inc. in Charlotte, NC and developed an interest in manufacturing, machining, and innovation while working at GreenWave Scientific, Inc. in Raleigh, NC in 2010.

He joined the PEC at NCSU in January 2011 and will receive his MS in Mechanical Engineering in August 2012. Zack has accepted a position at Cree, Inc. in Research Triangle Park and will begin in August 2012.

## **Acknowledgements**

My time at the Precision Engineering Center has been an amazing learning experience for which I am truly grateful. A thank you is duly given to the following people.

*Dr. Thomas Dow, Ken Gerrard, and Alex Sohn:* Their continuous ideas and encouragements were monumental to the success of the project. Thanks to Dr. Dow for pushing me to do my best work and showing me how to be an effective researcher/developer. Thanks to Dr. Dow, Ken, and Alex for teaching me an enormous amount about precision engineering, machining, and computing.

*William Barkman, and Babcock & Wilcox Y-12 Technical Services:* For providing funding for this challenging and rewarding project. Thanks to Bill for constantly checking-in, providing useful ideas and feedback, and pushing me to understand the project at each stage.

*Monica Ramanath:* For continuously assisting in part ordering/delivery and many other day-to-day aspects of the project.

*Steven Furst:* For his work on the successful part alignment project ending in 2008, which provided immense insight into the challenges of automating part alignment, as well as provided inspiration for the successful completion of this project.

# Table of Contents

<b>LIST OF TABLES .....</b>	<b>vi</b>
<b>LIST OF FIGURES .....</b>	<b>vii</b>
<b>LIST OF SYMBOLS, ABBREVIATIONS, NOMENCLATURE .....</b>	<b>x</b>
<b>1. INTRODUCTION.....</b>	<b>1</b>
1.1 BACKGROUND.....	1
1.1.1 <i>Runout on a typical lathe</i> .....	1
1.1.2 <i>Hemispherical workpiece, OC chuck, and IC chuck</i> .....	2
1.1.3 <i>Manual centering process</i> .....	4
1.1.4 <i>Automated centering: Thumper I</i> .....	6
1.1.5 <i>Automated centering: Precitech PCA</i> .....	11
1.2 IMPACT, FRICTION, AND PART MOTION .....	13
1.2.1 <i>Hertz contact</i> .....	13
1.2.2 <i>Modeling friction</i> .....	21
1.2.3 <i>1-D Newton-Hertz-Stribeck (NHS) part motion model</i> .....	27
1.2.4 <i>1D part motion experiments</i> .....	30
1.2.5 <i>2D Newton-Hertz-Stribeck part motion model on vertical OC chuck</i> .....	39
1.2.6 <i>2D part motion experiments</i> .....	46
1.3 PROBLEM DEFINITION FOR THUMPER II DESIGN .....	50
<b>2. THUMPER II: DEVICE DESIGN.....</b>	<b>51</b>
2.1 DEVICE OVERVIEW .....	51
2.2 COMPONENT SELECTION.....	53
2.2.1 <i>Actuator</i> .....	53
2.2.2 <i>Linear ball bearing</i> .....	57
2.2.3 <i>Position Encoder</i> .....	62
2.3 CONSTRUCTION AND INTEGRATING COMPONENTS .....	64
<b>3. THUMPER II: CONTROL SYSTEM DESIGN.....</b>	<b>71</b>
3.1 SYSTEM OVERVIEW .....	71
3.2 COMPONENT SELECTION.....	72
3.2.1 <i>Microcontroller</i> .....	72
3.2.2 <i>Amplifier and Power Supply</i> .....	73
3.2.3 <i>Graphic User Interface</i> .....	76
3.2.4 <i>Thumper II electrical packaging</i> .....	78
<b>4. THUMPER II: OPERATION .....</b>	<b>81</b>
4.1 MEASUREMENT OPERATION & TESTING .....	82
4.1.1 <i>Measurement Overview</i> .....	82
4.1.2 <i>LSC measurement details</i> .....	84
4.1.3 <i>Measurement using TIR versus LSC</i> .....	88
4.1.4 <i>Measurement preload force</i> .....	90
4.1.5 <i>Repeatability of the LSC measurement</i> .....	90
4.1.6 <i>Effect of incorrect spindle speed from operator</i> .....	92
4.1.7 <i>Tip settling time</i> .....	93

4.1.8	<i>Wear of Thumper II tip</i> .....	94
4.2	TAP DYNAMICS AND COIL MOTION .....	99
4.2.1	<i>Understanding coil dynamics in voltage mode</i> .....	100
4.2.2	<i>Effect of bellows during tap</i> .....	103
4.2.3	<i>Tapping scheme with Thumper II</i> .....	106
4.2.4	<i>Tapping frequency – repeatable impacts</i> .....	107
4.3	THE ADAPTIVE TAP ALGORITHM.....	108
4.3.1	<i>Algorithm features: How hard to tap the part</i> .....	109
4.3.2	<i>Algorithm features: Where to tap the part</i> .....	113
4.3.3	<i>How the algorithm features work together</i> .....	119
<b>5.</b>	<b>ALIGNMENT TESTING</b> .....	<b>121</b>
5.1	PART ALIGNMENT TESTING OVERVIEW .....	121
5.2	UNDERSTANDING THE ALIGNMENT PROCESS .....	121
5.3	COMPENSATING FOR DROP ANGLES .....	123
5.4	ALIGNMENT AT VARIOUS VACUUM PRESSURES ON OC AND IC CHUCKS .....	125
5.4.1	<i>Varying vacuum pressures on the OC chuck</i> .....	125
5.4.2	<i>An alignment inefficiency and its solution</i> .....	126
5.4.3	<i>Varying vacuum pressures on the IC chuck</i> .....	127
5.5	ALIGNMENT AT VARIOUS SPINDLE SPEEDS .....	128
5.6	FINAL MISALIGNMENT AND PROCESS TIME .....	129
<b>6.</b>	<b>CONCLUSIONS AND FUTURE WORK</b> .....	<b>130</b>
6.1	OBJECTIVES & SUMMARY .....	130
6.2	RESULTS .....	130
6.3	IMPROVEMENTS AND FUTURE WORK.....	131
	<b>REFERENCES</b> .....	<b>133</b>
	<b>APPENDICES</b> .....	<b>137</b>
	<b>APPENDIX A. PARTS AND CHUCKS USED FOR CENTERING EXPERIMENTS</b> .....	<b>138</b>
	<b>APPENDIX B. MASTER LIST OF CENTERING TESTS</b> .....	<b>140</b>
	<b>APPENDIX C. PARAMETERS USED BY THUMPER II FOR TAPPING</b> .....	<b>143</b>
	<b>APPENDIX D. LINEAR RELATION DATA FOR ADAPTIVE ALGORITHM</b> .....	<b>145</b>
	<b>APPENDIX E. TDVKA TABLES DETAILING AN ALGORITHM INEFFICIENCY</b> .....	<b>148</b>
	<b>APPENDIX F. ENERGY BALANCE EQUATIONS FOR PART MOTION</b> .....	<b>150</b>
	<b>APPENDIX G. SUMMARY OF COMPONENTS FOR THUMPER II</b> .....	<b>153</b>
	<b>APPENDIX H. TABLES FOR SELECTION OF RAIL MASS</b> .....	<b>154</b>
	<b>APPENDIX I. SHOP DRAWINGS FOR THUMPER II STRUCTURE</b> .....	<b>156</b>
	<b>APPENDIX J. ELECTRICAL SCHEMATIC FOR ELECTRICAL ENCLOSURE</b> .....	<b>163</b>
	<b>APPENDIX K. CODE &amp; ADAPTIVE ALGORITHM FLOW CHART</b> .....	<b>164</b>
	<b>APPENDIX L. OPERATE THUMPER II (FROM USER’S MANUAL)</b> .....	<b>166</b>

## List of Tables

Table 1. Key material properties.....	17
Table 2. Sliding distance ( $\mu\text{m}$ ) for simulations with Stribeck friction and Coulomb friction.	30
Table 3. Variation of static friction coefficients with surface condition. ....	31
Table 4. Observation of presliding displacement. ....	34
Table 5. Simulations of drop angle variations. ....	45
Table 6. Variation of drop angle with impact magnitude. ....	48
Table 7. Variation of drop angle with vacuum pressure. ....	49
Table 8. Part displacements for selection of maximum impact velocity (OC chuck at 12 psi). .....	56
Table 9. Thumper II encoder compared with precision DTM axis.....	67
Table 10. Misalignment ( $\mu\text{m}$ ) with LVDT and Thumper II (LSC and TIR) at 8 RPM.....	89
Table 11. Misalignment ( $\mu\text{m}$ ) at different spindle speeds. ....	90
Table 12. Misalignment ( $\mu\text{m}$ ) at different VCA preload forces. ....	90
Table 13. Repeatability of the least-squares circle fit measurement. ....	91
Table 14. Measurement of the effects of incorrect spindle speed.....	93
Table 15. Results from tip wear experiment.....	98
Table 16. Effect of bellows during tap.....	104
Table 17. Effect of vacuum created in bellows during tap. ....	105
Table 18. TDVKA table from an actual alignment process.....	110
Table 19. Drop angle values for two alignments. ....	125
Table 20. Alignment process at various vacuums on the OC chuck. ....	126
Table 21. Alignment process at various vacuums on the IC chuck. ....	127
Table 22. Alignment process time on the OC chuck at varying spindle speeds.....	128
Table 23. Process time (min:sec) and final misalignment. ....	129
Table 24. Parts used in Thumper II testing/development. ....	139
Table 25. Chucks used in Thumper II testing/development. ....	139
Table 26. List of all recorded centering tests.....	140
Table 27. Empirical parameters for performing taps. ....	143
Table 28. Misalignment table for alignment of part 1A on OC chuck at 5.2 psi.....	148
Table 29. TDVKA table corresponding to test in Table 28.....	149
Table 30. List of components used for Thumper II. ....	153
Table 31. Selection of impacting mass: increasing mass increases part displacement.....	155
Table 32. Selection of impacting mass: decreasing mass improves velocity resolution. ....	155

## List of Figures

Figure 1. (a) Full view of CNC lathe and (b) axial view of lathe. ....	2
Figure 2. Workpieces of interest. ....	3
Figure 3. Axial misalignment on the IC chuck and radial misalignment on the OC chuck. ....	4
Figure 4. Construction of an LVDT [1]. ....	5
Figure 5. Set-up for a manual alignment procedure. ....	6
Figure 6. Thumper I - Solution to automated part centering [2]. ....	7
Figure 7. Thumper I actuator construction [2]. ....	8
Figure 8. Free body diagram for impact actuation. ....	9
Figure 9. Experimental set-up for pushing a part [2]. ....	9
Figure 10. Experimental results from pushing a part [2]. ....	10
Figure 11. Precitech “Part Centering Accessory” [3]. ....	12
Figure 12. Hertz contact with two spheres [5]. ....	14
Figure 13. Experimental set-up with plastic impacting tip and load cell. ....	17
Figure 14. Simulated and measured force profiles for three impact velocities. ....	18
Figure 15. Experimental set-up using impact hammer. ....	19
Figure 16. Repeatability of impact hammer force profiles. ....	20
Figure 17. Varying tip material for same impact velocity using impact hammer. ....	21
Figure 18. Diagram of surface asperities [15]. ....	22
Figure 19. Coulomb friction behavior. ....	24
Figure 20. Stribeck curve with dry friction [5]. ....	24
Figure 21. LuGre asperity friction model [17]. ....	25
Figure 22. Friction spring model [2]. ....	26
Figure 23. Free body diagram for impact actuation. ....	27
Figure 24. Simulation of impact, friction, and 1-D part motion. ....	29
Figure 25. Set-up for pulley-mass experiment to determine static friction coefficient. ....	30
Figure 26. Impact hammer and part displacement set-up for 1D sliding. ....	32
Figure 27. Simulated and experimental part displacement and impact force. ....	33
Figure 28. Presliding displacement plot. ....	35
Figure 29. Direction reversal hysteresis with varying surface condition. ....	37
Figure 30. Direction reversal hysteresis with varying vacuum pressures. ....	38
Figure 31. Direction reversal hysteresis with varying impact magnitude. ....	39
Figure 32. 2D part motion free body diagram. ....	40
Figure 33. Simulation of impact, friction, and 2D part motion on OC chuck. ....	42
Figure 34. Basic geometry of the (a) coordinate system and (b) drop angle. ....	44
Figure 35. Experimental set-up for 2D motion measurements. ....	46
Figure 36. 2D sliding path measurement. ....	47
Figure 37. Drop angle variation with impact force. ....	48
Figure 38. Drop angle variation with vacuum pressure. ....	49
Figure 39. Picture and 3D rendering of Thumper II. ....	51
Figure 40. Thumper II automated part alignment device. ....	53
Figure 41. Linear VCA construction [18]. ....	54

Figure 42. Variation of force constant for VCA. ....	57
Figure 43. THK SSR-style caged-ball bearing and rail [19]. ....	58
Figure 44. Rail straightness measurements. ....	59
Figure 45. Simplified diagram of assembly mass acceleration. ....	60
Figure 46. Displacement variation by increasing impacting mass for constant kinetic energy. .....	61
Figure 47. (a) Single line grating and (b) Moiré fringe between two straight-line gratings of same pitch titled with respect to each other [20]. ....	63
Figure 48. Construction of Renishaw’s incremental optical encoder [21]. ....	64
Figure 49. Details of Thumper II construction. ....	65
Figure 50. Guide used in scale installation (a), scale and coil installed on rail (b). ....	66
Figure 51. Thumper II fully retracted and fully extended. ....	68
Figure 52. Construction of bellows. ....	69
Figure 53. Simple bearing resistance test. ....	70
Figure 54. Schematic of Thumper II control system. ....	71
Figure 55. TERN 586-P Microcontroller on top of the TERN P50 expansion board. ....	72
Figure 56. Thumper II GUI screenshot. ....	77
Figure 57. Front panel of electrical enclosure. ....	79
Figure 58. Inside of electrical enclosure. ....	80
Figure 59. Thumper II set-up for alignment on each chuck. ....	81
Figure 60. Shape errors and the LSC method. ....	83
Figure 61. Least-square circle fit method. ....	84
Figure 62. LSC measurement on the OC chuck. ....	85
Figure 63. Raw data of rail position during part measurement. ....	86
Figure 64. Measured points on part surface. ....	87
Figure 65. LSC measurement on the IC chuck. ....	88
Figure 66. Tip settling time with measurement type forces. ....	94
Figure 67. Set-up for tip wear experiment. ....	95
Figure 68. Profilometer trace over worn Acrylic tip. ....	96
Figure 69. Geometry of spherical cap [25]. ....	97
Figure 70. Microscope image of wear areas for (a) Nylon and (b) Acrylic tip. ....	97
Figure 71. Electrical circuit for linear voice coil motor. ....	100
Figure 72. Voltage across coil with amplifier in voltage mode. ....	101
Figure 73. Simulated coil velocity and current at 12V high-step and 8V low-step. ....	102
Figure 74. Measured coil velocity and current at 12V high-step and 8V low-step. ....	103
Figure 75. Impact force with bellows and without bellows installed. ....	104
Figure 76. Impact force with shield and without shield installed. ....	106
Figure 77. Measured position and velocity of coil-rail-tip in voltage mode. ....	107
Figure 78. Multiple impacts per revolution. ....	108
Figure 79. Observed linear displacement-velocity squared relationship. ....	112
Figure 80. Basic geometry of the (a) coordinate system and (b) drop angle. ....	114
Figure 81. Drop angle geometry (a) for tapping highspot and (b) as used in microcontroller. .....	115

Figure 82. Geometry to determine critical drop angle for tapping high spot. ....	117
Figure 83. Flow chart for alignment process. ....	118
Figure 84. Polar plot of center locations during alignment at two part weights on a logarithmic radial scale. ....	122
Figure 85. Thumper II overcoming large drop angle. ....	124
Figure 86. Parts and chucks used for centering experiments. ....	138
Figure 87. High-step and low-step voltages used for impacts. ....	144
Figure 88. Values from actual TDVKA tables for part 2 on the OC chuck at 11.1 psi. ....	145
Figure 89. Values from actual TDVKA tables for part 3A on the IC chuck at 7.1 psi. ....	146
Figure 90. Values from actual TDVKA tables for part 2 on the IC chuck at 11.1 psi. ....	146
Figure 91. Values from actual TDVKA tables for part 3B on the IC chuck at 3.4 psi. ....	147
Figure 92. Energy balance and instantaneous impact model. ....	150
Figure 93. Thumper II setup. ....	166
Figure 94. GUI Step 1. ....	169
Figure 95. GUI Step 2. ....	170
Figure 96. GUI Step 3. ....	171
Figure 97. GUI Step 4. ....	172
Figure 98. GUI Step 5. ....	173

## List of Symbols, Abbreviations, Nomenclature

Symbol	Description
$CE$	Material constant for Hertz theory
$KD$	Geometric constant for Hertz theory
$\nu_1$ and $\nu_2$	Poisson's Ratio
$E_1$ and $E_2$	Elastic Modulus
$d_1$ and $d_2$	Diameter of impacting tip and part
$y$	Center-center approach for Hertz theory
$F_a$	Impact force
$\ddot{x}_{tip}$	Tip acceleration used in finite difference models
$\dot{x}_{tip}$	Tip velocity used in finite difference models
$\dot{x}_{tip0}$	Initial tip velocity used in finite difference models
$\Delta t$	Time duration of a single step in finite difference models
$F_f$	Friction force
$F_s$	Static friction force
$F_k$	Kinetic friction force
$F_e$	External force
$\nu_s$	Rate for Stribeck curve
$N$	Normal force between part and chuck
$\mu$	Friction coefficient
$\mu_s$	Static friction coefficient
$\mu_k$	Kinetic friction coefficient
$\ddot{x}_{part}$	Part acceleration used in finite difference models (x-direction)
$\dot{x}_{part}$	Part velocity used in finite difference models (x-direction)
$x_{part}$	Part position used in finite difference models (x-direction)
$\ddot{y}_{part}$	Part acceleration used in finite difference models (y-direction)
$\dot{y}_{part}$	Part velocity used in finite difference models (y-direction)
$y_{part}$	Part position used in finite difference models (y-direction)
$\phi$	Angle for direction of part motion used in finite difference model
$F_{f,x}$	Friction force used in finite difference model (x-direction)
$F_{f,y}$	Friction force used in finite difference model (y-direction)
$m_{part}$	Mass of part
$v_{tip0}$	Velocity of tip at impact
$\theta_{drop}$	Drop angle
$\theta_c$	Critical drop angle
$m$	Slope of best fit line to part displacement impact velocity squared data
$b$	Intercept of best fit line to part displacement impact velocity squared data
$K_B$	Motor force constant
$K_F$	Motor back EMF constant
$L$	Inductance of motor
$R$	Radius of tip or resistance of motor depending on situation
$V_w$	Wear volume of tip
$h_w$ and $h$	Wear height of tip

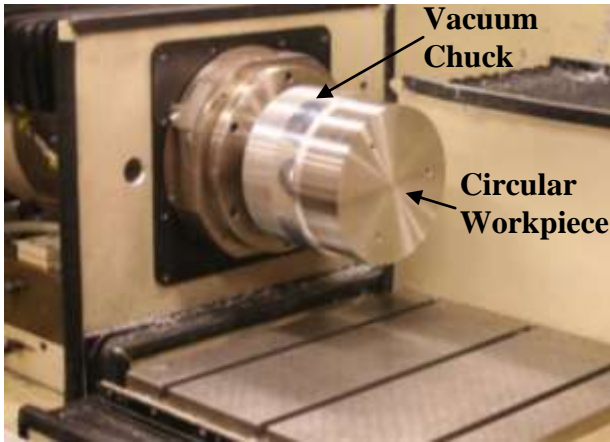
# **1. Introduction**

## **1.1 Background**

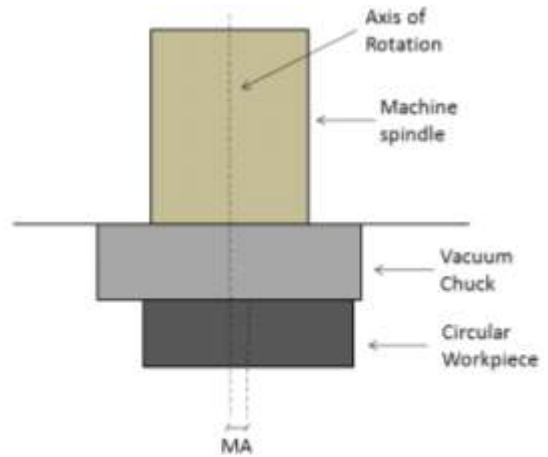
### **1.1.1 Runout on a typical lathe**

One of the first steps in many machining processes involves aligning the workpiece with respect to the machine used for manufacturing. For a lathe, this usually involves centering the workpiece with respect to the center of rotation by reducing workpiece runout. Centering the workpiece by reducing runout is necessary to ensure the desired shape of the part is achieved by the material cutting process.

A lathe with a vacuum chuck installed is seen in Figure 1 (a). A vacuum chuck that is mounted to a machine spindle holds a workpiece by vacuum pressure. Workpiece runout is generally defined as the total apparent radial motion of the workpiece as the spindle is rotated a complete revolution. Runout includes the misalignment of the workpiece as well as the shape of the workpiece. Misalignment on a lathe is illustrated in Figure 1 (b) which shows a circular part on a vacuum chuck. In general, the misalignment value, seen as “MA” in Figure 1 (b), is defined as the distance between the center of the round workpiece and axis of rotation. The runout is twice the misalignment value with the addition of workpiece shape errors.



(a)



(b)

Figure 1. (a) Full view of CNC lathe and (b) axial view of lathe.

While computer numerical control (CNC) machining makes it possible to automate the material removal process, the initial part centering process is typically still manual. The manual process of part alignment can be laborious, time-intensive, and prone to human error. These negative attributes are further exacerbated when a glove box machine environment is of interest.

Introducing automation into the part alignment process can yield time, labor, and cost savings. An automated centering device can be used to transform a partially-automated machine, such as a CNC lathe, into a more automated machine. An automated alignment device also helps to overcome the challenges of operating a machine in a glove box environment while reducing human interaction with the machine.

### 1.1.2 Hemispherical workpiece, OC chuck, and IC chuck

The workpiece of interest for this project is the hemispherical shell (i.e. hemishell). A 6" outer diameter aluminum hemishell with 1/4" wall thickness can be seen in Figure 2 (b). The automated device and system detailed in this thesis is not limited to the alignment of this

workpiece shape. In fact, a wide range of parts have been automatically aligned during this project. These parts are pictured in Figure 86 in Appendix A. The parts used during different tests will be referred to by their part number as given in Table 24 in Appendix A.

The outer contour (OC) and inner contour (IC) chucks can be seen in Figure 2 as well. The OC chuck holds the hemishell while its outer surface is machined, and the IC chuck holds the hemishell while its inner surface is machined. Both chucks hold the part using vacuum pressure.



(a) IC chuck      (b) Hemishell      (c) OC chuck

Figure 2. Workpieces of interest.

Workpiece misalignment has a different geometrical meaning depending on the chuck being used to hold the hemishell. This is indicated in Figure 3 where the “MA” dimension is the misalignment. Figure 3 (a) is a side view cutaway of the IC chuck, and Figure 3 (b) is a front view of the OC chuck. When the hemishell is held by the OC chuck, *radial* misalignment is being corrected. When the part is on the IC chuck, *axial* misalignment is being corrected. Radial misalignment is the more common type encountered in lathes, and the radial runout alignment process by Thumper II will work for most circular cross-section parts. As indicated by Figure 1 and Figure 3, the runout value for a given part is twice the misalignment value.



(a) Side view of IC chuck showing axial misalignment of face of part

(b) Front view of OC chuck showing radial misalignment of part center

Figure 3. Axial misalignment on the IC chuck and radial misalignment on the OC chuck.

It is important to realize that the device only measures the surface of the part and does not contact a fiducial (i.e. reference surface) on the machine. For example, in the radial measurement case the part is not displaced towards the center of a predefined spindle axis, but instead is simply displaced to reduce runout.

### 1.1.3 Manual centering process

The manual process of centering a workpiece on a spindle requires setting up an instrument within the machine to measure part runout. One such instrument often used in precision applications is the Linear Variable Differential Transformer (LVDT) which is pictured in Figure 4. In an LVDT, a magnetic core is attached to a rod outside the main housing which contacts the object being measured (e.g. the workpiece in Figure 1). An AC voltage is sent through the primary coil. As the rod and core displace during measurement, different voltages will be induced in the secondary coils. This voltage difference directly represents the displacement of the core, and the sign of the voltage difference between the two coils indicates the direction of the core and rod from the null (i.e. middle) position.

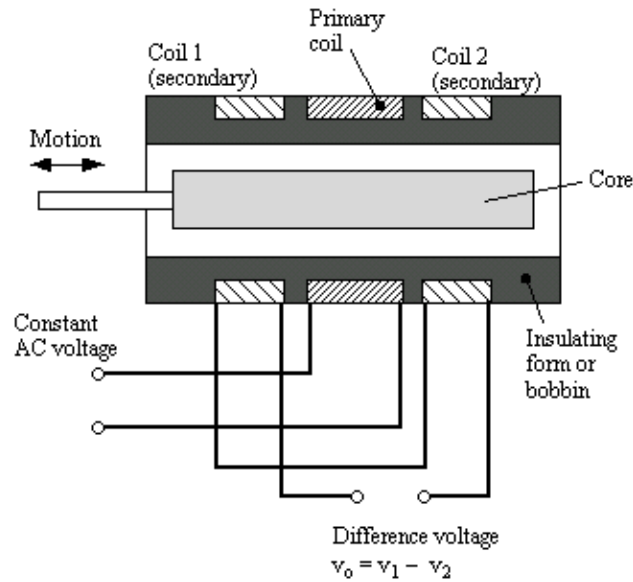


Figure 4. Construction of an LVDT [1].

Figure 5 shows an example of a common manual alignment set-up using a lever-style gage. Similar to the LVDT, displacement is derived by noting the voltage difference between two secondary coil windings in the electronic gage seen in Figure 5. This electromechanical design is known as a shaded pole inductor. The tip of the measurement probe has an involute tip making it possible to measure linear displacement (vertical direction in Figure 5) using a rotating lever arm.

To perform manual centering with this set-up, the operator first puts the part on the chuck and turns on the vacuum pressure. Then, the operator brings the gage into contact with the workpiece and zeros the gage. Then, the gage output is viewed as the spindle is rotated. In the case of Figure 5, the highspot is found to be the place where the gage displacement is at its maximum upward value. Once the highspot is located at the probe tip, the part is tapped just to the side of the probe with a hammer towards the center of rotation as indicated in Figure 5. To obtain micrometer displacements, the workpiece may be tapped with something lighter than a hammer, such as an Allen wrench. This manual process of locating and tapping the highspot is repeated until the workpiece is sufficiently aligned.



Figure 5. Set-up for a manual alignment procedure.

One of the biggest disadvantages of the manual alignment method in precision turning is that it can be time-consuming as it involves setting up an instrument in the machine and taking measurements. This task becomes much more difficult and time intensive if the parts are being machined in a glove box environment. The manual alignment method also requires a trained operator as it is easy to set-up the gage incorrectly and obtain invalid information about workpiece runout. The manual procedure described would not be able to center a part better than the shape error of the part. In other words, if a part is not round then multiple high spots can occur making it impossible to center the part to further precision with the manual procedure. Automating part alignment is advantageous as it offers potential time and cost savings while helping to eliminate human error.

#### **1.1.4 Automated centering: Thumper I**

Considerable research and development regarding automated part alignment techniques has already taken place. A device (Thumper I) developed by Furst [2] and a commercial product

from Precitech [3] show that part alignment on a vacuum chuck can be automated. Both techniques are able to correct misalignment of precision parts to less than 2.5  $\mu\text{m}$ .

Furst showed that it is possible to align hemispherical parts using a compact device featuring a linear voice-coil actuator that uses impact actuation to align the workpiece to micrometer precision [2]. The set-up for Thumper I is shown in Figure 6 and Thumper I operates as follows. A PC-based software program rotates the spindle and collects runout data from either the electronic gage or touch probe which are contacting a hemispherical part. The software determines the location of the high spot, and then rotates the spindle so the high spot is next to the actuator positioned underneath the part. Then, a voltage signal is applied to the actuator, resulting in an impact between the part and plastic tip of the actuator. It is this impact that moves the part towards the center of rotation and reduces runout. This process of measuring and impacting is repeated until part misalignment is less than 2.5  $\mu\text{m}$ .

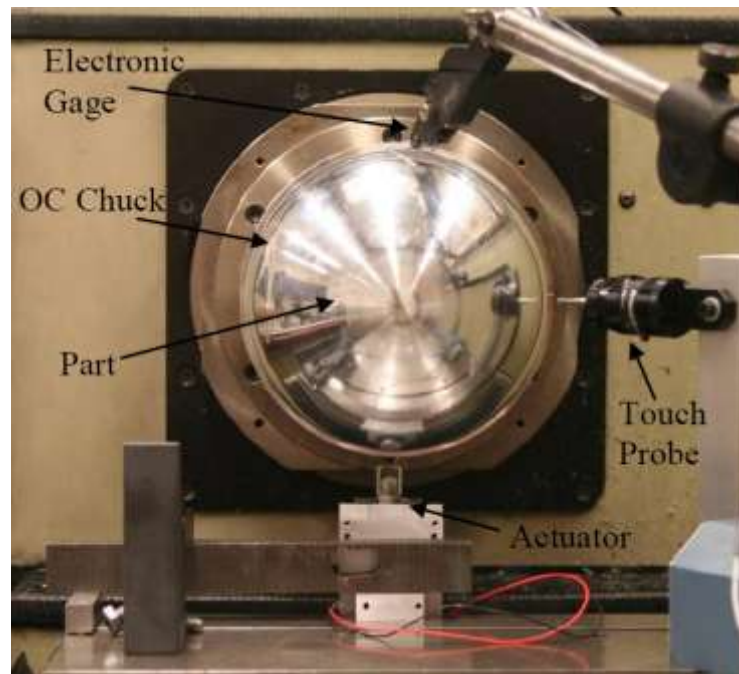


Figure 6. Thumper I - Solution to automated part centering [2].

The construction of the Thumper I actuator is shown in Figure 7. To displace the part, Thumper I applies a voltage across the voice-coil actuator (VCA) which accelerates the VCA coil, translating shaft, and impacting head to a desired velocity. The operation of a VCA is described in detail in Sections 2.2.1 and 4.2. When the impacting head strikes the workpiece at a given velocity, the actuator will displace the workpiece some amount based on the friction force between the workpiece and chuck and the impacting mass and velocity.

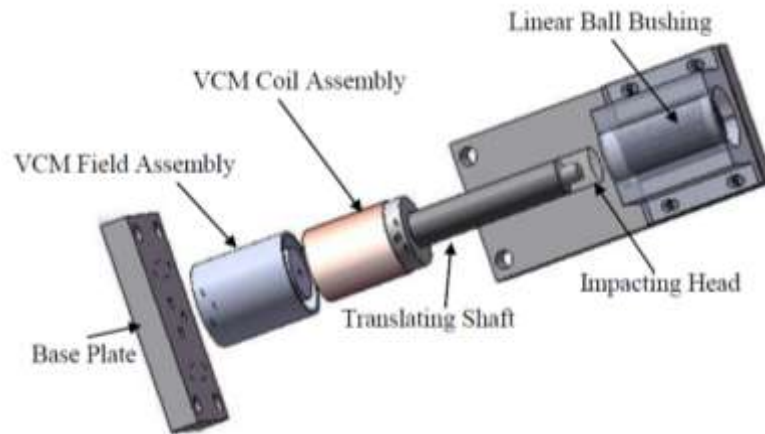


Figure 7. Thumper I actuator construction [2].

It is important to understand the impact actuation technique developed by Furst. The free body diagram given in Figure 8 explains the operation of impact actuation with Thumper I. It shows the coil-shaft-tip assembly from Figure 7 (with mass  $m_t$ ) impacting a hemispherical part at some velocity  $v_t$ . Thus, to move the part a greater distance, Thumper I must impact the part with a greater velocity since the impacting mass is constant.

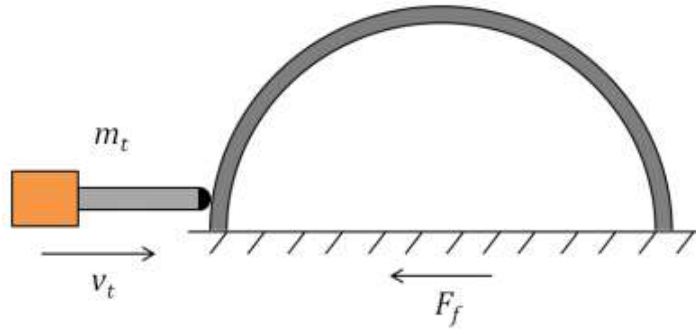


Figure 8. Free body diagram for impact actuation.

*Impact actuation versus pushing the part*

The difficulty of displacing a part to micrometer precision by slowly pushing the part can be understood with the experimental setup in Figure 9 [2]. In this experiment, a part (called “Puck” in Figure 9) on a vacuum chuck is pushed by moving the axis of a turning machine into the part. The force that the axis imparts on the puck is measured with a load cell on the “Pusher”. The part and axis displacements are measured with an electronic gage and cap gage, respectively.

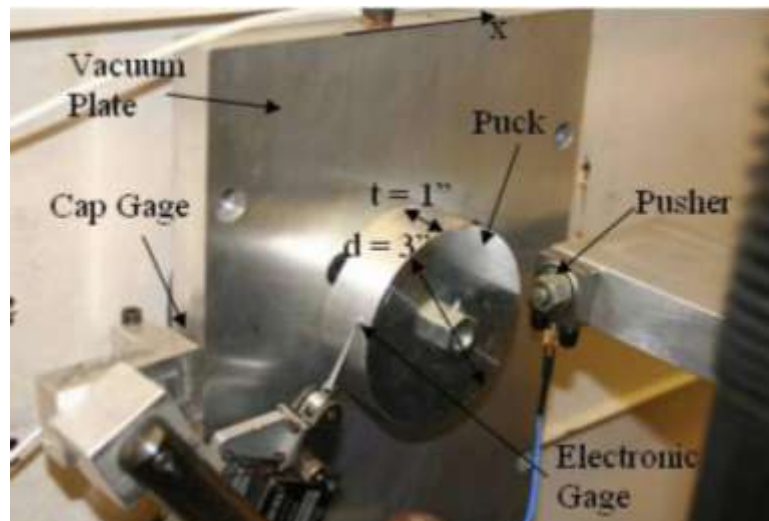


Figure 9. Experimental set-up for pushing a part [2].

As seen in Figure 10, the force imparted on the puck increases as the axis position moves further into the puck. At around 11 seconds, the force becomes large enough to displace the puck. As seen in Figure 10, the puck quickly displaces by about 2 micrometers just after the force becomes great enough to move the part. This 2 micrometer distance is the least significant distance (LSD) that the part will move from the pushing method under the conditions for Figure 10.

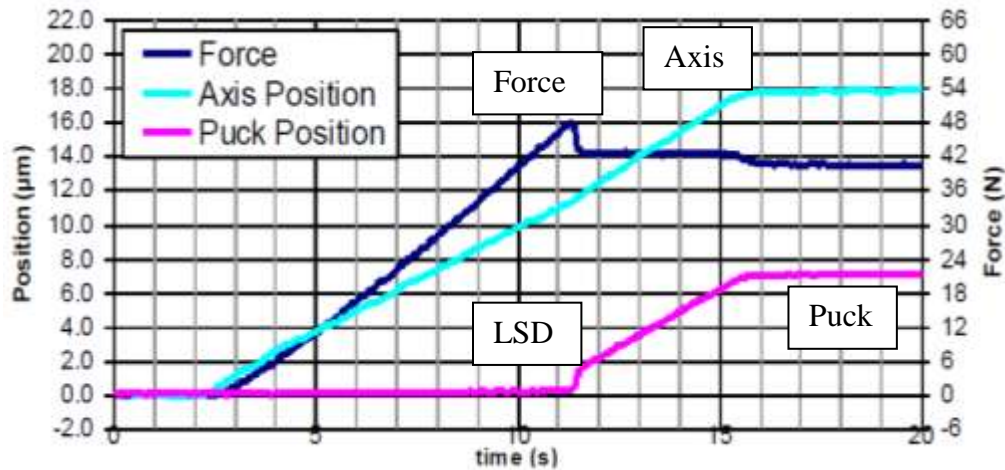


Figure 10. Experimental results from pushing a part [2].

Figure 10 shows two characteristics of the pushing method that make it undesirable for precision part alignment.

- 1) The 2 µm LSD is difficult to avoid with the push method. It occurs because the force applied to the part remains for seconds after the part begins to move. This characteristic of the pushing method makes it difficult to displace parts less than a few micrometers.
- 2) The pushing process described in Figure 10 is inherently slow. To achieve small displacements with the pushing method, the force must be gradually applied (i.e. over

10 seconds as in Figure 10). If the force is not gradually applied, then the applied force will displace a greater distance.

The tapping method demonstrated by Furst is the ideal method to displace an object with micrometer precision. Furst selected the impact actuation method instead of the pushing method because the impacting object imparts a force on the workpiece that lasts for about 1 millisecond. With the impact method, a force is imparted onto the part that is great enough to move it, but the force does not last long enough to incur an LSD as in the pushing case. The Thumper II device, described in Sections 2 – 5, directly employs the impact actuation technique. More detail on the physics of the impact are given in Section 1.2.1.

#### *Thumper I conclusions*

While Thumper I was able to consistently align workpieces to less than 2.5  $\mu\text{m}$ , it had key shortcomings. The method for this automated technique required a separate measurement probe, and as a result it is neither automated enough nor compact enough to produce cost-savings or be beneficial in a glove box environment. A second shortcoming is the fact that it requires reading and controlling the spindle position during the alignment process. Therefore, this device could only be used on machines with spindle encoder data available.

Yet, the Thumper I device demonstrated a successful technique for automating the part centering process using a compact actuator assembly. This solution is the foundation for a more automated and general solution, Thumper II, described in Sections 2 – 5.

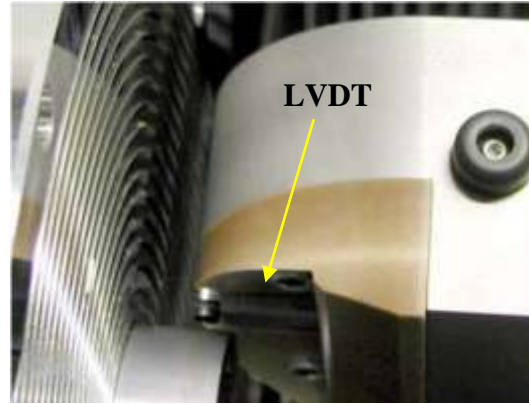
#### **1.1.5 Automated centering: Precitech PCA**

One commercial product for automating part centering on a vacuum chuck already exists. This solution, known as the “Part Centering Accessory” (PCA), has been developed by Precitech and can be seen in Figure 11. Figure 11 (a) shows a standard tool holder in the foreground with the part centering device in the background contacting the part. A close-up view in Figure 11 (b) shows that the PCA contains an LVDT which measures the part runout.

The PCA device is capable of measuring part runout as well as displacing the part towards the center of rotation.



(a)



(b)

Figure 11. Precitech “Part Centering Accessory” [3].

The Precitech PCA begins alignment by moving the machine axis to zero the LVDT. It then rotates the spindle while measuring the runout with the LVDT, locates the center of the part, and then rotates the spindle so the high spot is next to the PCA. Lastly, the software reduces the vacuum pressure so the part can be displaced with a lower force, and the device slowly pushes the part using the machine axis. The part eccentricity is located again and is pushed again until the eccentricity is as small as required. The Precitech PCA is designed for achieving part misalignment less than 2  $\mu\text{m}$  in 15 seconds for small parts.

The Precitech device has limited application.

- 1) The biggest limitation of this device is its communication with and control of the turning machine. The PCA software must control the spindle, one machine axis, and vacuum pressure. The device is only designed for use on certain Precitech machines that contain certain control hardware. This makes it very difficult to use this device on a general lathe machine.

- 2) Another potential limitation of this device concerns the method it uses to displace the part. If part displacement is to occur, the motor of the machine axis must be able to overcome the force due to vacuum pressure that holds the part to the chuck. This is problematic for heavy parts as the axis motor must overcome a high friction force value. The vacuum could be lowered to alleviate this difficulty. However, lowering the vacuum pressure could be dangerous or costly if the part falls off the chuck, especially if the part is heavy or expensive.
- 3) A final issue with the PCA is that it relies on pushing the part instead of impulse actuation.

## **1.2 Impact, Friction, and Part Motion**

The workpiece is displaced due to an impact with a plastic tip as described with Thumper I in Section 1.1.4 and Figure 8. To improve this design, it is essential to understand the physics of the tip-workpiece collision, as well as the physics of the friction that exist between the workpiece and chuck face.

### **1.2.1 Hertz contact**

#### *Hertz contact theory and deriving the impact force*

Impact actuation is the ideal strategy for aligning a part to micrometer precision. This is mostly due to stick-slip friction behavior to be discussed in Section 1.2.2. First, it will be useful to understand the physics of two colliding objects. The impacting tip (as seen in Figure 5) is spherical and the workpiece is spherical as well. Hertz contact theory [4] and its associated equations explain what occurs during the collision. A diagram of Hertz contact for two spheres is seen in Figure 12. The force  $F_a$  results in a deformation of the contact surface defined by a circular area of radius  $a$ .

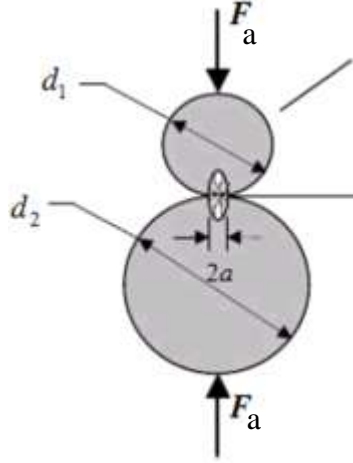


Figure 12. Hertz contact with two spheres [5].

The Hertz contact values  $CE$  (material constant) and  $KD$  (geometric constant) are defined with the relations in Equations (1) and (2). The variables  $d_1$  and  $d_2$  are the diameters of the contacting spheres. The variables  $E$  and  $\nu$  are the elastic modulus and position's ratio of each material [4].

$$CE = \frac{1 - \nu_1^2}{E_1} + \frac{1 - \nu_2^2}{E_2} \quad (1)$$

$$KD = \frac{d_1 d_2}{d_1 + d_2} \quad (2)$$

The center-center approach  $y$  of the two spheres (i.e. distance the two centers move towards each other) is given by Equation (3).

$$y = 1.04 \sqrt[3]{F_a^2 C_E^2 / K_D} \quad (3)$$

Equation (3) can be rearranged for force  $F_a$ , yielding Equation (4).

$$F_a = \left( \frac{y}{1.04} \right)^{1.5} \sqrt{\frac{K_D}{C_E}} \quad (4)$$

The nonlinear interface stiffness  $k$  satisfying the relation  $F_a = ky$  can be found using the result in Equation (4), yielding:

$$k = \left(\frac{1}{1.04}\right)^{1.5} y^{0.5} \sqrt{\frac{KD}{CE^2}} \quad (5)$$

### *The finite difference model and Hertz impact*

The goal of the finite difference method here is to calculate the force profile (i.e. force versus time during an impact). In the finite difference method, a set of initial conditions start the computation and a set of equations update the values in the computation during each time step.

Equations (6) show the initial conditions for the finite difference method. The tip velocity (i.e. impact velocity) has an initial value  $\dot{x}_{tip0}$  and the initial center-center approach is zero.

$$\begin{aligned} \dot{x}_{tip}(0) &= \dot{x}_{tip0} \\ y(0) &= 0 \end{aligned} \quad (6)$$

The equations that are updated are seen in Equations (7) – (10).

- 1) First, the center-center approach,  $y(t)$ , is calculated with Equation (7) and depends on the previous center-center distance,  $y(t - \Delta t)$ , and the distance the tip translates into (or out of) the part defined by the tip velocity from the previous time step,  $\dot{x}_{tip}(t - \Delta t)$ , and the time step duration  $\Delta t$ .
- 2) Second, the impact force,  $F_a(t)$ , is calculated with Equation (8) and is a function of the center-center approach just calculated.
- 3) Third, the acceleration of the tip,  $\ddot{x}_{tip}(t)$ , is calculated with Equation (9) and is a function of the mass of the tip,  $m_{tip}$ , and the impact force just calculated which acts to accelerate the tip away from the part.

- 4) Fourth, the velocity of the tip,  $\dot{x}_{tip}(t)$ , is calculated with Equation (10) and is a function of the tip velocity from the previous time step, the tip acceleration, and time step duration.

$$y(t) = y(t - \Delta t) + \dot{x}_{tip}(t - \Delta t) * \Delta t \quad (7)$$

$$F_a(t) = \left(\frac{y(t)}{1.04}\right)^{1.5} \sqrt{\frac{K_D}{C_E}} \quad (8)$$

$$\ddot{x}_{tip}(t) = F_a(t)/m_{tip} \quad (9)$$

$$\dot{x}_{tip}(t) = \dot{x}_{tip}(t - \Delta t) + \ddot{x}_{tip}(t) * \Delta t \quad (10)$$

The accuracy of the finite difference method increases as the time step duration decreases[6]. A suitable time step value for the impact simulations was found to be  $5 \times 10^{-7}$  seconds, and this value was found by observing when the force profile calculated from the finite difference model converged.

#### *Experimentation with Hertzian collision*

Two tip materials have been used in testing; acrylic and nylon. The tips have been machined using a sharp diamond tool to have a diameter of 50 mm. The properties for these materials are listed in Table 1. Nylon was eventually selected as the tip material due to lower wear as discussed in Section 4.1.8. Workpiece material properties of Al 6061 and 304 SS are also listed in Table 1. Part 2 is Al 6061, while part 1A, 1B, and 3 are 304 SS. The part numbers refer to the parts list in Appendix A.

Table 1. Key material properties.

Material	Elastic Modulus (GPa)	Poisson's Ratio
Nylon [7]	1.13	0.35
Acrylic [8]	2.88	0.40
AL 6061[9]	69.0	0.35
304 SS [10]	193	0.29

The set-up seen in Figure 13 was used in many tests to measure the force profile during a tap. In this set-up, the tip of the device impacts a flat surface that is connected to a load cell which measures the impact force. Since the tip is impacting a flat surface, Equation (2) must be changed to Equation (11) below, where  $d_1$  is the diameter of the impacting tip.

$$KD = d_1 \quad (11)$$

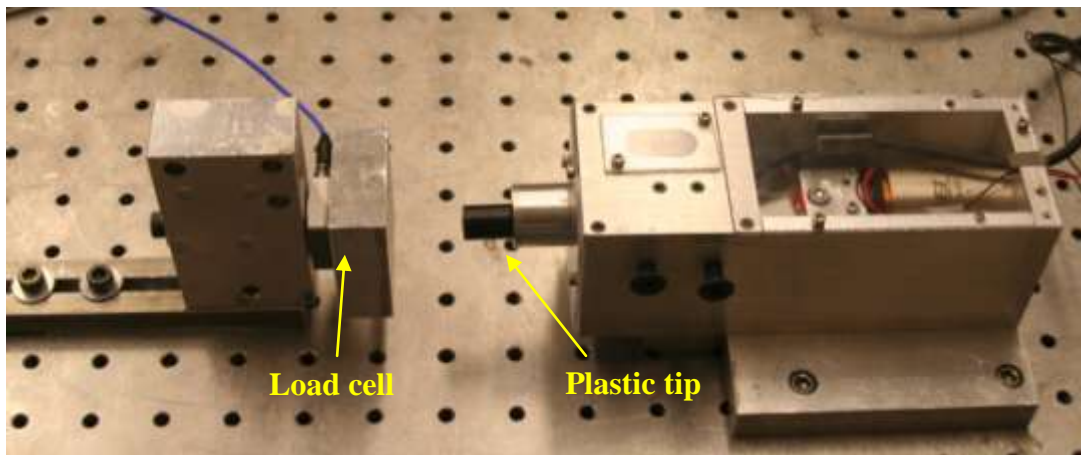


Figure 13. Experimental set-up with plastic impacting tip and load cell.

Simulated force profiles for three tap velocities can be seen in Figure 14 alongside force profiles measured with the set-up in Figure 13. A simulated force profile was found using an impacting mass of 0.2 kg. Figure 14 suggests that Hertz contact theory provides a qualitatively and quantitatively reliable prediction of the force profile which results from an impact. The simulated force profiles in Figure 14 are smoother than the experimental

profiles. The peak force for the measured profile is slightly less than the simulated for all three velocities. This difference can be partly attributed to small differences in shape (i.e. deviation from sphere due to wear) as well as variability in material properties. Average values for elastic modulus and Poisson's ratio were used in the simulated plots. However, using values slightly different from the average value could result in theoretical force profiles closer to experimental. Based on Figure 14, increasing the peak impact force from 150 N to 425 N results in a slight decrease in impact duration.

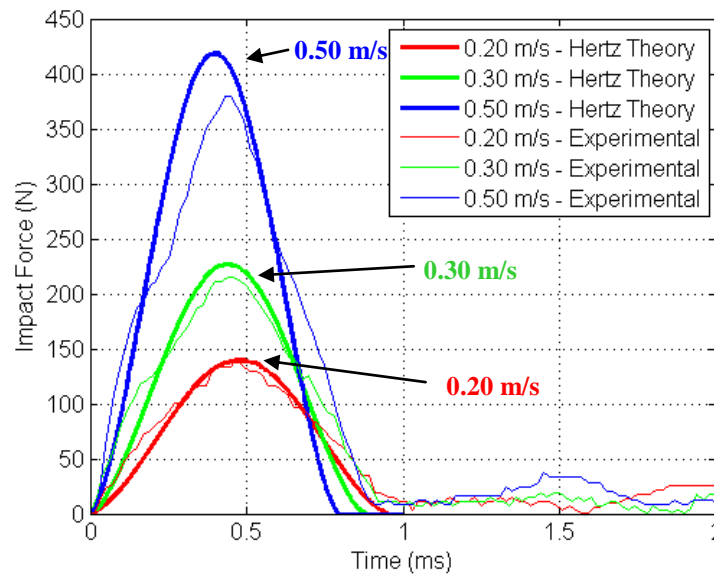
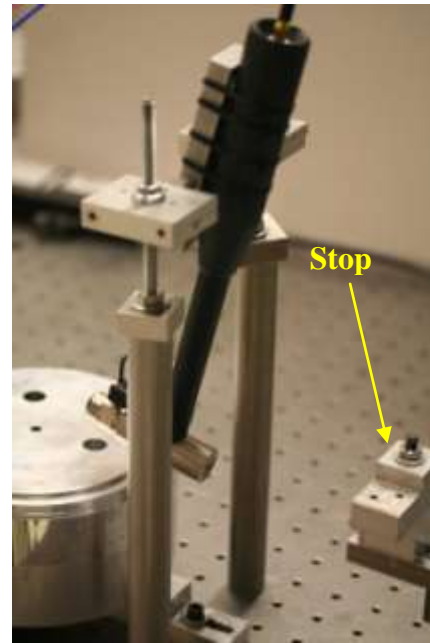


Figure 14. Simulated and measured force profiles for three impact velocities.

The material properties of the tip affect the peak force and duration of the impact. As seen in Equation (5), increasing the elastic modulus of either object will increase the stiffness of the interface between the impacting objects. To understand these effects further, experiments using the impact hammer in Figure 15 were performed. The impact hammer contains a force transducer so the impact force profile can be measured. It also has tips of different materials that can be used. As seen in Figure 15 (b), the impact hammer pivots and can be pulled back to contact the stop.



(a)



(b)

Figure 15. Experimental set-up using impact hammer.

The hammer “swing” set-up allows for highly repeatable forces to be applied. The hammer is lifted to contact the adjustable stop seen at the right of Figure 15 (b) allowing for the repeatable force profiles. The plots in Figure 16 show the repeatability of the hammer force profile for three separate taps using a plastic tip on the hammer.

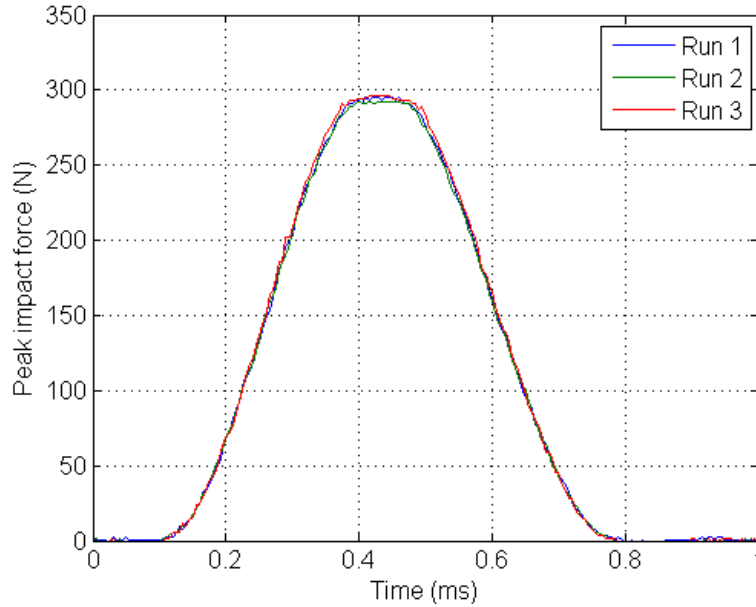


Figure 16. Repeatability of impact hammer force profiles.

Figure 17 shows measured force profiles at the same impact velocity (i.e. same hammer drop position) for three materials used as the impact hammer tip. For the same impact velocity, the steel tip has a peak force (700 N) which is more than twice that measured with the plastic tip (300 N). However, the duration of impact for the steel tip (0.3 ms) is half that of the plastic tip (0.6 ms). The amount of part displacement is related to the peak force, as well as the duration of impact.

Studying Figure 17 qualitatively illustrates why a plastic tip is used for Thumper II instead of a rubber or metal tip. The main issue with a metal tip is that it could damage the part during a given tap as the higher forces result in higher stresses. The rubber tip is not desirable because it requires a higher impact speed to exceed static friction and move the part. This shifts the required impact velocity range of Thumper II upwards, requiring more power and size from Thumper II. A plastic tip provides a desirable compromise between the metal and rubber tips.

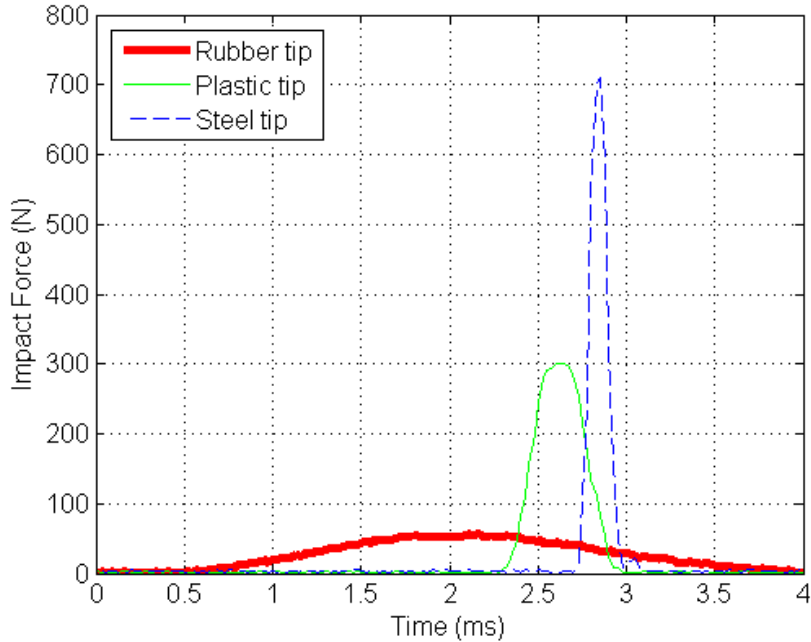


Figure 17. Varying tip material for same impact velocity using impact hammer.

### 1.2.2 Modeling friction

Friction can be described as the force that exists at the interface of two contacting objects in the direction tangential to the contact interface. Friction arises at the contact interface between the workpiece and chuck and understanding friction at this interface is critical to the design of a precision alignment device.

Friction is often a major obstacle to achieving precise motion in a machine [11], [12]. Koren notes that friction in machine axes often leads to errors while machining a workpiece [12], [13]. Friction occurring in joint angles of an industrial robot makes precise positioning challenging. Stick-slip motion (defined in later in this section) in robotics often leads to static position errors and undesirable motions [13]. Despite the variability in friction, friction compensation control algorithms can be implemented to ensure a certain machine precision [11], [12]. The adaptive algorithm explained in Section 4.3 is complex enough to overcome variations in friction.

Friction is commonly explained physically as an interaction between surface asperities. Asperities are the small bumps and protrusions on the surface of objects as shown in Figure 18. Asperities have been modeled (i.e. the LuGre model [14]) to yield an approximation for the friction force and relative object displacement.

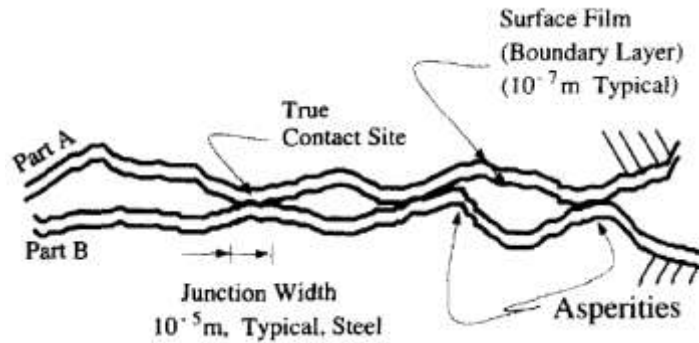


Figure 18. Diagram of surface asperities [15].

#### *Validity of Amonton's Law*

The two laws provided by Amonton in the 17<sup>th</sup> century provide the most basic understanding of friction. A discussion of these laws and their validity gives interesting insight into the mechanisms of friction. Amonton's two laws are stated below [16]:

1<sup>st</sup> law – The force of friction is directly proportional to the applied load.

2<sup>nd</sup> law – The force of friction is independent of the *apparent* area of contact.

Amonton's 1<sup>st</sup> law results in the most basic relation for friction seen in Equation (12). It states that the friction force  $F_f$  is equal to the product of the normal load  $N$  and a friction coefficient  $\mu$ . Amonton's law does not include differentiation between static friction and kinetic friction.

$$F_f = \mu N \quad (12)$$

Amonton's 2<sup>nd</sup> law is an important result when considering the hemispherical shell workpiece. Even though the nominal cross-section of the hemishell is a 6" diameter circle, only a 1/4" thick wall of the shell actually contacts the OC chuck. Amonton's 2<sup>nd</sup> law states that the friction force is independent of the apparent contact area, thus the fact that only a 1/4" thick wall contacts the chuck is irrelevant.

### *Stiction and the Coulomb friction force*

It has been experimentally observed that the force to move an object initially is larger than the force required to keep the part sliding [17]. This difference is not captured with Amonton's Laws. Equation (13) describes how the stiction (i.e. static friction) and Coulomb friction forces are used together to model these two friction force levels. The stiction force  $F_s$  is the external force required to initiate object motion, and external forces below stiction will result in no relative displacement. The Coulomb friction force  $F_k$  is the kinetic friction force that describes the active friction force while an object is sliding. The kinetic friction force is the minimum force required to maintain part sliding. In general, the force  $F_k$  is less than the force  $F_s$ .

$$\begin{aligned} F_s &= \mu_s N \\ F_k &= \mu_k N \end{aligned} \tag{13}$$

Figure 19 shows the behavior of friction with the Coulomb model. For the part to remain at rest the applied force must be less than the static friction force. Once relative motion occurs, the friction force immediately drops to the kinetic friction force. However, this immediate change in friction levels does not accurately reflect reality.

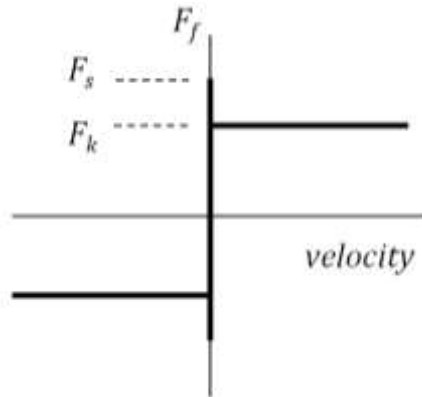


Figure 19. Coulomb friction behavior.

*The Stribeck friction model*

The Stribeck curve describes a continuous transition from static to kinetic friction when sliding is initiated [17]. The curve also describes the continuous transition from kinetic to static friction when a sliding object comes to rest. The Stribeck curve, pictured in Figure 20, differs from the instantaneous change in friction force seen in the Coulomb model. As indicated in Figure 20, the Stribeck curve describes the friction force as a function of the relative sliding velocity.

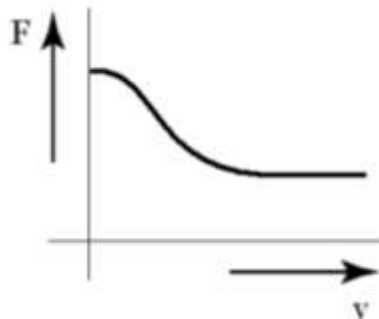


Figure 20. Stribeck curve with dry friction [5].

A general model for friction can be described with Equation (14), which combines the stiction and Coulomb friction force levels, as well as the Stribeck curve [17]. As seen in Equation (14), Stribeck friction is related to the relative sliding velocity  $v$  and the Stribeck curve velocity  $v_s$  that defines how quickly the friction force changes from static to kinetic or vice versa. The  $F_s$  term is the static friction force and the  $F_k$  term is the kinetic friction force. The Stribeck effect is most prominent for low ( $\approx 5 \mu\text{m}$ ) object displacements. Thus, using the Coulomb assumption yields nearly identical results as using the Stribeck assumption for large part displacements. This claim is explored later in Section 1.2.3.

$$F_f = \begin{cases} F_k + (F_s - F_k)e^{-\left|\frac{v}{v_s}\right|} & \text{if } v \neq 0 \\ F_e & \text{if } v = 0 \end{cases} \quad (14)$$

### *Stick-slip motion*

The physical mechanism of friction is understood to be a result of the interaction of surface irregularities (i.e. asperities) on contacting surfaces [14]. As a force attempts to move one object with respect to the other, the surface asperities will deflect like the bristles seen in Figure 21. The force resulting from this bristle deflection results in a force resistive to motion. If the applied force is large enough, the bristles will slip and the object will slide.

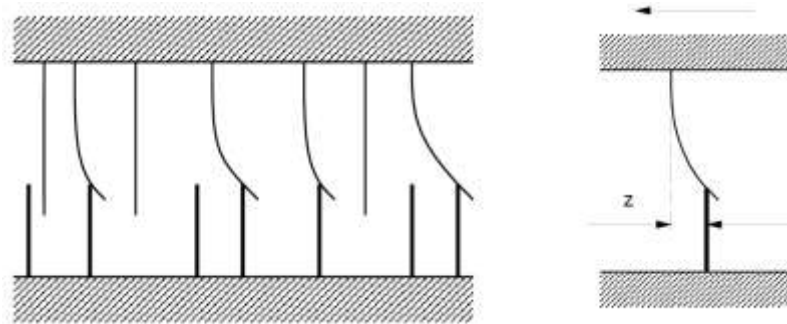


Figure 21. LuGre asperity friction model [17].

The spring model shown in Figure 22 describes the effect of the bristles on part motion. The actuator impacts the part with some velocity  $v$  and the spring in Figure 22 represents the bristles in Figure 21 that deflect before sliding occurs. If the impact force does not exceed static friction, then the actuator will compress the spring (i.e. deflect the bristles) seen in Figure 22 and rebound without displacing the part. If the impact force does exceed static friction, then the actuator will compress the spring enough to displace the part permanently.

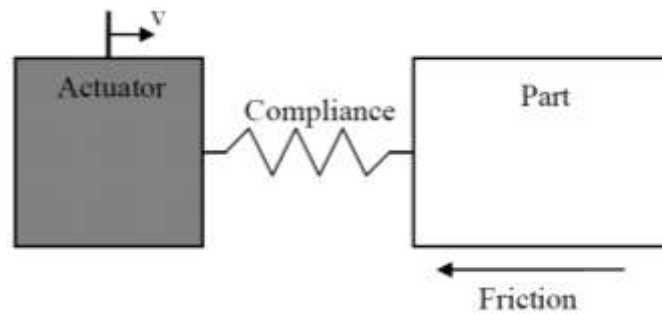


Figure 22. Friction spring model [2].

Stick-slip motion is the main reason that Thumper I *tapped* the part instead of *pushed* the part to align it. Stick-slip motion describes how an object moves when an external force *slowly* increases above the static friction force value.

Stick-slip behavior is described with the following observation. Once the external force exceeds the static friction force for an object at rest, motion begins to occur. Since the friction force decreases once part motion ensues, acceleration of the object will continue until the external force becomes less than the dynamic friction force. The object will accelerate as long as the external force exceeds the friction force.

With this understanding of stick-slip motion, it is seen that once motion begins, the external force must exceed the dynamic friction force value for a short amount of time if little part displacement is desired. This condition is assured if the part is tapped and static friction is exceeded.

Despite the challenges of stick-slip motion, Furst showed that it is possible to move parts on a vacuum chuck with micrometer precision by *pushing* the part [2]. However, this required a complex set-up that ensured the applied force is quickly released after part motion is sensed, and also required control of a machine axis and the spindle. This set-up also required a static spindle, indicating that this may not result in a quick alignment process for heavy parts.

### 1.2.3 1-D Newton-Hertz-Stribeck (NHS) part motion model

A 1-D Stribeck friction model on a horizontal surface is useful to discuss. This Newton-Hertz-Stribeck (NHS) part motion model combines the Hertz impact model, the Stribeck friction model, and Newton's 2nd law. Figure 23 shows a free body diagram for an object resting on a horizontal surface. The impactor has a mass  $m_{tip}$  and velocity  $\dot{x}_{tip}$  while a friction force  $F_f$  resists object motion.

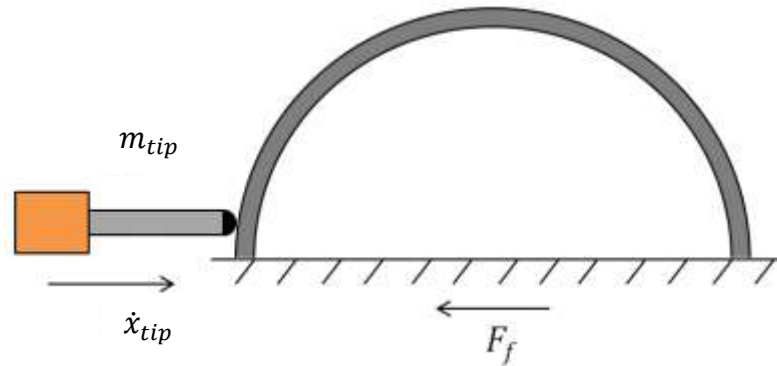


Figure 23. Free body diagram for impact actuation.

The finite difference method is used for the NHS part motion model. Refer to Section 1.2.1 to understand the steps in the finite difference method that calculate the tip motion and impact force. The finite difference method for calculating part motion due to an impact is explained with Equations (15) – (18).

- 1) First, the friction force  $F_f(t)$  is found with Equation (15) and is a function of the static and kinetic friction forces, as well as the part velocity from the previous time step,  $\dot{x}_{part}(t - \Delta t)$ .
- 2) Second, the acceleration of the part  $\ddot{x}_{part}(t)$  is calculated with Equation (16) and is a function its mass,  $m_{part}$ , and the difference between the impact force,  $F_a(t)$ , and friction force,  $F_f(t)$ .
- 3) Third, the velocity of the part  $\dot{x}_{part}(t)$  is calculated with Equation (17) and is a function of the previous velocity, part acceleration, and time step duration.
- 4) Fourth, the position of the part  $x_{part}(t)$  is calculated with Equation (18) and is a function of the previous position, part velocity, and time step duration.

$$F_f(t) = F_k + (F_s - F_k)e^{-\left|\frac{\dot{x}_{part}(t-\Delta t)}{0.001}\right|} \quad (15)$$

$$\ddot{x}_{part}(t) = [F_a(t) - F_f(t)]/m_{part} \quad (16)$$

$$\dot{x}_{part}(t) = \dot{x}_{part}(t - \Delta t) + \ddot{x}_{part}(t) * \Delta t \quad (17)$$

$$x_{part}(t) = x_{part}(t - \Delta t) + \dot{x}_{part}(t) * \Delta t \quad (18)$$

Figure 24 shows results from a simulation of impact, friction, and part motion. In this simulation, a part is sliding on a surface parallel to the ground. This location of the shell at any time is shown in the “Shell Position” plot. The plot also shows the parabolic-like impact force profile as the impacting mass strikes the shell and rebounds. For this simulation, the impacting mass and velocity was 0.20 kg and 0.80 m/s respectively. This moves the 6.5 kg mass about 17  $\mu\text{m}$  in 1.4 ms.

The friction force is equal to the impact force and part motion (i.e. shell position change) does not occur until the static friction force of 290 N is exceeded. When motion begins, the friction force decreases gradually according to velocity-based Stribeck theory. In Section 1.2.4, it will be shown that these simulated curves for impact force and part displacement agree with experimentation.

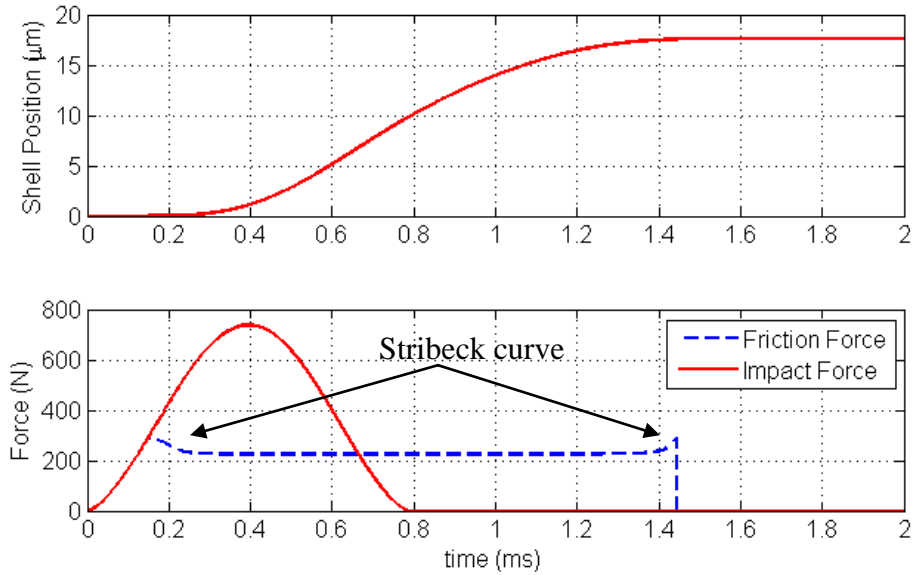


Figure 24. Simulation of impact, friction, and 1-D part motion.

*Stribeck curve and sliding distance*

As seen in Figure 24, the Stribeck curve (i.e. model for static/dynamic friction transition) is only present during the beginning and end of object sliding. Thus, the Stribeck curve will have less of a relative effect on the total sliding distance for longer sliding distances. The values in Table 2 illustrate this fact and were taken from 1D sliding simulations. As seen, the percent difference values for part displacement between the two friction models is near 2% at a 1.00 m/s impact velocity, while there is a percent difference of 97.2% at 0.37 m/s. A number of parameters were used for these simulations and are listed here: vacuum (10.0 psi); part weight (63.4 N); static friction coefficient (0.23); kinetic friction coefficient (0.18); impacting mass (0.20 kg).

Table 2. Sliding distance ( $\mu\text{m}$ ) for simulations with Stribeck friction and Coulomb friction.

Impact velocity (m/s)	Part displacement ( $\mu\text{m}$ )		% Difference
	Stribeck Friction	Coulomb Friction	
1.00	32.6	33.3	2.10 %
0.80	17.5	18.2	3.85 %
0.50	3.08	3.62	14.9 %
0.40	0.43	0.96	55.2 %
0.37	0.01	0.36	97.2 %

#### 1.2.4 1D part motion experiments

##### *Understanding the static friction coefficient*

Figure 25 shows a mass hanging by a wire that is connected to the cylindrical workpiece through a pulley mounted on a shaft. Known masses are incrementally added to the mass holder until part sliding is visually observed, yielding a value for static friction force and thus static friction coefficient.



Figure 25. Set-up for pulley-mass experiment to determine static friction coefficient.

Table 3 shows how the static friction coefficient measured with the set-up in Figure 25 varies with surface condition. These results, and other tests, suggest that a realistic static friction coefficient value for steel on aluminum is 0.18 – 0.25.

Table 3. Variation of static friction coefficients with surface condition.

Condition	$\mu_s$ from pulley-mass expt.
Cleaned with mineral spirits	0.54
Rubbing hand on surface for 30 seconds	0.26
Thin layer of cutting oil	0.18

### *1D Part sliding*

Figure 26 shows an experiment used to measure friction between a part and a horizontal surface. Figure 26 shows a cap gage which measures the displacement of the part caused by an impact from the hammer. The impact hammer is used in the same fashion as described in Figure 15. Vacuum can be used to increase the contact load between the part and surfaces. The cap gage and impact hammer outputs are recorded simultaneously on an oscilloscope to allow temporal synchronization.

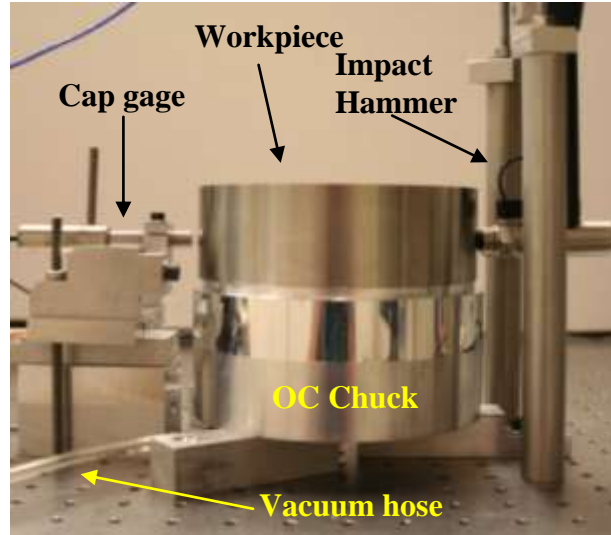


Figure 26. Impact hammer and part displacement set-up for 1D sliding.

### *Simple 1D sliding experiments*

Using the set-up in Figure 26, the 1D NHS model can be verified. Part 1A was used in this test and the surfaces were cleaned with mineral spirits. Figure 27 (a) shows simulated part displacement and impact force using the model in Section 1.2.3 while Figure 27 (b) shows experimental results.

The simulated model uses a friction value of  $\mu_s = 0.50$ , the average found with pulley-mass experiments on the same day. The only unknown for the NHS model is the  $\mu_k$  value. This value is iterated in the NHS simulation until the simulated displacement is very near the observed and yields a kinetic friction coefficient of  $\mu_k = 0.43$  for the plot in Figure 27 (a).

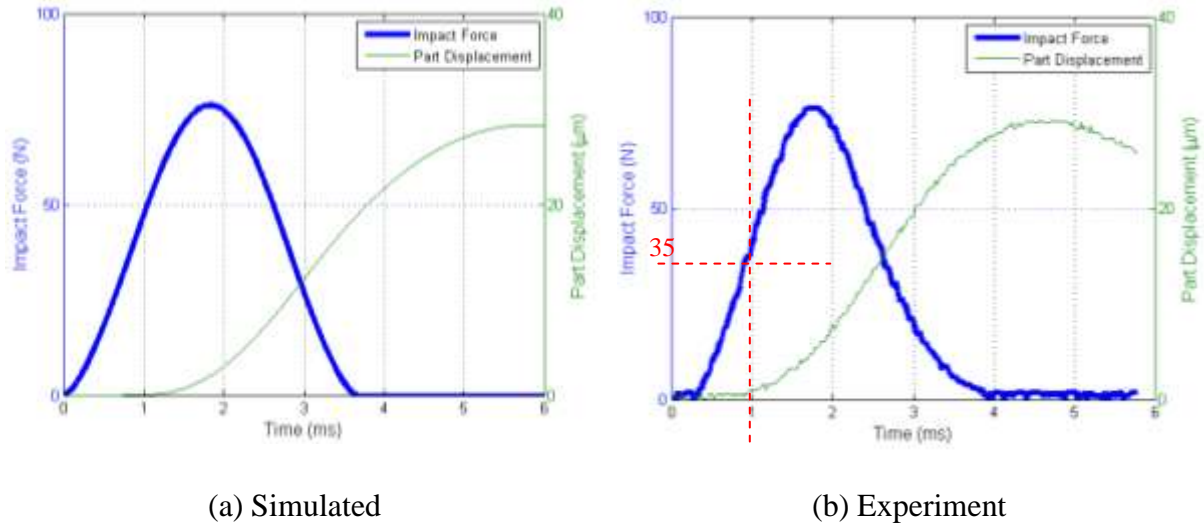


Figure 27. Simulated and experimental part displacement and impact force.

The strong similarities between the shapes of the experimental and simulated plots in Figure 27, and the realistic  $\mu_k$  value, suggest that the NHS model can be used to predict part motion. It is interesting to note that iterating on the  $\mu_k$  value in the simulation to match the empirical and simulated displacement also resulted in a close match in the impact force profiles. This further suggests the validity of the NHS model.

As seen in Figure 27 (b), the part does not begin sliding at impact, but sliding begins when the force reaches the static friction level of 35 N according to Figure 27 (b). The expected static friction force is 32 N from the pulley-mass experiments which determined  $\mu_s = 0.50$  with a part weighing 63.4 N. Thus, Figure 27 (b) confirms the assumption that part sliding does not occur until static friction is reached. As seen in Figure 27 (b), it is difficult to define exactly when part sliding begins. This could be partly due to presliding displacement phenomenon.

### *Presliding displacement*

Before sliding occurs in the LuGre model, small amounts of bristle deflection can occur resulting in what is termed presliding displacement. The transition from elastic asperity deflection to sliding is not easily defined and does not happen at a single instant [15]. In steel contacts, the presliding displacement regime is typically about 2–5  $\mu\text{m}$  [15]. This cited range for presliding displacements makes it important to understand this phenomenon when positioning parts to a misalignment of 2.5  $\mu\text{m}$ .

Experiments were conducted to observe the presliding displacement using the same set-up as in Figure 26. Part 1B was used in this experiment (i.e. 304 SS and 30 lb). It was observed from pulley-mass experiments performed before these presliding tests that the static friction coefficient is  $\mu_s = 0.19$ . This yields a static friction force of 25.4 N for the 30 lb part.

To perform the presliding displacement experiment, the part was tapped with the impact hammer for peak forces around 25.4 N. Table 4 and Figure 28 show the results for this experiment. At a force of 20.2 N, the part moves 0.10  $\mu\text{m}$ . This would yield a static friction value of 0.13 if 0.10  $\mu\text{m}$  were considered sliding. However, the fact that part motion is measured well before the static friction force is exceeded suggests the presence of presliding displacement.

Table 4. Observation of presliding displacement.

Peak Force (N)	Displacement ( $\mu\text{m}$ )
20.2	0.10
24.6	0.24
25.7	0.36
27.5	0.99
31.1	1.90

The values in Table 4 are plotted in Figure 28 and shows that the displacement-force relationship is divided into two regimes separated near the static friction force of 25.4 N. Above static friction force, a given increase in applied peak force yields a much greater change in part displacement than below the static limit. These could be understood as the presliding regime and sliding regime, though as mentioned before, this transition is difficult to clearly define. Yet, it is clear that part motion occurs before static friction is reached.

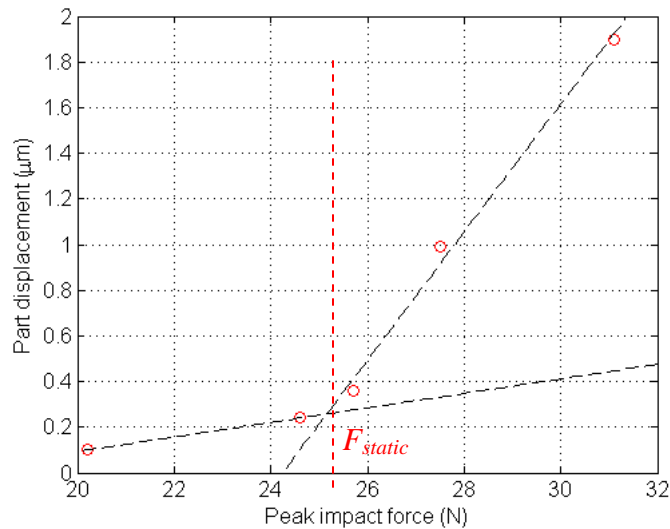


Figure 28. Presliding displacement plot.

The data in this set of experiments do not prove the mechanism of presliding displacement. Nevertheless, Table 4 and Figure 28 show that friction is continuous and that sub-micrometer displacements occur well below the static friction limit.

#### *Hysteresis at displacement reversal*

Displacement reversal hysteresis refers to the apparent variation in friction when the direction of part motion is reversed. This hysteretic behavior was noted by Furst to be an impediment to centering parts to less than 2.5 μm of misalignment [2].

This hysteresis effect can be described by considering an object on a horizontal surface. If the object is tapped multiple times with the same magnitude in a single direction, the object will displace some nominal distance from to each tap. In actuality, there will be some variation in individual displacements due to friction variations, but these variations are small relative to the reversal effect. If the object is then tapped multiple times with the same impact magnitude in the *reverse* direction, a significant increase in object displacement can occur for the first few taps in the opposite direction. Thus, this observation states that large differences in object displacement for a given impact magnitude can occur after displacement direction is reversed.

The reason for this hysteresis behavior can be understood as a strain buildup in the bristles captured in the spring model in Figure 22. When direction is reversed, the compressed spring (i.e. strained bristles) will release energy that can help displace the part an additional amount.

The hysteresis effect was studied using the experimental set-up in Figure 26. To perform the hysteresis test, the part was first tapped multiple times with a mallet towards the impact hammer. Then, the impact hammer supplied a series of impacts to the part to move it in the opposite direction. This is not true hysteresis as the initial impacts from the mallet are not necessarily of the same magnitude as the impact hammer taps. Nevertheless, the reversal effect is clear from these tests. Figure 29 – Figure 31 were created using this experimental method and these plots explore the relation between the reversal effect and three parameters: surface condition, vacuum and normal load, and impact magnitude. The first tap in the reverse direction yields about 2  $\mu\text{m}$  for each case. This helps to reduce the number of variables.

#### *Direction reversal hysteresis: Lubrication and surface condition*

Figure 29 shows the effect of surface condition on directional hysteresis. The plot shows the amount the part displaced due to each tap after reversing direction. In both cases, the first tap intentionally yields about 2  $\mu\text{m}$  of displacement. However, the peak impact force used for all

taps in the cutting oil case is 98 N and in the mineral spirits case 150 N. The vacuum pressure was 4.91 psi for both cases.

Figure 29 shows that the hysteresis effect is much less prominent when a thin layer of cutting oil is applied between the two surfaces. This observation seems to fit with previously mentioned knowledge of bristle deflection and presliding displacement.

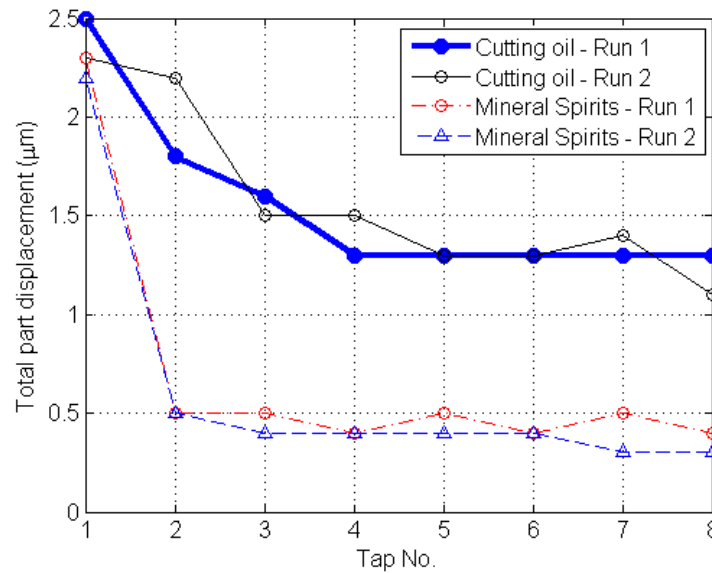


Figure 29. Direction reversal hysteresis with varying surface condition.

*Direction reversal hysteresis: Effect of vacuum pressure and normal force*

Figure 30 shows the effect of vacuum pressure (i.e. normal force) on directional hysteresis. In all three cases the first tap intentionally yields around 2 µm of displacement. Since the initial displacement is roughly the same for each case, the impact forces used for the taps at each vacuum level differs. The hysteresis effect becomes more pronounced as the vacuum (i.e. friction force) is increased. Figure 29 and Figure 30 both suggest that an increase in friction force yields an increase in the hysteresis effect.

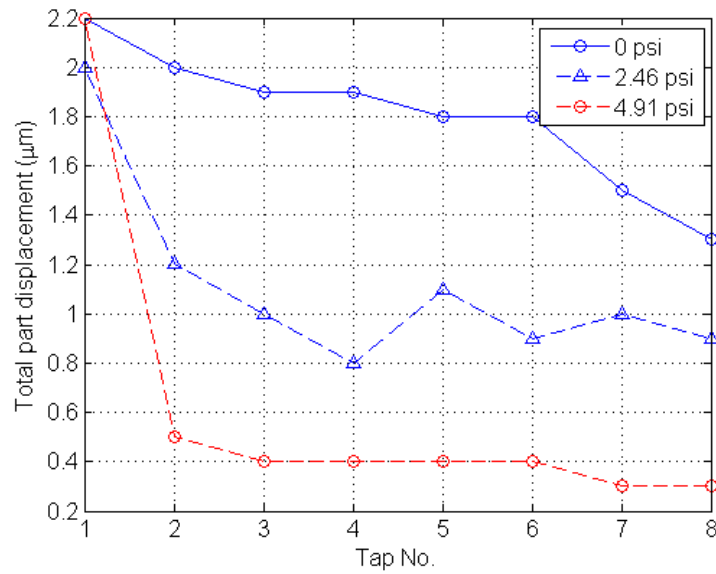


Figure 30. Direction reversal hysteresis with varying vacuum pressures.

*Direction reversal hysteresis: Displacement and impact magnitude*

Furst observed that the hysteretic effect becomes more prominent as impact magnitude (or part displacement) is decreased. This was noted by Furst as an impediment to part alignment at the micrometer level. If a tap was just slightly too large and dislocated the part past the center of rotation, a significantly different part displacement (for the same impact velocity) could be witnessed when the part was tapped again in the opposing direction.

Figure 31 shows that Furst’s observation regarding the relation between impact magnitude (or part displacement) and reversal hysteresis is not always true as the higher impact magnitude experiences a greater reversal effect.

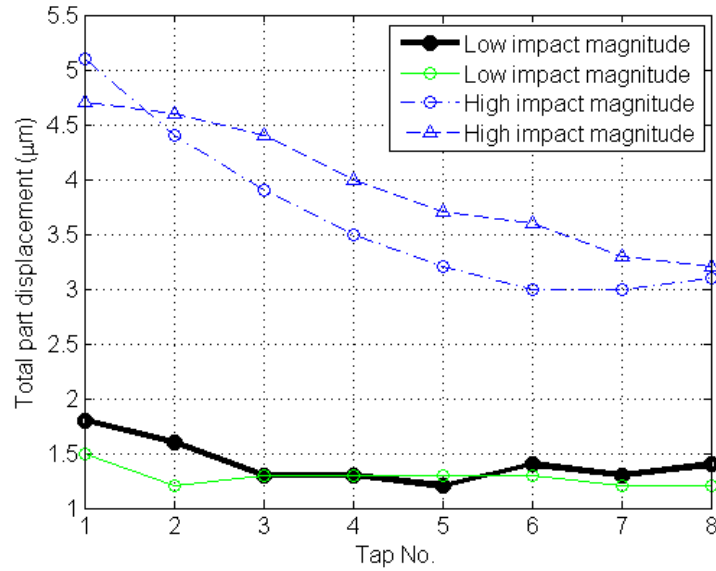


Figure 31. Direction reversal hysteresis with varying impact magnitude.

The experiments conducted to study direction hysteresis were limited in scope. The fact that the results presented here differ from those presented by Furst suggest that velocity reversal is a complex phenomenon. One of the sources of these differences could be the orientation of the part sliding with respect to gravity (Figure 6 and Figure 15). Furst’s tests involved impacting the part in the direction of gravity while the tests detailed here were in a direction transverse to gravity.

### 1.2.5 2D Newton-Hertz-Stribeck part motion model on vertical OC chuck

The 2-dimensional NHS model of part motion is similar to that from Section 1.2.3, but is applied to motion on a vertical chuck face. Figure 32 shows the FBD for 2D part motion on the OC chuck. The 2D model differs in two main ways from the 1D model. In the 2D model:

- 1) A gravity force  $F_g$  perpendicular to the impact force exists, and
- 2) The direction of friction varies throughout the part motion path.

The gravitational force is equal to the part's weight and it accelerates the part downwards once part sliding is initiated by an impacting mass. The friction force always acts in the direction opposite of part velocity and is defined by an angle  $\phi$  with respect to the horizontal in Figure 32

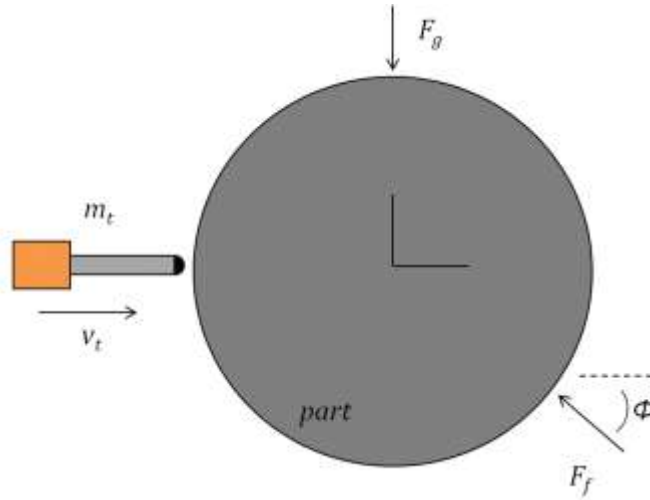


Figure 32. 2D part motion free body diagram.

The finite difference model for the 2D NHS part motion model is similar to the 1D NHS part motion model as described in Section 1.2.3. Refer to Section 1.2.1 to understand the steps in the finite difference method that calculate the tip motion and impact force. The finite difference method for calculating 2D part motion due to an impact is explained with Equations (19) – (28).

- 1) First, the friction force  $F_f(t)$  is found with Equation (19) and is a function of the static and kinetic friction forces, as well as the sum of the squares of the part velocity in the horizontal (x) and vertical (y) direction from the previous time step,  $\dot{x}_{part}(t - \Delta t)$  and  $\dot{y}_{part}(t - \Delta t)$ . Then, the direction of the friction force is found with Equation (20) following the geometry in Figure 32.

- 2) Second, the friction forces in the x and y direction are calculated with Equations (21) and (22) respectively.
- 3) Third, the acceleration of the part in the x direction is calculated with Equation (23) and is a function its mass,  $m_{part}$ , and the difference between the impact force,  $F_a(t)$ , and friction force,  $F_{f,x}(t)$ . The acceleration of the part in the y direction is calculated with Equation (16) and is a function its mass,  $m_{part}$ , and the difference between the gravity force,  $F_g$ , and friction force,  $F_{f,y}(t)$ .
- 4) Fourth, the velocity of the part in the x direction is calculated with Equation (25) and is a function of the previous velocity, part acceleration, and time step duration. The velocity of the part in the y direction is calculated with Equation (26) and is a function of the previous velocity, part acceleration, and time step duration.
- 5) Fifth, the position of the part in the x direction is calculated with Equation (27) and is a function of the previous position, part velocity, and time step duration. The position of the part in the y direction is calculated with Equation (28) and is a function of the previous position, part velocity, and time step duration.

$$F_f(t) = F_k + (F_s - F_k)e^{-\left| \frac{[\dot{x}_{part}^2(t-\Delta t) + \dot{y}_{part}^2(t-\Delta t)]^{1/2}}{0.001} \right|} \quad (19)$$

$$\phi = \tan^{-1}(\dot{y}_{part}(t - \Delta t)/\dot{x}_{part}(t - \Delta t)) \quad (20)$$

$$F_{f,x}(t) = F_f(t) * \cos(\phi) \quad (21)$$

$$F_{f,y}(t) = F_f(t) * \sin(\phi) \quad (22)$$

$$\ddot{x}_{part}(t) = [F_a(t) - F_{f,x}(t)]/m_{part} \quad (23)$$

$$\ddot{y}_{part}(t) = [F_g - F_{f,y}(t)]/m_{part} \quad (24)$$

$$\dot{x}_{part}(t) = \dot{x}_{part}(t - \Delta t) + \ddot{x}_{part}(t) * \Delta t \quad (25)$$

$$\dot{y}_{part}(t) = \dot{y}_{part}(t - \Delta t) + \ddot{y}_{part}(t) * \Delta t \quad (26)$$

$$x_{part}(t) = x_{part}(t - \Delta t) + \dot{x}_{part}(t) * \Delta t \quad (27)$$

$$y_{part}(t) = y_{part}(t - \Delta t) + \dot{y}_{part}(t) * \Delta t \quad (28)$$

Figure 33 shows results from a simulation of impact, friction, and part motion on the vertical OC chuck. Part motion (i.e. shell displacement) does not occur until the resultant of the impact force and gravitational force are above the static friction force of 290 N which decreases according to Stribeck theory. In Section 1.2.6 it is shown that these simulated curves for impact force and part displacement agree with the experiments.

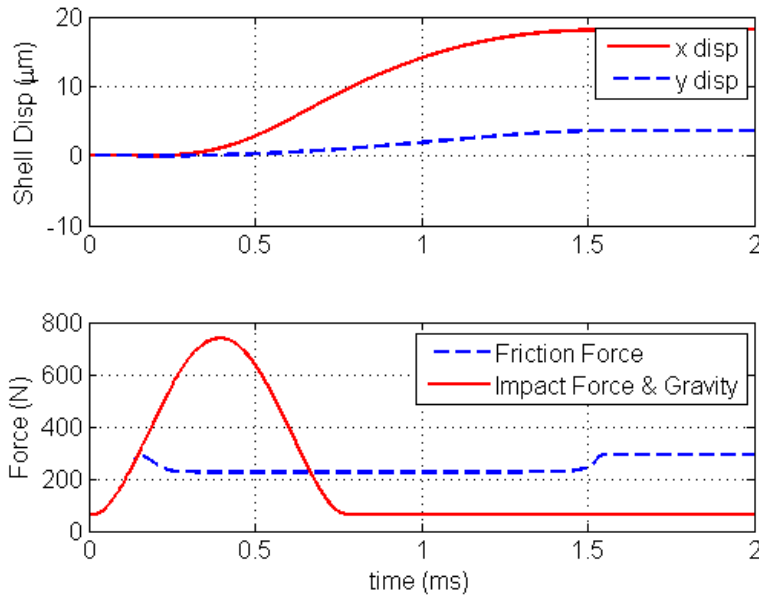


Figure 33. Simulation of impact, friction, and 2D part motion on OC chuck.

It is interesting to compare the displacements predicted for the horizontal and vertical chuck face. The magnitude of final displacements for the vertical chuck is 18.1  $\mu\text{m}$  for the horizontal direction and 3.62  $\mu\text{m}$  for the vertical direction. The final displacement in Figure 24 (1D motion) is 17.5  $\mu\text{m}$ . The same material properties, part weights, vacuum pressure, impact velocity and other values are used in the simulations for Figure 24 and Figure 33.

Thus, it is seen that the part moves more from a given impact on the OC chuck than on a flat surface with the same conditions due to the addition of the gravitational force. However, it should be noted that the smallest possible normal force in the horizontal case is the weight of the part, whereas the smallest realistic normal force on the vertical chuck must be large enough to hold the part safely to the chuck (e.g. 5X the part weight for  $\mu_k = 0.20$ ).

### *Understanding the drop angle*

The drop angle defines the ratio of the vertical to horizontal displacements of the workpiece on a vertical chuck face. The presence of a drop angle means is that if the highspot is tapped, the part will not move directly towards the center of rotation. With high drop angles values, the alignment algorithm can take an unreasonable amount of time to align a part or simply be unable to align a part if compensation is not used. The drop angle is only an issue if the part is being tapped at the side (i.e. perpendicular to gravity) on a vertical chuck. This orientation is necessary for size constraints as the device described in Section 2 cannot fit underneath a workpiece and the new device described in Section 3 was designed to be held by a standard tool holder.

Figure 34 illustrates the geometry of the drop angle. Figure 34 (a) shows a mass horizontally impacting the part when the highspot (i.e. workpiece center location) is next to the impacting tip. Figure 34 (b) shows a solid circle for the workpiece before the tap and a dotted circle after the workpiece finishes sliding. The drop angle is defined as the angle that the vector between the final and initial part center locations (points 1 and 2 in Figure 34 (b) respectively) forms with the horizontal axis of the rotational coordinate system. From Figure 34 it is clear that the drop angle can be defined with Equation (29) as the arc-tangent of the quotient of the vertical and horizontal displacements. This relation is used in the alignment algorithm to determine the drop angle value.

$$\theta_{drop} = \tan^{-1}(\Delta y / \Delta x) \quad (29)$$

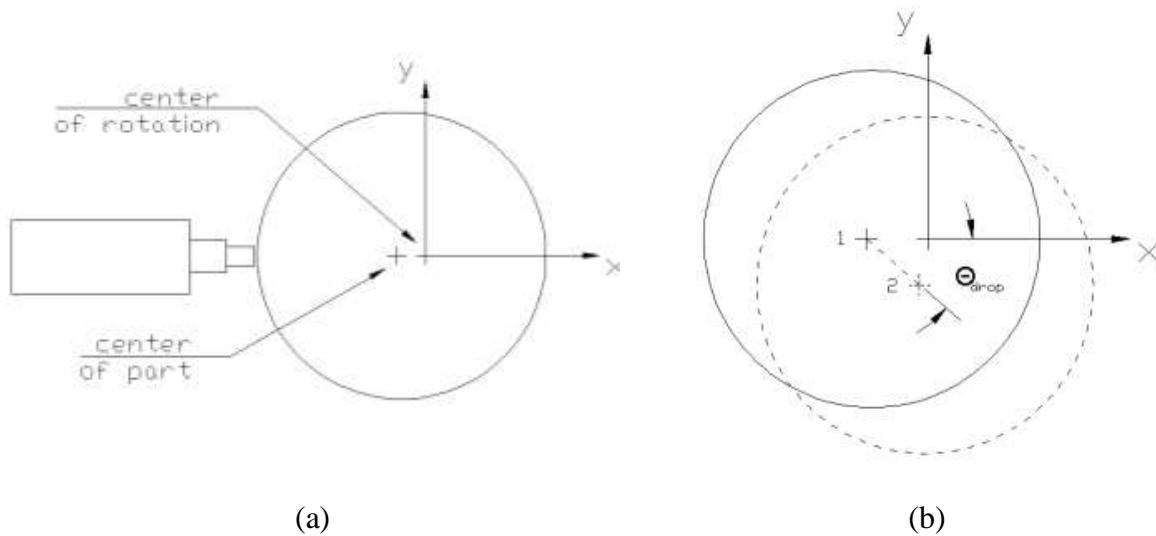


Figure 34. Basic geometry of the (a) coordinate system and (b) drop angle.

The drop angle is near  $0^\circ$  under some conditions but can approach  $90^\circ$  under other conditions. It is important to understand the effects of vacuum pressure (i.e. normal load), impact velocity, and part weight on the drop angle. These effects can be understood using the 2D NHS part motion model.

- 1) Effect of part weight on drop angle: As part weight increases, the drop angle increases as well. If the horizontal impact force profile is held constant, then this relation is easy to understand as an increase in part weight increases the gravitational force in the vertical direction. As the gravitational force (i.e. part weight) is increased relative to the impact force, an increase in the vertical displacement relative to horizontal will be observed.
- 2) Effect of impact velocity on drop angle: As the impact velocity decreases, the drop angle increases. This fact is similar to the effect from part weight. Just as increasing part weight (which increases the vertical force relative to the horizontal) increases the drop angle, decreasing the impact velocity (which reduces the horizontal force relative to the vertical) increases the drop angle.

- 3) Effect of vacuum pressure on drop angle: As vacuum pressure is increased, the impact force required to move the part a given distance is increased. If the impact magnitude is increased, then the drop angle value will decrease. It is also clear that there is a point, theoretically, when the vacuum pressure is high enough to hold the part statically, but when part motion is initiated, the kinetic force is low enough such that the part falls off the chuck. This suggests that as vacuum pressure is decreased, the drop angle approaches 90°.

The values in Table 5 show that the 2D NHS model supports the three claims described above. These simulations were carried out at the part weight, vacuum pressure and impact velocities given in Table 5. Simulations predict that decreasing the impact velocity, increasing part weight, and decreasing vacuum pressure will increase the drop angle.

Table 5. Simulations of drop angle variations.

Impact velocity (m/s)	Part weight (lb)	Vacuum (psi)	Drop angle (deg)
0.4	15	10	15.1
0.6	15	10	12.7
0.8	15	10	11.3
1	15	10	10.4
0.8	5	10	3.68
0.8	15	10	11.3
0.8	25	10	20.2
0.8	35	10	31.6
0.8	15	4	25.0
0.8	15	6	18.4
0.8	15	8	13.4
0.8	15	10	11.3

## 1.2.6 2D part motion experiments

### *2D part motion testing*

Part sliding on a vertical chuck face was studied using the experimental set-up in Figure 35. The set-up features two capacitance gages, one to measure horizontal part displacement and another to measure vertical displacement. The vertical cap gage can be adjusted horizontally to move it to the correct position. The impact hammer is pulled to contact the stop and released to achieve repeatable and directional taps. A connection to a vacuum pump allows vacuum pressure to be adjusted. This set-up is used to study the path the part takes during sliding, as well as the effect of certain conditions on the drop angle.

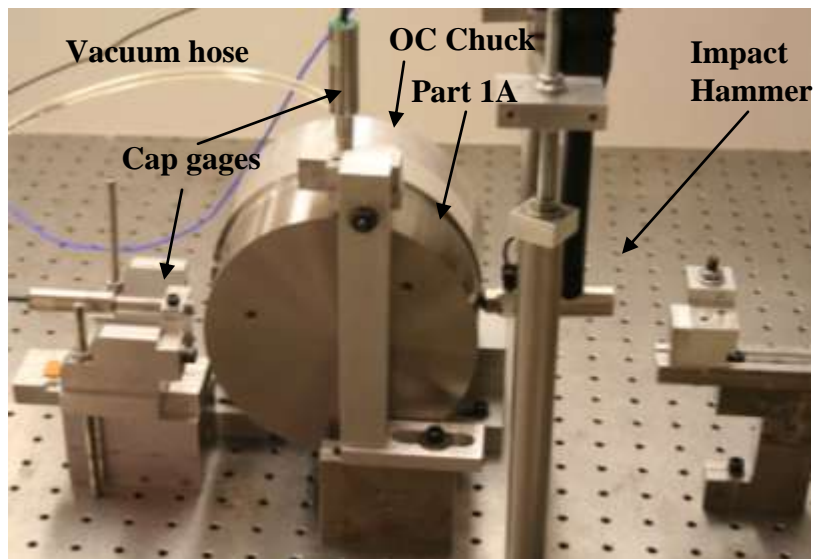


Figure 35. Experimental set-up for 2D motion measurements.

The measured part displacement for part 1A (see 0 for part list) at 4.91 psi vacuum with a plastic hammer tip is seen in Figure 36. As seen, the part moves more in the vertical direction than the horizontal direction, and appears to reach the steady-state horizontal position before reaching the steady-state vertical position. The biggest qualitative difference between Figure

36 (experimental) and Figure 33 (simulated) is the oscillations observed in the horizontal direction. These oscillations are attributed to vibration in the experimental set-up.

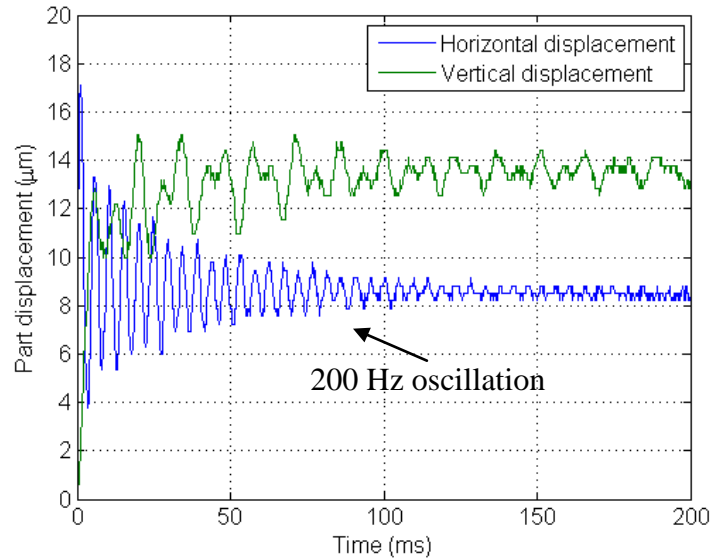


Figure 36. 2D sliding path measurement.

#### *Drop angle testing*

Large drop angles can make an alignment process take longer or even make it not possible to align a part to 2.5 μm precision by simply tapping the highspot. Table 6 shows results detailing how the drop angle changes with impact magnitude based on tests using the set-up in Figure 35. Each displacement and drop angle data point in the table is an average of four tests. As seen in Table 6, a change in peak impact force of 219 N (from 303 N to 522 N) yields a drop angle change of 19°.

Table 6. Variation of drop angle with impact magnitude.

Peak impact force (N)	Avg. horizontal disp. ( $\mu\text{m}$ )	Avg. vertical disp. ( $\mu\text{m}$ )	Avg. drop angle (degree)
303	1.33	2.38	60.9
391	7.12	7.90	47.9
431	11.7	12.2	46.3
522	19.0	17.0	41.9

Figure 37 plots the peak impact force and drop angle values from Table 6. As expected, the drop angle increases as impact velocity decreases.

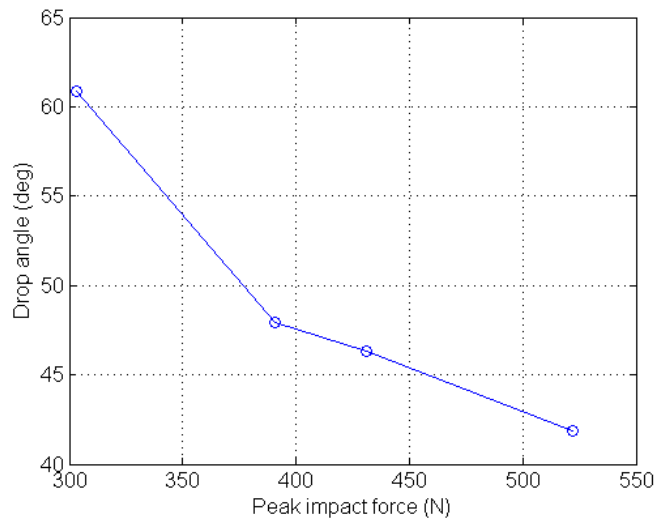


Figure 37. Drop angle variation with impact force.

Table 7 shows the how the drop angle changes with vacuum pressure based on tests using the set-up in Figure 35. Each displacement and drop angle data point in the table is an average of four tests. As expected, the drop angle increases as vacuum pressure decreases. This test also shows that it is possible to attain  $60^\circ$  drop angle.

Table 7. Variation of drop angle with vacuum pressure.

Vacuum pressure (psi)	Avg. horizontal disp. ( $\mu\text{m}$ )	Avg. vertical disp. ( $\mu\text{m}$ )	Avg. drop angle (degree)
6.87	10.0	7.9	38.5
6.38	13.9	12.9	42.8
5.89	17.7	18.9	46.8
5.40	22.9	40.1	60.2

Figure 38 plots the vacuum pressure and drop angle values from Table 7. As expected, the drop angle increases as vacuum pressure decreases. The drop angle, its effect on part alignment, and how it is compensated is discussed more in Section 4.3.2.

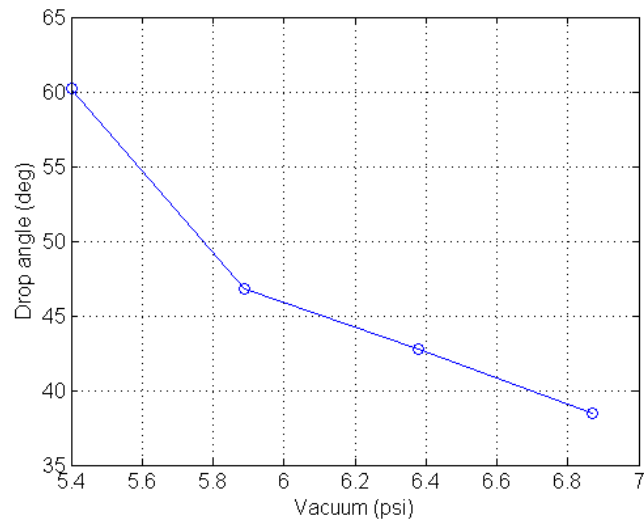


Figure 38. Drop angle variation with vacuum pressure.

### **1.3 Problem Definition for Thumper II Design**

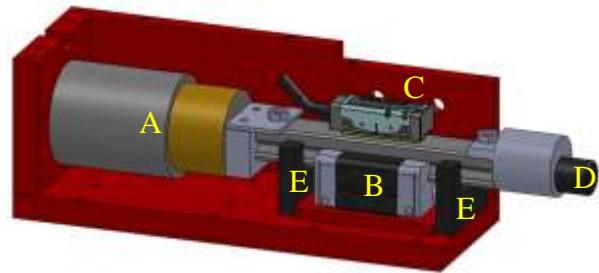
The goal of this thesis is to design an alignment system to automatically reduce workpiece runout to less than 5  $\mu\text{m}$  without human interaction or connection to the machine spindle or axis encoders. A system, called Thumper II, uses an impactor similar to Thumper I. It was designed to meet the following criteria:

- Center parts to a runout of less than 5  $\mu\text{m}$  (i.e. misalignment less than 2.5  $\mu\text{m}$ ).
- Correct initial part runout of up to 2.5 mm (IC chuck) and up to 250  $\mu\text{m}$  (OC chuck).
- Align parts weighing 5-35 lbs with 6-8 inch nominal outer diameter.
- Highly automated with little operator interaction.
- No interaction with or control of machine spindle or axes.
- Align the workpiece on the IC or OC chuck in less than 4 minutes.
- System should be compact enough to fit inside of a diamond turning machine.
- Held in tool holder, so horizontal actuation.

## 2. Thumper II: Device Design

### 2.1 Device Overview

The Thumper II device will replace a tool on a lathe and automatically center a part on a vacuum chuck. The components of Thumper II can be seen in Figure 39. Referring to Figure 39 (b), the Thumper II device includes a voice-coil actuator (A) connected to a linear ball bearing (B). An optical scale is attached to the top surface of the linear bearing. This scale can be read by the optical encoder (C). The device includes a spherical-end plastic tip (D) which contacts the workpiece. Nylon stops (E) prevent the coil from over-traveling and potentially damaging the encoder. An actual picture of the inside of the device can be seen in Figure 39 (a).



(a) Side view of Thumper II during assembly      (b) Side view 3D rendering of Thumper II

Figure 39. Picture and 3D rendering of Thumper II.

The device has two modes of operation: (1) measurement mode and (2) tap mode. In measurement mode, the magnitude and location of part misalignment is measured. In tap mode, the device taps the workpiece to move it toward the rotational center and reduce runout.

- 1) In measurement mode, the voice-coil actuator (VCA) applies a light preload (2.20 N) to hold the tip of the device against the part (Figure 59 shows Thumper II next to a

part). The displacement of the tip that occurs as the part rotates is measured by the optical encoder and these measurements are used to calculate the runout and its location.

- 2) In tap mode, the moving mass of the actuator impacts the part to move it towards the center of rotation. This involves accelerating the Thumper II mass (VCA coil + linear bearing + tip + connector pieces) to a desired impact velocity resulting in a momentum transfer between the part and impacting mass.

Figure 40 is a picture of Thumper II fully assembled. The plastic tip can be seen as well as a protective bellows that helps ensure debris does not enter Thumper II. Clear acrylic panels cover the otherwise open parts of Thumper II, allowing the user to see inside the device while keeping it sealed from the environment. The electrical wires for the encoder and VCA exit Thumper II through a small hole at the rear of the device. The aluminum structure is 2.34" x 2.00" x 6.07".

As seen in Figure 40, a rubber piece holds the VCA lead wires against the Thumper II structure. This piece ensures that the coil wires cannot be easily pulled backwards. If the wires are pulled backwards too far, the wires will exert a force on the coil assembly as it is accelerated during a tap and could result in unexpected impact velocities and an unsuccessful alignment process.



Figure 40. Thumper II automated part alignment device.

## 2.2 Component Selection

### 2.2.1 Actuator

#### *Actuator types*

The main purpose of the actuator in Thumper II is to displace the part through impulse actuation. There are many types of actuators commonly used in precision applications. Some common actuator types include piezoelectric, solenoid, and linear voice-coil motor.

Piezoelectric (PZT) actuators are commonly used in precision applications. A PZT actuator has the advantage of operating at high frequencies; e.g. 1000 Hz. A PZT actuator could potentially impact the part hundreds of times in a second to displace the part a desired distance. However, initial part runout can be as large as 2.5 mm. Thus, PZT actuators are not well-suited for this application due to their short strokes.

Linear solenoid motors can produce large forces and have millimeter scale strokes. These motors convert electromechanical energy into a mechanical force that can accelerate a load. The main disadvantage of a DC solenoid motor is that the linear mechanical force produced by the motor on the plunger varies greatly with stroke. This characteristic is undesirable as it makes it difficult to accelerate the plunger to a precise velocity, especially if distances between the actuator and part vary significantly.

The voice-coil actuator is a Lorentz-type actuator. The main advantage of the voice-coil motor is that it can be designed such that the force constant (units of Newton/Amp) is nearly linear across the entire stroke, as opposed to the solenoid which shows large variations of force versus stroke. The construction of a VCA can be seen in Figure 41. A permanent magnet is fixed around the inner surface of the ferrous cylinder. A core whose magnetic flux returns through the center of the device results in the creation of a radial magnetic field.

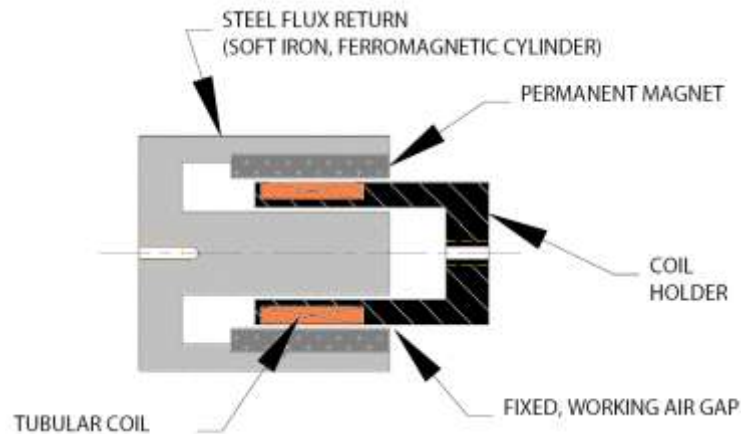


Figure 41. Linear VCA construction [18].

The force exerted on a current carrying conductor located in a magnetic field can be described by the Lorentz force law given by Equation (30). This law states that there is a force  $F$  exerted on the current-carrying wire that is equal to the cross product of the current  $I$

and length of wire  $l$  and the magnetic field  $B$ . The construction of the linear VCA results in a linear force directed along the length of the motor.

$$F = Il \times B \quad (30)$$

### *Selection of Voice-coil Actuator*

The selected voice-coil actuator for Thumper II must meet two key criteria:

- 1) Possess a large enough linear force and stroke to achieve the desired maximum impact velocity of 1.25 m/s. The specification of this upper limit is explained in this section.
- 2) Possess enough stroke to measure an initial runout of up to 2.5 mm on the IC chuck.

The maximum impact velocity for Thumper II is 1.25 m/s and was selected as this velocity is sufficient for alignment of heavy workpieces. This value was determined with the aid of Table 8 which shows the net distance a part moves due to three impacts at the specified impact velocity. These displacement values were found using the 2D NHS part motion model on the OC chuck described in Section 1.2.5 with the following conditions: vacuum (12.0 psi); static friction coefficient (0.23); kinetic coefficient (0.18); impacting mass (0.20 kg); part weight 25-35 (lbs).

The maximum runout on the IC chuck is 2.5 mm which means the maximum distance the part must be moved during an alignment process is 1.25 mm (see Figure 2). The part displaces 68.63  $\mu\text{m}$  due to three impacts at 1.25 m/s. If the part can be impacted 3 times per revolution, then it would take 18 revolutions, or 54 impacts, to displace the part 1.25 mm. Together these tap cycles would take about 2:30 (min:sec) if an 16 RPM spindle speed is used (this will become more clear in Section 5). The time of 2:30 shows it possible to align even a heavy part at high friction in less than the target 4 minutes using a peak impact of 1.25 m/s.

Table 8. Part displacements for selection of maximum impact velocity (OC chuck at 12 psi).

Part Weight (lb)	Impact velocity (m/s)	Net distance from 3 impacts (μm)
35	1.50	107.2
	1.25	68.63
	1.00	38.26
25	1.50	133.1
	1.25	84.76
	1.00	46.86

The selected actuator is listed in Appendix G. It has a stroke of 25.4 mm and peak force of 44.5 N. The maximum velocity attainable for the selected actuator can be found with the simple dynamic relation in Equation (31). In this case, the impacting mass is 0.2 kg and the useable stroke is 20 mm as some stroke must be reserved for measuring runout. The maximum possible velocity is 2.94 m/s which makes this a suitable for the desired peak force 1.25 m/s.

$$\begin{aligned}
 v_{max} &= \sqrt{2 * \text{acceleration} * \text{distance}} \\
 &= \sqrt{2 * [(44.5\text{N} - 1.4\text{N})/0.2\text{kg}] * 0.02\text{ m}} = 2.94\text{ m/s}
 \end{aligned}
 \tag{31}$$

Figure 42 shows the variation of force constant over the 25.4 mm stroke of the motor used in Thumper II. One plot in Figure 42 is from the motor datasheet, while the other two plots were experimentally collected using a load cell as in Figure 13.

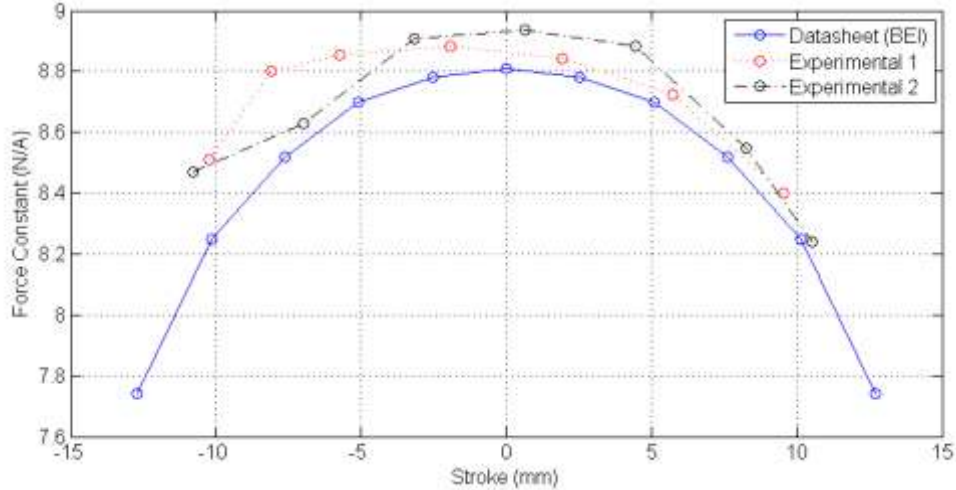


Figure 42. Variation of force constant for VCA.

### 2.2.2 Linear ball bearing

There are many options for the linear slide used in Thumper II. One possibility would be to have the rail supported with an air bearing. An air bearing would have low friction making the dynamics of the moving mass easier to understand and apply. The main disadvantage of an air bearing is the high-pressure air source, perhaps making Thumper II overly complex. Thus, a precision linear ball bearing was selected to be the most appropriate choice.

The selected linear slide made by THK is seen in Figure 43. The key feature of the bearing is its unobstructed surface (the bottom surface in Figure 43). This surface can hold an encoder scale so that rail displacement can be measured. The selected THK combination includes a stainless steel profile rail and a ball bearing block. The end seals provide protection of the bearing from debris on the rail. Both end seals are removed in Thumper II to reduce the frictional drag experienced by the rail. Since the rail is located in a sealed Thumper II device, there is little concern for debris affecting the performance of the bearing. The selected bearing is detailed in Appendix G.

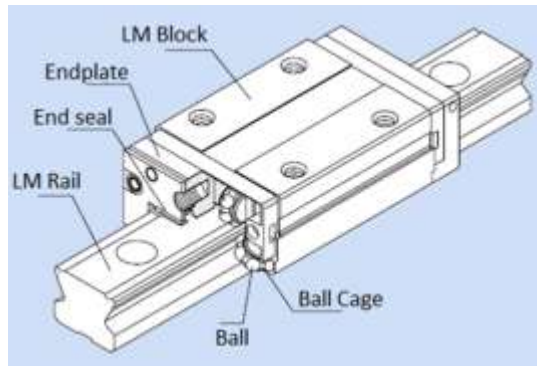
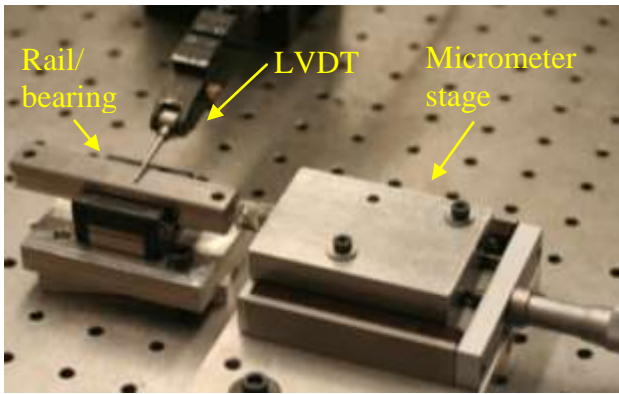
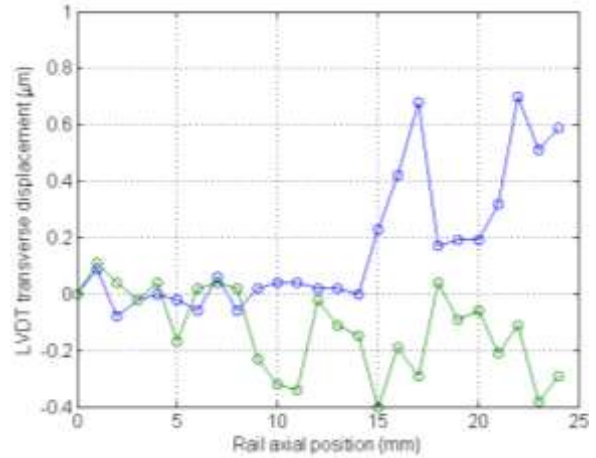


Figure 43. THK SSR-style caged-ball bearing and rail [19].

Some key considerations for selecting the appropriate linear rail include the straightness of motion, length, and mass. The straightness value for the rail is important as poor readings from the selected encoder would result if the straightness is too high. The straightness value gives the magnitude of the vertical motion of the top surface of the rail with respect to the block as the rail displaces axially. The selected rail has a published straightness of  $2\ \mu\text{m}$ . The plot in Figure 44 (b) shows a measurement of straightness to verify this value. An LVDT measured the vertical change in the top surface of the rail as it was displaced axially with a micrometer stage as seen in Figure 44 (a). Figure 44 (b) shows that the rail meets the encoder criterion of a running parallelism less than  $50\ \mu\text{m}$  to ensure accurate measurements are possible.



(a) Experimental set-up



(b) Results of measurements

Figure 44. Rail straightness measurements.

Since 25.4 mm of stroke was selected for the actuator, a minimum length of the rail is 25.4 mm greater than the length of the bearing block. In fact, the length of the rail is actually about 2 inches longer than the length of the bearing block to ensure the rail-coil connector piece and rail-tip do connector piece do not impact the encoder at the either end of travel.

#### *Selection of rail mass*

The mass of the rail is an important consideration since the mass and speed of the impacter have a direct influence on part displacement. To understand the relation between kinetic energy, impacting mass, impacting velocity, and part displacement, it is first important to understand the basics of the acceleration phase of the coil. A simplified diagram of the assembly mass  $m_i$  being accelerated over a stroke  $d$  can be seen in Figure 45.

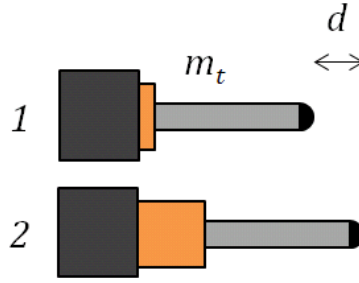


Figure 45. Simplified diagram of assembly mass acceleration.

A given voice-coil actuator has a fixed stroke  $d$  and peak linear force  $F_{peak}$ . Thus, the peak impacting kinetic energy of the impacting mass is fixed as given in Equation (32).

$$KE_{peak} = \frac{1}{2} m_{tip} v_{tip0}^2 = F_{peak} d \quad (32)$$

Equation (52) from 0 defines part displacement as a function of impacting velocity  $v_{tip0}$ , impacting mass  $m_{tip}$ , coefficient of restitution  $e$ , part mass  $m_{part}$ , and a nominal friction force  $F_f$ . The value for  $v_{tip0}$  in terms of  $KE_{peak}$  from Equation (32) can be substituted into Equation (52) to yield an equation for part displacement.

$$\delta = \frac{m_{part}(1 + e)^2 m_{tip}^2 v_{tip0}^2}{2F_f (m_{tip} + m_{part})^2} \quad (33)$$

Equation (32) can be plotted to show how part displacement changes as impacting mass changes for a constant kinetic energy. A plot of part displacement variations at a kinetic energy of 0.445 Nm (i.e. 44.5 N \* 10.0 mm) for various friction ( $F_f$ ) and part weight values can be seen in Figure 46. Figure 46 shows that increasing the impacting mass will increase the part displacement for all cases until it reaches 2.25 kg. However, 2.25 kg is much greater than could be used in Thumper II. Thus it can be concluded that for the realistic range of Thumper II impacting mass, increasing mass will increase the part displacement.

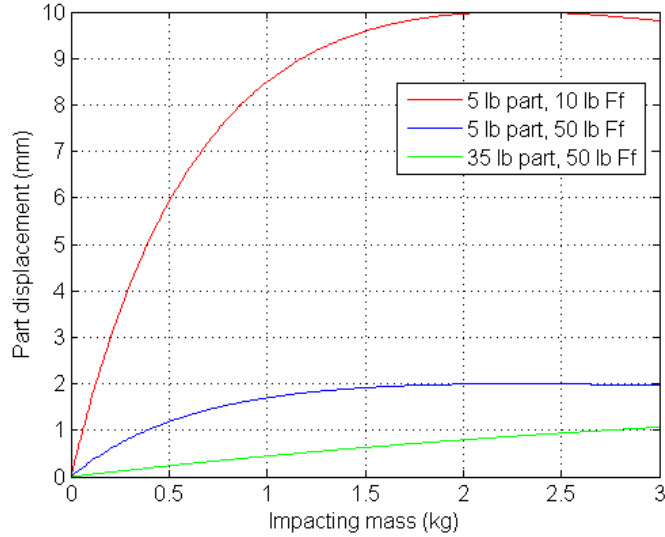


Figure 46. Displacement variation by increasing impacting mass for constant kinetic energy.

Deciding upon the ideal impacting mass includes a consideration of an important tradeoff. As seen in Figure 46, increasing the impacting mass has the advantage that Thumper II will have the ability to displace a heavy part at high friction a longer distance for a given VCA. However, increasing the impacting mass makes it more difficult to displace a light part at low friction. Velocity sensitivity is an indication of the relationship between the change in impact velocity and the resulting change in part displacement. Low velocity sensitivity indicates that a small change in impact velocity results in a large change in part displacement. For precise positioning of a light part, it is desired to have high velocity sensitivity.

To choose a proper impacting mass, it is necessary to consider this tradeoff and Table 31 and Table 32 in Appendix H were used for this purpose. As indicated in Appendix H, an impacting mass of 0.35 kg is too large as it yields a low velocity resolution and an impacting mass of 0.15 is too light to displace a heavy part at high friction a large enough distance to result in a quick alignment process.

The selected rail is 0.110 kg and the coil is 0.060 kg. When combined with the tip and connecting pieces, the impacting mass is about 0.20 kg. Successful testing of Thumper II

suggest that an impacting mass of 0.20 kg can displace heavy parts but possesses a desirable velocity sensitivity.

### **2.2.3 Position Encoder**

There are many types of position encoders available for part measurement and some are listed here:

- 1) LVDT: This is a common device used in the manual method of part alignment and its operation was explained in Section 1.1.3. The main disadvantage of the LVDT for Thumper II is its size and difficulty with incorporating into a compact tapping device.
- 2) Capacitance gage: A capacitance gage can be seen in Figure 35. The capacitance gage is positioned near a metallic object to be measured. Changing the gap between the capacitance gage and object changes the electrical capacitance between the two and the gage uses this capacitance change to derive relative displacement. The main disadvantage of the capacitance gage is its limited measuring range which is typically much less than the maximum runout of 2.5 mm.
- 3) Incremental optical encoder: Some optical encoders use Moiré fringe patterns to discern relative displacement between the encoder and scale. Figure 47 shows the creation of Moiré fringes. A single grating is seen in Figure 47 (a). Figure 47 (b) two gratings; one grating of the same pitch as another which is tilted by an angle  $2\alpha$  resulting in distinct areas of constructive and destructive interference. If the two gratings in Figure 47 (b) are of equal spacing, then there is a periodic spacing of the interference zones equal to  $\lambda/2 \sin\alpha$  [20]. The electronics of the selected encoder uses this concept to discern relative displacement of the two gratings.

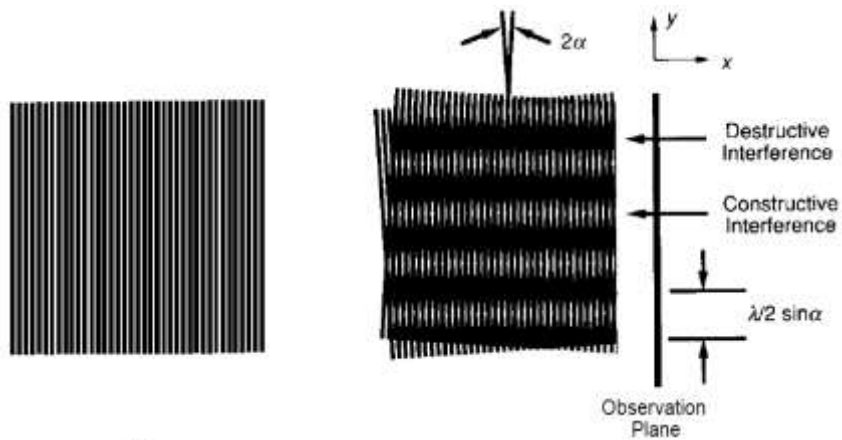


Figure 47. (a) Single line grating and (b) Moiré fringe between two straight-line gratings of same pitch tilted with respect to each other [20].

Figure 48 shows the construction of the selected encoder system. The scale placed on the rail has a  $20\ \mu\text{m}$  pitch of surface features and acts much like the lower grating seen in Figure 47 (b). The encoder contains a second grating in the read head. An infrared LED illuminates the surface while a photodetector detects the interference pattern and outputs an appropriate signal. This signal is sent to the encoder interpolator which converts the sine/cosine quadrature signal to square wave quadrature that can be interpreted by a quadrature decoder.

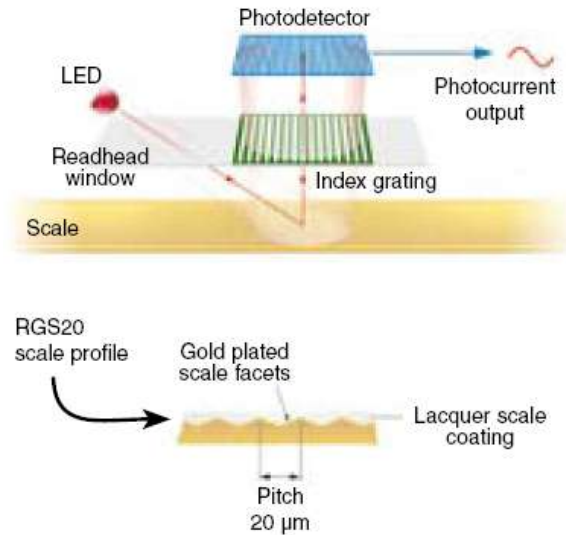


Figure 48. Construction of Renishaw’s incremental optical encoder [21].

Some key considerations for the position encoder are its resolution and interface clock speed. Since the smallest measurement of interest is  $2.5\ \mu\text{m}$  (i.e. misalignment goal), it is desired for the resolution of the encoder to be at least one-tenth of  $2.5\ \mu\text{m}$ , or  $250\ \text{nm}$ . The selected encoder has a resolution of  $50\ \text{nm}$ . The clock speed of the interpolator (separate from the readhead) determines the maximum velocity that can be measured. The selected interpolator (which converts sine/cosine signal to quadrature) can only operate up to about  $0.70\ \text{m/s}$ . As a result, the encoder cannot read the rail position when tap velocities exceed  $0.70\ \text{m/s}$  and thus the acceleration of the coil for a tap in Thumper II is an open-loop process based on empirical parameters.

### 2.3 Construction and integrating components

Figure 49 details the construction of the Thumper II structure. Appendix H shows the 6 structural pieces that make up the Thumper II structure. The numbers on Figure 49 (#/6) refer to the page numbers on the drawings in Appendix H. The VCA bolts to part 1/6 in Figure 49. As seen in Figure 39 (a), two bolts connect the readhead to part 3/6 in Figure 49. There are

multiple challenges with designing the structure for the Thumper II device and integrating its components in a compact manner.

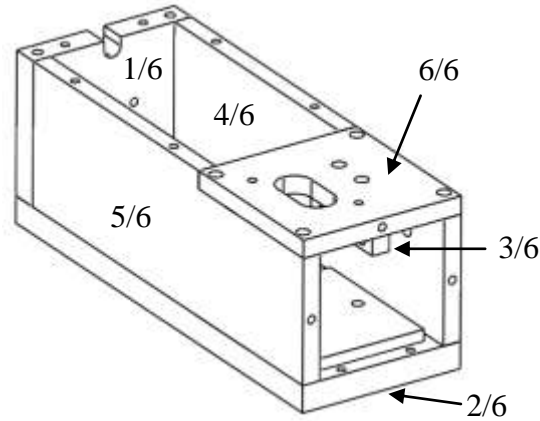
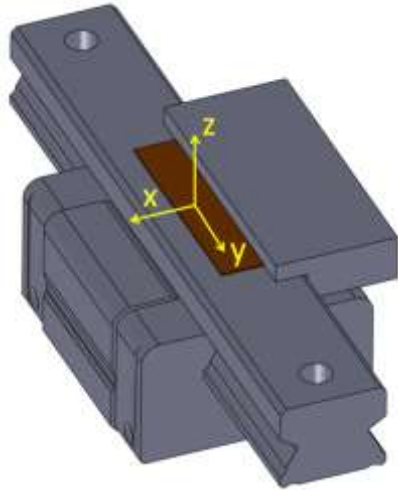


Figure 49. Details of Thumper II construction.

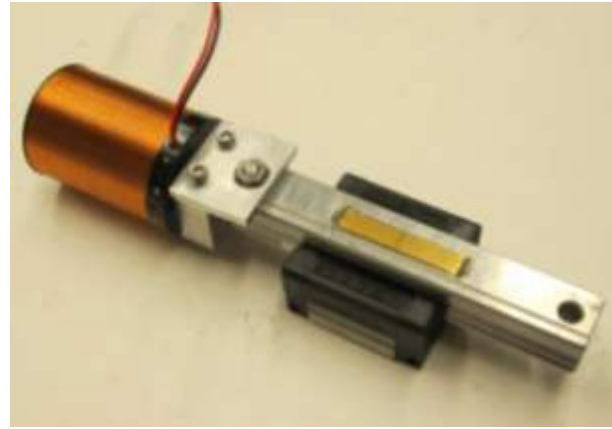
### *Construction*

The scale was installed on the rail with relative ease. The first task was to remove the plastic from the bottom of the scale (revealing a sticky surface) and place the scale on the rail in the correct place. To ensure the rail would be installed in the correct location and orientation, the simple guide seen in Figure 50 (a) was used. The scale was simply placed down against the guide. This guide ensured that the scale was in the correct  $x$  location and aligned in the  $z$  orientation. The device was placed in the correct  $y$  location by aligning the end of the scale with a scribe mark engraved precisely from the end of the rail. The scale is 30 mm long, even though the end stops only allow about 25 mm of motion, which is the stroke defined for the VCA. The extra length of the scale makes the  $y$  position of the scale more flexible.

Once the scale was in place, a small amount of Renishaw adhesive (Araldite AV 138M-1/HV 998) was applied to the ends of the scale. This helps to prevent the scale from peeling off due to temperature fluctuations or stresses. Figure 50 (b) shows the scale and coil installed on the rail, and the adhesive on the ends of the scale is visible.



(a)



(b)

Figure 50. Guide used in scale installation (a), scale and coil installed on rail (b).

The tolerances from the encoder datasheet give an understanding of the importance of placing the scale and readhead correctly. The yaw tolerance (i.e.  $z$  orientation) of the readhead with respect to the scale is  $\pm 0.4^\circ$ . The  $x$  center of the readhead must be within  $500\ \mu\text{m}$  of the  $x$  center of the scale. The pitch and roll tolerances of the readhead with respect to the scale is  $\pm 1.0^\circ$ . Lastly, the rideheight of the readhead (i.e. distance between bottom of readhead and top of scale) must be  $2.1\ \text{mm}$  with a tolerance of  $\pm 150\ \mu\text{m}$ .

To verify that the readhead and scale were properly installed, the displacement of the rail was compared with the displacement of a precision diamond turning machine (DTM) axis. To perform this test, a light preload from the VCA allowed Thumper II to contact a rigid surface on the DTM spindle. Then, the axis of the machine was moved, and the new axis location and the new Thumper II rail location were measured. This data shows that after the DTM  $x$ -axis encoder identified a translation of  $22.1403\ \text{mm}$ , Thumper II had displaced  $22.1392\ \text{mm}$  which is only a  $1.09\ \mu\text{m}$  difference. This suggests that Thumper II is set-up correctly and providing accurate measurement values.

Table 9. Thumper II encoder compared with precision DTM axis.

ASG DTM x-axis ( $\mu\text{m}$ )	Thumper II ( $\mu\text{m}$ )	Difference ( $\mu\text{m}$ )
0.0	0.0	0.0
- 2,520.9	- 2,520.7	- 0.19
- 4,607.9	- 4,607.7	- 0.21
- 7,666.2	- 7,665.4	- 0.87
- 11,556.6	- 11,555.4	- 1.27
- 14,520.2	- 14,519.0	- 1.29
- 17,969.3	- 17,967.9	- 1.39
- 20,486.8	- 20,485.9	- 0.88
- 22,140.3	- 22,139.2	- 1.09

### *Design Notes*

The aluminum structure of Thumper II is 2.34” x 2.00” x 6.07”. The limitations of the width and height of the structure are the size of the components. As seen in Figure 39, there is little extra space in the width or height direction.

Understanding the requirements on the length of Thumper II involves more consideration. The rail needs to be at least 25.4 mm longer than its block to produce the desired 25.4 mm stroke. The rail needs to be even longer so that the connector pieces do not hit the encoder readhead. This is illustrated with Figure 51 which shows Thumper II fully retracted and fully extended. The coil-rail connector nearly touches the encoder when the device is fully extended and the rail-tip connector nearly touches the encoder when the device is fully retracted. The coil-rail connector fits underneath the readhead cable to reduce the overall required length.

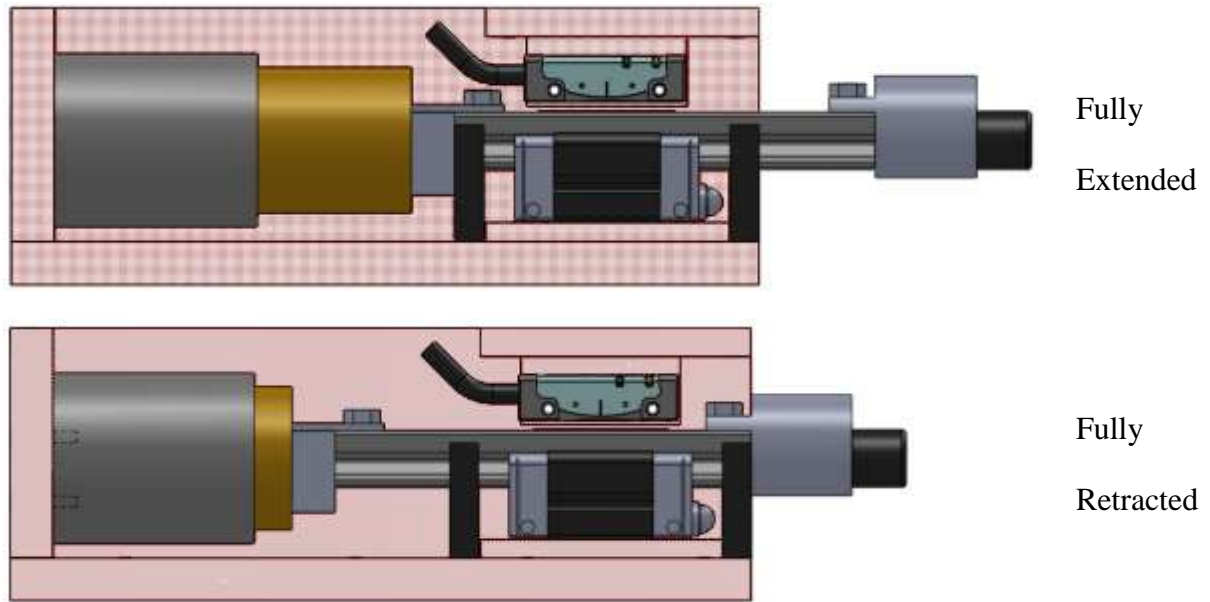


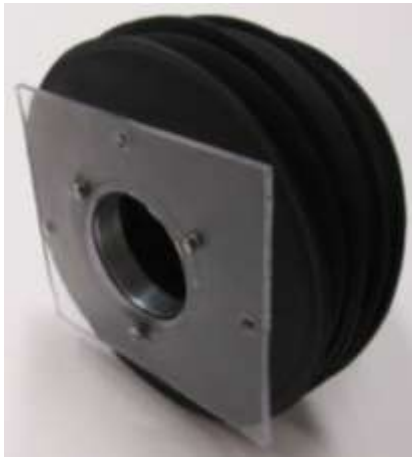
Figure 51. Thumper II fully retracted and fully extended.

One key factor in the length of Thumper II is the length of the connector between the VCA coil and the rail. The device could be made shorter by eliminating this connector and directly bolting the coil (which has through holes) to holes on the end face of the rail. While eliminating this connector would reduce the device's length, doing so would result in larger problems. This is because the rail is magnetic and the Aluminum connector seen in Figure 39 acts as a magnetic flux gap. If the rail is connected directly to the coil, then when the coil is fully retracted the rail becomes only a few millimeters away from the VCA magnet and a strong magnetic force attracts the rail to the magnet. This undesirable force on the rail would make accelerating the coil troublesome.

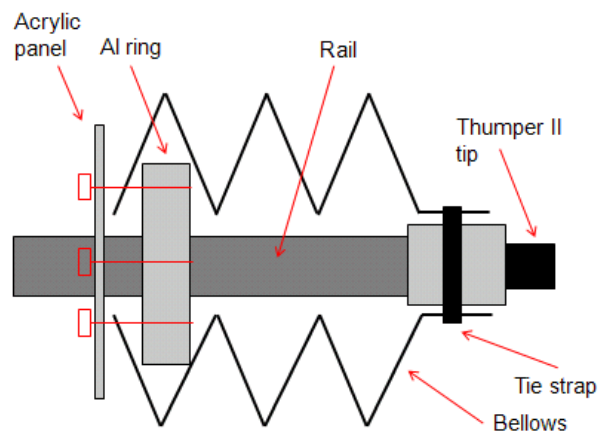
The structure and connector pieces were created such that the centerlines of the VCA coil, rail, and tip are all collinear. This requires the stepped-up area for the rail block to sit on (see Figure 39) and it also requires positioning the tip off-center from the piece that connects it to the rail. The nylon tip of Thumper II was diamond turned to a diameter of 50 mm.

### *Bellows*

The bellows used in the final version of Thumper II is a highly flexible polyurethane bellows. The bellows has a 0.01 inch wall thickness and inner and outer diameter of 1 inch and 3 inches. The bellows is fixed to the Thumper II structure as shown in Figure 52 (b). An aluminum ring with 1" ID and 1.5" OD is inserted in the bellows and the aluminum ring has three tapped bolt holes. The ring is bolted to a plastic panel with part of the bellows in between the ring and panel. As shown in Figure 52, the front of the bellows has a round 1" diameter cuff which is sealed to the aluminum connector piece with a tie strap.



Picture of bellows, panel, and aluminum ring



Drawing of bellows construction

Figure 52. Construction of bellows.

### *Bearing resistance*

The ball bearing has friction which adds to the inertia of the moving mass increasing the force needed to achieve a given impact velocity. The bearing friction force was determined with the test in Figure 53. The bearing block was fixed vertically so that after enough extra mass was added, the rail would slide out of the block. Thus, the static friction force is the

gravitational force of the combined mass of the rail  $m_1$  and added mass  $m_2$  when the rail slides.

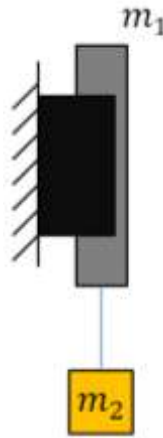


Figure 53. Simple bearing resistance test.

The rail has a mass of 110 g and does not slide from the block from its own weight. The value of the added mass which caused the rail to slide in the block was 400 g with the block end seals installed and 30 g without the end seals installed. The end seals are 1.65 mm thick pieces of plastic at the end of the bearing (see Figure 43) that wipe debris off the rail so it does not enter the bearing. The end seals are not installed in Figure 39. Thus, the resistance force with and without seals is 5.0 N and 1.4 N respectively. The 5.0 N force with the end seals installed is much higher than desirable. This is a high force for the VCA to overcome and would severely affect impact dynamics. For this reason the bearing block end seals were removed. Since Thumper II housing is sealed, removing the end seals will have a negligible effect on bearing cleanliness.

### 3. Thumper II: Control System Design

#### 3.1 System Overview

The system that controls the Thumper II device is intended to be located outside of the turning machine. A schematic of the Thumper II control system can be seen in Figure 54. A microcontroller is the centerpiece of the system. It creates analog voltage signals with on-board digital-analog convertors (DAC) that are amplified to accelerate the impacting mass to the desired velocity for impact with the part. The microcontroller includes two quadrature decoder integrated circuit (IC) chips to collect encoder data while in measurement mode. The microcontroller software includes a least squares circle fit function used to evaluate raw measurement data and locate the part center, as well as the tap algorithm that determines the magnitude and location of taps.

The system is operated with a GUI application installed on a personal computer (PC). The PC and microcontroller communicate serially. The GUI program allows the user to input information, such as part weight and spindle speed, which the microcontroller uses in the alignment process. The communication also includes transmission of information such as runout magnitude and status updates from the microcontroller to the PC for display to the operator.

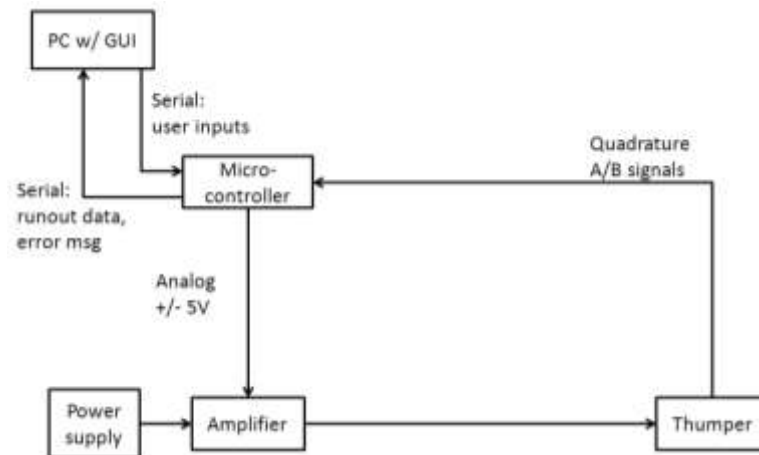


Figure 54. Schematic of Thumper II control system.

## 3.2 Component Selection

### 3.2.1 Microcontroller

The C-coded microcontroller is the central processing and decision point of the control system. One of the reasons that a dedicated microcontroller external to the PC was selected is that many aspects of the alignment program need to be precisely timed. Programmable interrupt service routines and other time functions ensure that the program can precisely track time and perform time sensitive procedures such as the tapping procedure discussed in Section 4.2.3.

The microcontroller is pictured in Figure 55. The main microcontroller (586-P) can be seen as the top board and includes an AM5<sub>x</sub>86 CPU processor. A slightly larger expansion board (P50) fits underneath the microcontroller and it contains the two quadrature decoder IC chips. The quadrature signal from the encoder is decoded using an on-board IC chip (Hewlett Packard HCTL-2020).

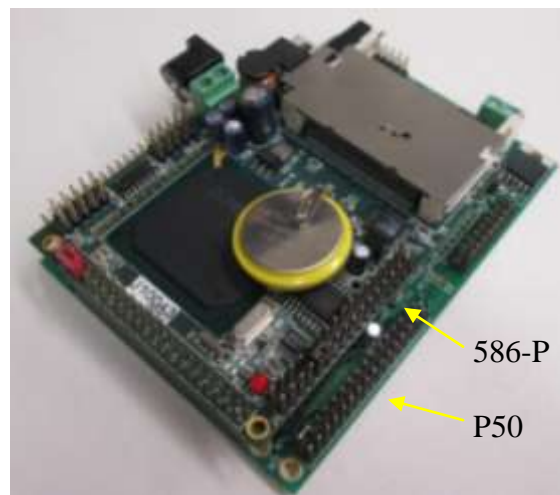


Figure 55. TERN 586-P Microcontroller on top of the TERN P50 expansion board.

The microcontroller performs many actions for the Thumper II system, including the following:

- Decode and store time-sensitive runout data from the rail position encoder,
- Track the angular position of the spindle using a known spindle speed and precise clock reference,
- Manipulate the runout data using a least-squares circle fit function to determine the location of the high spot,
- Create time-sensitive tapping sequence and send to the amplifier, and
- Execute the adaptive tapping algorithm that determines when and how hard to tap the workpiece.

### **3.2.2 Amplifier and Power Supply**

All power amplifiers receive an input signal and amplify its power (voltage and/or current depending on operation mode) for use by a motor or other device. A power supply converts the voltage from the wall to a DC voltage. The amplifier modulates this power and outputs some portion to the load depending on how much power is commanded by the input signal to the amplifier.

Power amplifiers differ in 3 ways: (1) the type of input signal, (2) how the input signal is interpreted, and (3) and type of output signal the amplifier produces.

- 1) The input signal is usually one of two types: analog voltage signal or a digital pulse-width modulated (PWM) signal. The main advantage of an amplifier designed for a PWM input signal is the availability and low price compared to an analog signal. Including a DAC device needed to produce an analog signal can add cost and complexity to the amplifier. A PWM signal also contains no errors due to digital-analog conversion as the PWM signal is a digital signal. Amplifiers designed for

- PWM input are not nearly as common as analog input amplifiers, and, for this reason, an analog amplifier was used for Thumper II.
- 2) How the amplifier interprets the input signal is one of two types: desired voltage across the load (Voltage mode), or desired current through the load (Current mode). If an amplifier receives a 2V analog input signal, it will interpret this signal as either a desired voltage across the load (the output voltage is equal to the input voltage multiplied by a known gain value), or the signal is interpreted as a desired current through the coil (the output current is equal to the analog voltage signal multiplied by a scaling factor set within the amplifier). In Voltage mode, the amplifier applies the desired voltage until a new input command is issued. Thus, in Voltage mode, current will vary if changes in the load occur. In current mode, the amplifier monitors the output current, and adjusts the applied voltage to maintain the commanded current level. Thus, in Current mode, applied voltage will vary if changes in the load occur. The Thumper II system operates in Voltage mode, and this reason for this is discussed in Section 4.2.1.
  - 3) The type of output signal the amplifier produces is one of two types: linear or switching (i.e. PWM). A linear voltage output amplifier applies a constant voltage across the load according to the command signal. The switching voltage output amplifier (also known as type-D amplifier) switches at a high frequency (the selected amplifier switches at 33 KHz) between 0V and the nominal power supply voltage (80V for the selected power supply), and the average voltage across the load is equal to the command voltage. Switching amplifiers are typically less expensive as they do not linearize the output voltage. Switching amplifiers are usually more energy efficient than linear amplifiers as well. However, the intermittent use of the amplifier in the Thumper II yields no significant efficiency gains. The amplifier selected is a switching output type that is rated for voice-coil actuators.

With the type of amplifier selected, power requirements must also be met for the selected amplifier and power supply. A proper amplifier and power supply must be able to supply enough power to achieve desired system performance within operating limits.

The required system voltage can be found using Equation (34). The required system voltage  $V_{req}$  is the sum of the resistive voltage drop  $V_R$  and the back electromotive force  $V_B$  at maximum desired coil velocity  $v$ . The voice coil is rated at a maximum of 5 Amps and 46 Volts and has a measured resistance of 9.2  $\Omega$ . The value  $K_B$  is the motor's back electromotive force (back EMF) constant and the peak velocity of 1.25 m/s is drawn from simulations (see Section 2.2.1) looking at the velocities needed to move a 35 lb part at high vacuum pressure.

$$V_{req} = V_R + V_B = iR + vK_B = 5A * 9.2\Omega + 1.25 \frac{m}{s} * 8.79 \frac{Vs}{m} = 57.0 V \quad (34)$$

Equation (34) shows that the power amplifier must be able to supply 57.0 V at 5 A to results in the maximum desired coil velocity. It is recommended by the amplifier and power supply manufacturer that they be rated at least 10% above the system voltage requirement, yielding a requirement of at least 63 V [22]. The current requirement for the amplifier and power supply is implicit from Equation (34), and with a 10% current safety buffer, a 5.5A current requirement is needed for the amplifier and power supply.

The amplifier selected is of:

- A linear analog voltage input signal to use with the DACs on board the microcontroller,
- Voltage mode operation (though the amplifier has Current mode capacity) as it is better suitable for velocity control, and
- Switching output type as this is a least expensive type.

Selecting a power supply is simple once an amplifier has been chosen. The selection process includes three main considerations: amplifier over voltage limit, system power requirements [22], and electrical isolation. The AMC 12A8 amplifier has an over voltage limit (greatest

power supply voltage that should be used with the amplifier) of 86 V. This means that the power DC supply voltage should not exceed 86 V. It is recommended to have a 10% voltage safety buffer such that the selected power supply should be less than 77V.

The power supply must meet the same voltage and current requirements given. It is also important to ensure there is electrical isolation between the AC line from the wall and the signal pins on the amplifier [22]. Advanced Motion Controls makes the selected amplifier (12A8) and power supply (PS16180-L) which are detailed in Appendix G.

### **3.2.3 Graphic User Interface**

The GUI for Thumper II was developed in Microsoft's Visual Studio Express 2010 using the VB.NET, an object-oriented version of the Visual Basic language. A screenshot of the GUI is seen in Figure 56. The code for this GUI can be found in Appendix L. As mentioned earlier, this interface serves three main purposes:

1. Aid in positioning Thumper II with respect to the workpiece,
2. Allow the user to send information (e.g. spindle speed) to the microcontroller,
3. Display runout feedback from Thumper II measurements.

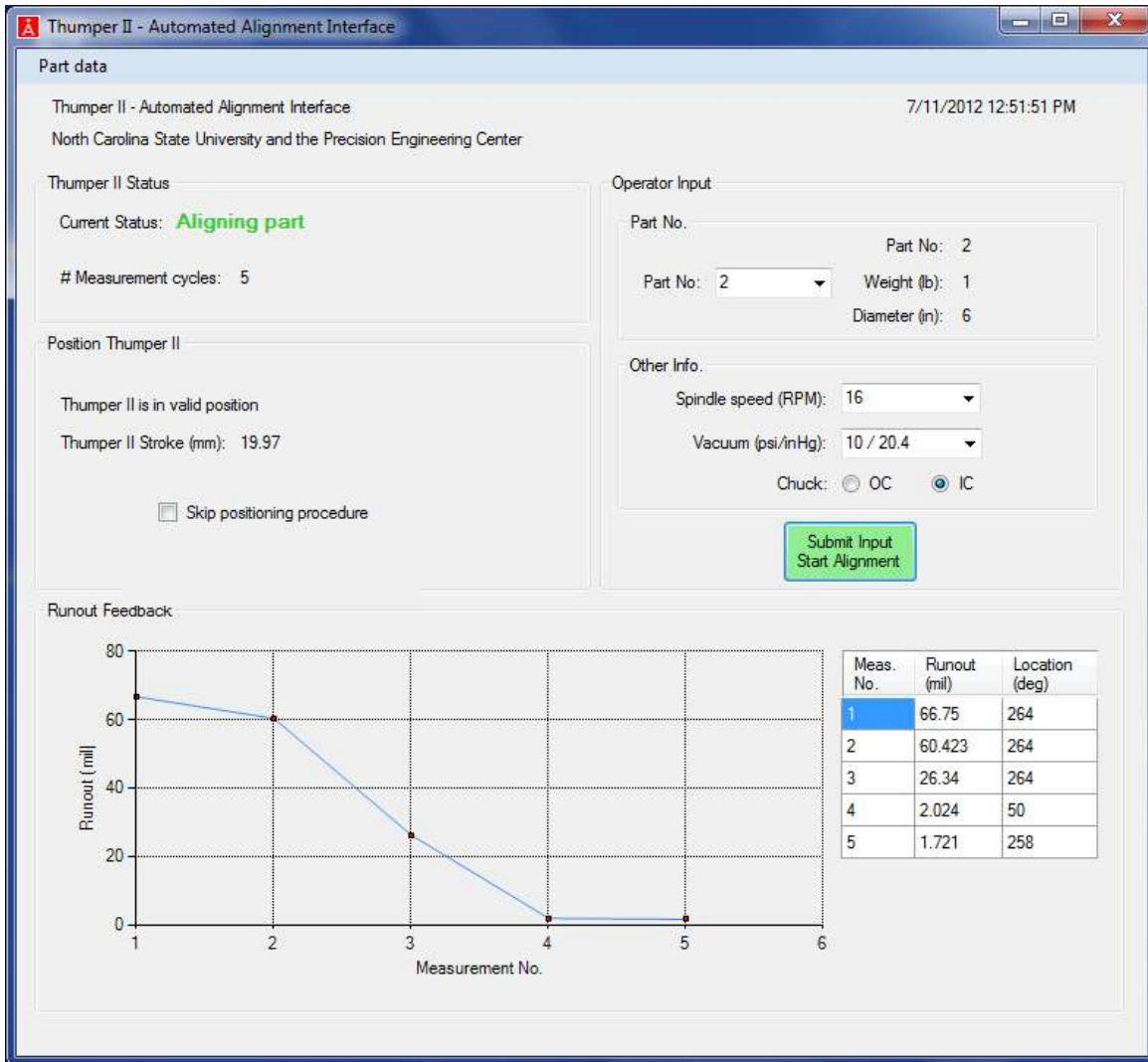


Figure 56. Thumper II GUI screenshot.

In the ‘Thumper II Status’ box in the upper left of Figure 56, status updates inform the operator what the microcontroller is doing. For example, the microcontroller could be “Waiting for user input” or “Aligning part.”

In the ‘Position Thumper II’ box in the middle left of Figure 56, the user can position Thumper II with respect to the as described in Appendix L.

In the ‘Operator Input’ box in the upper right of Figure 56 there are options for the user to enter part characteristics and spindle speed. The ‘Part No.’ dropdown box is populated from a text file in which each row contains a part number, weight in pounds and the diameter in inches with comma delimiters. The microcontroller uses this value to determine the relative location of collected runout data points, the location of the high spot, and when to tap the part. Lastly, the user can input vacuum pressure and the chuck type. The initial values sent from the GUI to the microcontroller are: part weight, friction force, chuck type, and spindle speed. Friction force  $F_f$  is calculated with the Equation (35) and is a function of vacuum pressure  $P$ , friction coefficient  $\mu$ , and vacuum area  $A$  which is a function of part diameter  $D$ .

$$F_f = \mu PA = 0.25 * P \left( \frac{\pi}{4} D^2 \right) \quad (35)$$

In the ‘Runout Feedback’ box in Figure 56, a line graph displays the measured runout, i.e. twice the misalignment, value for each measurement in mils (i.e. 0.001 inch). These runout values are displayed in a table along with the runout angular location.

### 3.2.4 Thumper II electrical packaging

The components of the control system have been arranged in a portable package. This allows Thumper II to be easily transported from one machine to another if desired. Electrical disconnects on the enclosure and device make it possible for Thumper II to be transported between machines.

The front panel of the enclosure can be seen in Figure 57. One switch controls the power for the entire enclosure. One connector is used for the Thumper II encoder and another is used for the Thumper II motor. A momentary switch is used to reset the microcontroller (and its software) and the LED is green when the microcontroller is powered on.



Figure 57. Front panel of electrical enclosure.

The inside of the electrical enclosure can be seen in Figure 58. The enclosure houses the microcontroller, power supply, and amplifier. The flat aluminum panel below the microcontroller helps to reduce RF noise coming from the 80V power supply. The cable for serial communication exits through a hole at the rear of the enclosure (not pictured). A wiring diagram for the enclosure can be seen in Appendix J and includes wire label and pin number information.

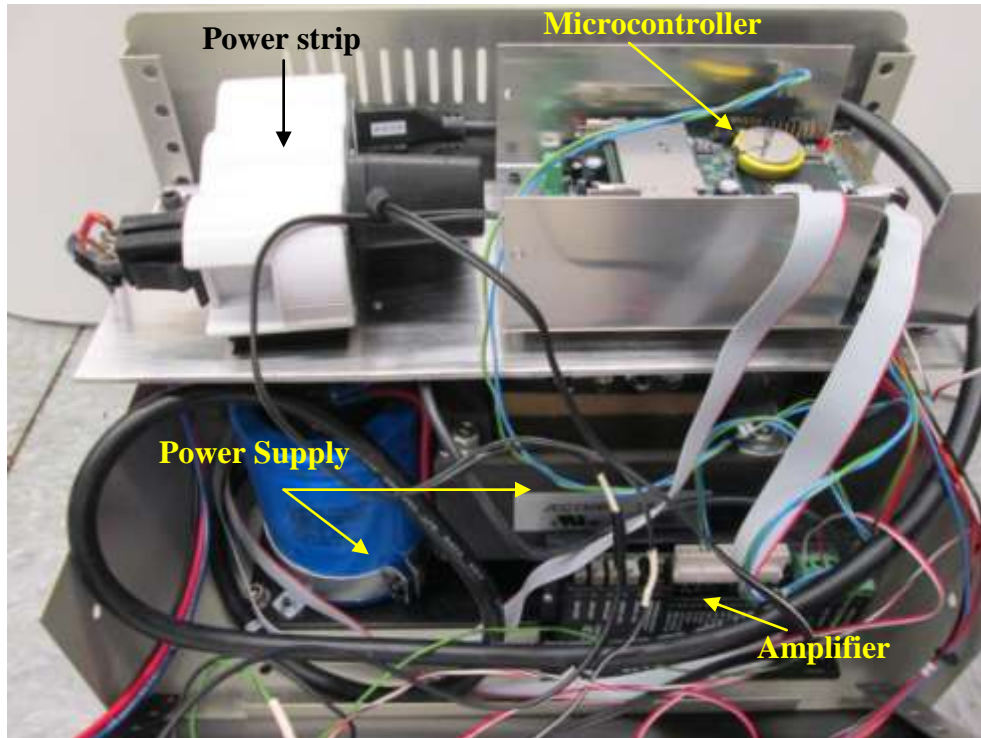


Figure 58. Inside of electrical enclosure.

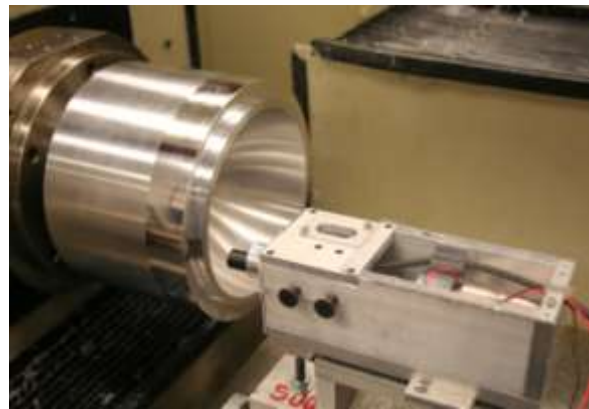
## 4. Thumper II: Operation

Figure 59 shows the Thumper II device set-up in a diamond turning machine whose spindle is holding a hemispherical part (part 2 in Appendix A). Figure 59 shows the Thumper II set-up for alignment on the OC and IC chuck.

Section 4.1 gives details on the measurement task of Thumper II, and Section 4.2 gives details on the tapping task. Section 4.3 details the features of the tap algorithm that determines how hard and when to tap the part. To understand how the human operator sets up the device and operates the GUI, the Thumper II User's Manual should be consulted. A portion of the User's Manual can be seen in Appendix L.



(a) Thumper II set-up for radial alignment on the OC chuck.



(b) Thumper II set-up for axial alignment on the IC chuck.

Figure 59. Thumper II set-up for alignment on each chuck.

## **4.1 Measurement operation & testing**

Many tests have been carried out to ensure that Thumper II measures runout accurately and that its measurement capabilities are optimized. This section details the verification tests performed and provides insight into the measurement limitations with this device.

### **4.1.1 Measurement Overview**

The measurement task of Thumper II operates on a simple but powerful idea. It uses the specified spindle speed value and time functions on the microcontroller to determine where a data point is located in space. This is a powerful idea because Thumper II does not need to reference a datum on the machine nor use information from a spindle encoder. Instead, the microcontroller updates the spindle location throughout the alignment process based on the specified spindle speed. The microcontroller updates a variable for spindle location ( $0^\circ - 360^\circ$ ) based on its clock in an interrupt that executes every 6 milliseconds. The biggest issue with this idea is that the alignment process could fail if the actual spindle speed is not specified correctly or is not constant.

Two measurement methods were tested with Thumper II: Total Indicated Runout (TIR) and Least-Squares Circle (LSC).

- 1) The TIR measurement defines the runout as the difference between the maximum and minimum Thumper II displacements observed over one spindle revolution. To perform TIR measurement with Thumper II, the rail position is observed for an entire revolution. The maximum and minimum position is updated as this observation takes place. The magnitude of the runout is the difference between the maximum and minimum position, and the location of the highspot is the location of the minimum position (i.e. most inward position for Thumper II).
- 2) The LSC measurement is more complex, yet more robust, than the TIR method. In this approach, a finite number of data points are collected and a circle is fit to these points. The center of this circle is the center of the part. Thumper II uses 20 data

points to find the center as this was shown to be an adequate number of points by Furst [2].

If form errors on the part are greater than the misalignment, the TIR method cannot be used to align the part to less than the magnitude of the form errors. Figure 60 illustrates this point and shows a part with an elliptical cross-section which slightly deviates from a nominal 150 mm diameter circle. The part in Figure 60 cannot be aligned to less than 20  $\mu\text{m}$  of runout as defined by the TIR measurement. When there are two high spots as in Figure 60, the TIR measurement will result in an alignment program that cannot decide when to impact the part and cannot converge. However, the part in Figure 60 can be aligned to less than 20  $\mu\text{m}$  of runout using the LSC method. The LSC measurement constructs the shape of the workpiece surface during each measurement and can align the part to less than the form error magnitude. In this way, the LSC method minimizes the deviations of the part from a perfect circle. In a similar manner, a bump or dirt particle could be interpreted in the TIR method as a high spot, but the effect of the particle would be averaged in the LSC measurement. The LSC method is used on both OC and IC chucks due to its superior robustness over the TIR method.

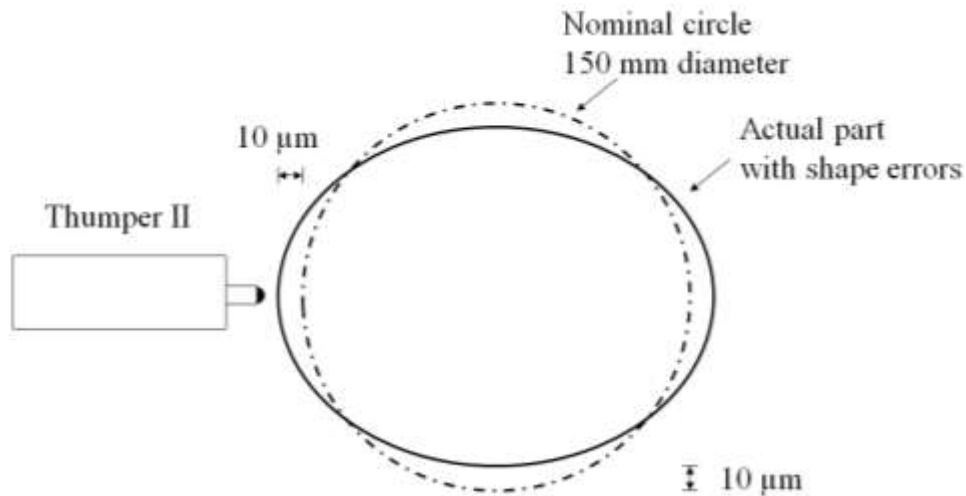


Figure 60. Shape errors and the LSC method.

#### 4.1.2 LSC measurement details

The LSC measurement uses a least-squares circle fit function based on Taubin's circle fitting technique[23]. This technique was coded by Chernov [24] and this code is the basis of the circle fitting algorithm in Thumper II. Figure 61 illustrates how the least-squares circle fit is performed. The inputs for the algorithm are the locations of the points on the "Actual data" curve. The center is found by minimizing the net distance "Minimized distance" between an "Actual data" point and the surface of the best-fit circle in the radial direction. The output of the algorithm is the center location of the fitted circle.

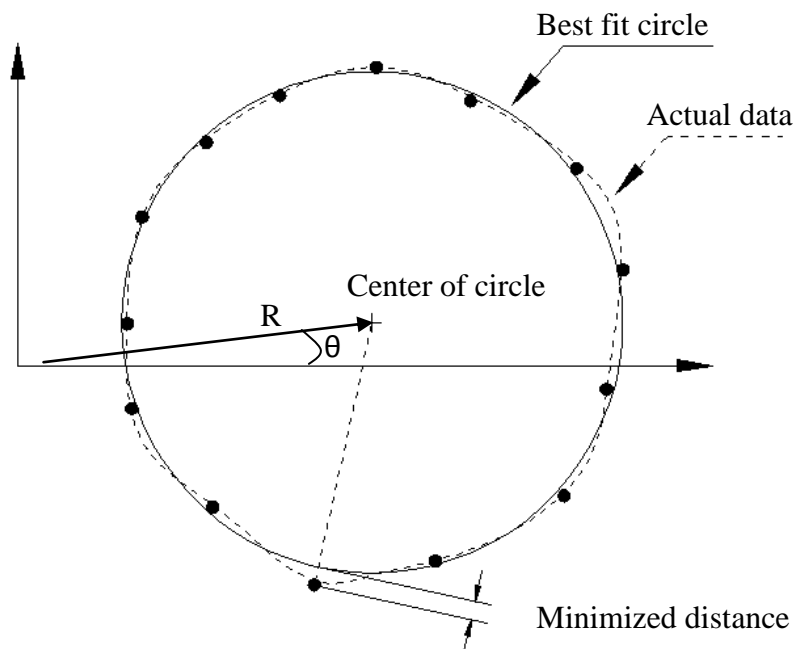


Figure 61. Least-square circle fit method.

#### *LSC data collection for OC Chuck measurement*

The LSC method just described is used for measurements on the OC and IC chuck. However, the geometrical meaning of collected data points differs depending on the chuck of interest.

Figure 62 shows the geometry for runout measurement on the OC chuck if looking down the axis of the spindle in Figure 59. As shown, the part center is offset from the center of rotation and Thumper II is measuring radial runout. The value  $R$  represents the nominal radius of the part (which ranges 76.2 mm to 101.6 mm) and the value  $d$  represents displacement of the Thumper II tip during measurement (which ranges from less than 5  $\mu\text{m}$  to a maximum of 250  $\mu\text{m}$  on the OC chuck). The high spot will be next to the Thumper II tip when the tip is at its minimum (most retracted) point.

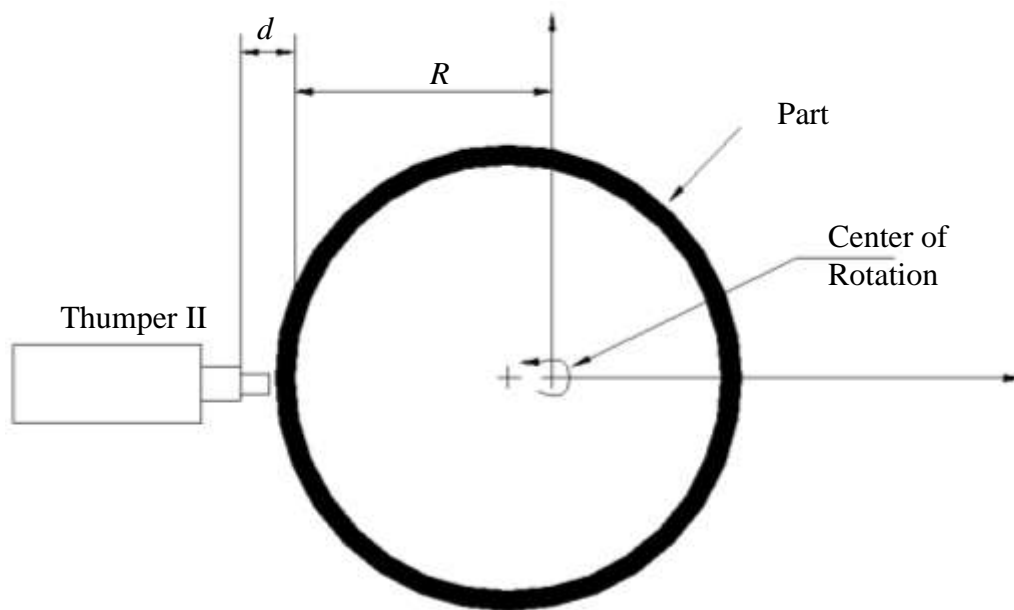


Figure 62. LSC measurement on the OC chuck.

A measured set of data as in Figure 61 is constructed from OC chuck measurements with the following steps:

- 1) The spindle rotates at a constant and known speed.
- 2) As the spindle rotates, the position of the Thumper II is recorded (i.e.  $d$  in Figure 62) along with the current spindle value (which ranges from  $0^\circ$ – $360^\circ$ ) for every  $\sim 18^\circ$  of spindle rotation ( $360^\circ/20$  data points =  $18^\circ$ /data point).

- 3) The “Actual data” circle as in Figure 61 can then be constructed by adding the nominal radius  $R$  to the measured deviation  $d$  for each point yielding a set of points on the curve in polar coordinates  $(R, \theta)$ .
- 4) The data points from step 3 can be sent directly to the circle fit algorithm, which returns the best-fit center of the part in polar coordinates.

*Actual data from OC Chuck measurement*

Figure 63 shows actual scale position data points plotted versus spindle angle (this is step 2 from above). This sine wave shape is expected for measurements in which the runout is orders of magnitude smaller than the part radius. The sine wave shape for scale displacement will be seen for OC and IC chuck measurements. In this particular measurement, the distance between the part and rotational center was calculated to be  $101.9 \mu\text{m}$  and the part center was located at  $81.4^\circ$  according to the best-fit circle algorithm.

As seen in Figure 63, the high spot (i.e. minimum rail position) is observed to be around  $81.4^\circ$ , the value calculated by the LSC function. This ability to see the runout location in Figure 63 is to be expected with shape errors much less than the runout.

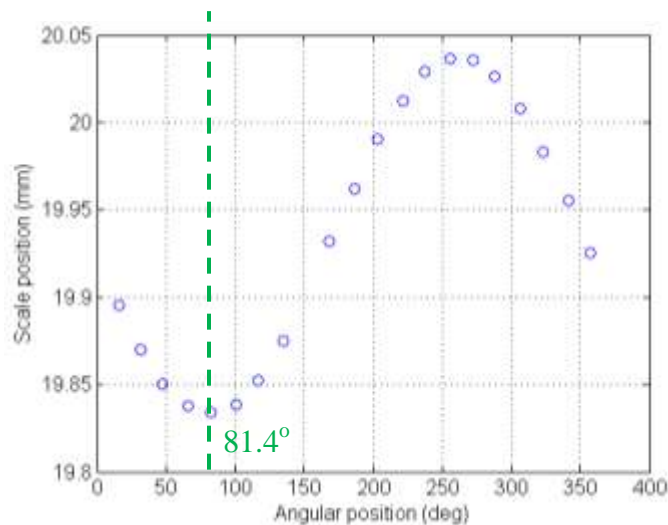


Figure 63. Raw data of rail position during part measurement.

The “Actual data” circle can be constructed by referring to step 3 on page 86, and this circle is shown in Figure 64. Although it cannot be seen due to scaling, the center of the best-fit circle for the points in Figure 64 is at (101.9  $\mu\text{m}$ , 81.4 $^\circ$ ).

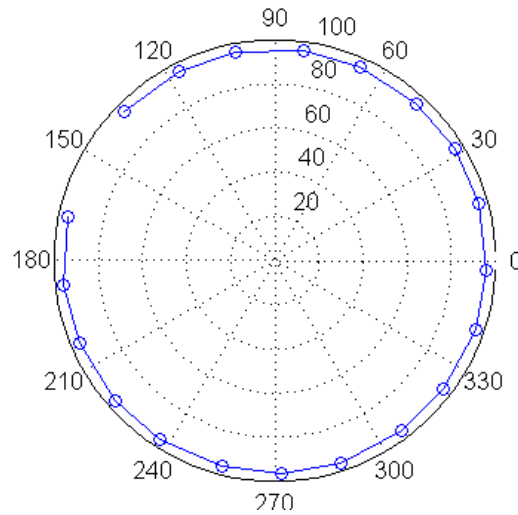


Figure 64. Measured points on part surface.

#### *LSC data collection for IC Chuck measurement*

Figure 65 shows the geometry for runout measurement on the IC chuck if looking at the top of the set-up in Figure 59. As shown, the face of the part is tilted from a plane perpendicular to Thumper II and axial runout is being measured. The value  $R$  represents the nominal radius of the part (which ranges 76.2 mm to 101.6 mm) and the value  $d$  represents displacement of the Thumper II tip during measurement (which ranges from less than 5  $\mu\text{m}$  to a maximum of 2.5 mm on the IC chuck).

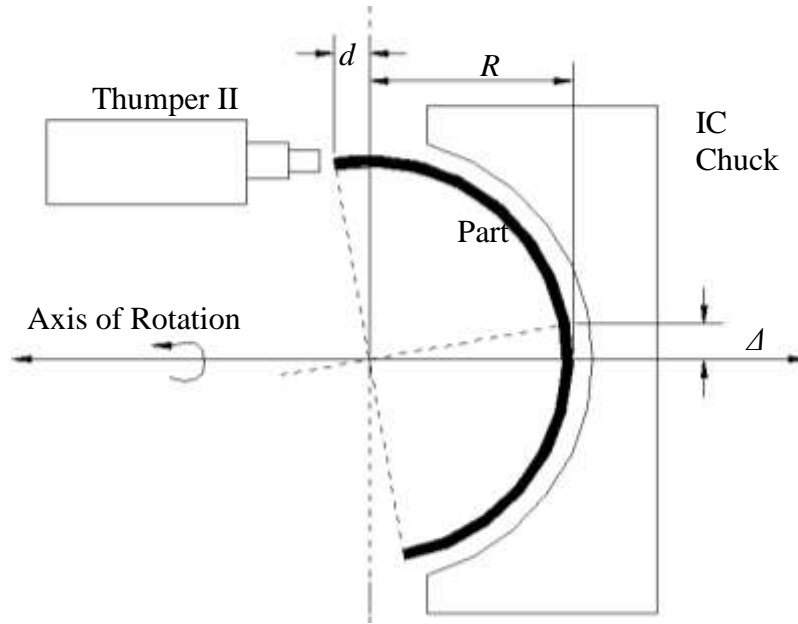


Figure 65. LSC measurement on the IC chuck.

A measured set of data as in Figure 61 is constructed from IC chuck measurements with the same four steps given for the OC chuck. The rail displacement data for the IC chuck will be a sine wave much like the data from the OC chuck in Figure 63. However, there is a difference in geometrical interpretation to create a circle like the one in Figure 64 for the IC chuck. Figure 65 shows that the distance  $d$  measured by the Thumper II tip is the same as the distance  $d$  between the rotational axis and the center of the part surface for a spherical shape part. As a result, just as for the OC chuck, the high spot will be next to the Thumper II tip when the tip is at its minimum (most retracted) point. The  $d$  values can be added to the nominal  $R$  value and a polar plot as in Figure 64 can be constructed as previously described.

#### 4.1.3 Measurement using TIR versus LSC

In Table 10, the LVDT measurement of part runout is compared to the runout measured using Thumper II with Total Indicated Runout (TIR) and Least-Squares Circle (LSC) measurement methods. The LVDT is set-up as in Figure 5 and Thumper II is set-up as in Figure 59 (a), respectively. The LVDT measurement of  $29.5 \mu\text{m}$  was obtained as a TIR

measurement, i.e. simply taking the difference between the maximum and minimum values with the spindle manually rotated. The Thumper II measurements (LSC and TIR) were taken at 8 RPM spindle speed, with the VCA applying a preload force of 2.20 N.

There is about a 4% difference between the average LSC measurement and the LVDT measurement in Table 10. This difference can be partly attributed to different axial location of Thumper II and the LVDT and the part shape at these locations.

Table 10. Misalignment ( $\mu\text{m}$ ) with LVDT and Thumper II (LSC and TIR) at 8 RPM.

Measurement Type	Measurement No.			
	1	2	3	4
Thumper II - LSC	30.76	30.82	30.75	30.77
Thumper II - TIR	31.95	31.95	31.95	31.95
<b>LVDT</b>	<b>29.5</b>			

*TIR measurement at various spindle speeds*

One observation from measurement testing is that the TIR measurement method tends to develop errors at spindle speeds from 8–16 RPM. Table 11 shows the misalignment value from an LVDT and from Thumper II using the LSC and TIR methods for two part locations. In Table 11, as spindle speed is increased, the misalignment value (i.e. distance between part center and rotational center) is nearly constant for the LSC method while the LVDT shows 29.5  $\mu\text{m}$  of misalignment. However, there appears to be a sudden misalignment increase from the 2 to the 4 RPM measurement in the TIR case. Based on these results, the TIR measurement is not as robust or reliable as the LSC measurement.

Table 11. Misalignment ( $\mu\text{m}$ ) at different spindle speeds.

Meas.	Measurement Type	Spindle speeds (RPM)					Std. Dev.
		1	2	4	8	16	
1	Thumper II (LSC)	30.84	30.78	30.89	30.81	30.84	0.04
	Thumper II (TIR)	31.86	31.95	38.35	38.33	38.33	3.52
	LVDT	29.50					-
2	Thumper II (LSC)	466.42	466.97	467.33	465.28	467.43	0.88
	Thumper II (TIR)	473.54	473.55	467.00	468.70	473.40	3.15
	LVDT	Measurement not taken					-

#### 4.1.4 Measurement preload force

Table 12 shows that LSC and TIR measurements with Thumper II show little variation when preload forces are varied the range of 1.65 N to 4.40 N. These measurements were taken at a spindle speed of 16 RPM. Each misalignment value is the average of four runs at the given preload force and measurement type. The preload force used by Thumper II is 2.20 N. The issue of tip wear as a function of part surface speed and load is addressed in Section 4.1.8.

Table 12. Misalignment ( $\mu\text{m}$ ) at different VCA preload forces.

	Preload force (N)			
	1.65	2.20	3.30	4.40
LSC	465.78	468.48	465.50	467.09
TIR	473.11	473.41	470.30	473.28

#### 4.1.5 Repeatability of the LSC measurement

The repeatability of the least-squares circle (LSC) measurement can be determined by measuring the same part with the same runout multiple times. If the LSC measurement is highly repeatable, then the magnitude and location of the highspot will change very little.

The results of this test are given in Table 13. Table 13 shows three sets of runout measurements taken by Thumper II at 8 RPM spindle speed. The part was moved to a different location in between each measurement set. The low percent difference values indicate the high level of repeatability for the LSC runout measurement. This suggests the part need only be measured once to obtain a reliable value for the LSC runout magnitude and location.

It is interesting to note that the measurement set with the highest variability is set 3 which measures just above 3  $\mu\text{m}$  of center misalignment. It is more important for this small misalignment value to be accurate as it is the final test of the part location. Although the 3  $\mu\text{m}$  set is the least repeatable, the variation around 1.0% is still acceptable.

Table 13. Repeatability of the least-squares circle fit measurement.

Measurement Set	Runout Magnitude ( $\mu\text{m}$ )	Runout Location (degree)	Runout %diff from average of 4 runs
1	128.6	117.5	0.55
	129.5	118.0	0.09
	129.6	117.9	0.18
	129.7	117.7	0.27
			Average = 0.27
2	20.6	102.3	0.03
	20.6	102.2	0.03
	20.6	102.2	0.06
	20.6	102.4	0.00
			Average = 0.03
3	3.3	76.6	0.47
	3.4	77.0	1.20
	3.4	76.8	0.97
	3.3	76.5	1.69
			Average = 1.08

#### **4.1.6 Effect of incorrect spindle speed from operator**

Inaccurate spindle rotation can make it difficult or impossible for Thumper II to function as designed due to at least three complications:

- 1) Thumper II could tap the part in the wrong location, thus not moving the part in the desired direction.
- 2) Invalid part center locations could result in the alignment algorithm not working properly as displacements corresponding to a given impact velocity are invalid.
- 3) The invalid part surface data points could suggest that the part misalignment target has been met when in fact the part is not aligned.

This spindle speed error refers to how close the actual average spindle speed is to the operator specified value used in the Thumper II program code. The effect of spindle speed can be evaluated using two consecutive runout measurements at an operator specified speed of 4.0 RPM but actual speed of 4.2 RPM. At the actual spindle speed the spindle rotates  $378^\circ$  in 15 seconds (i.e. one measurement cycle), even though the microcontroller assumes the spindle has rotated  $360^\circ$  in 15 seconds. Thus, it is expected that the high spot in the second measurement would be  $18^\circ$  away from the first measurement.

To show the effect of spindle speed, data in Table 14 was collected for four consecutive measurements using the LSC method. For this test, the program code spends 15 seconds collecting data for the first measurement, and after the least-squares algorithm is executed, the code spends 15 more seconds for the second measurement. In the first data set the assumed and actual spindle speeds are 4.0 RPM and in the second set the actual speed is 4.2 RPM. Table 14 shows the misalignment magnitude and location for each measurement. Table 14 shows that the expected  $18^\circ$  shift in misalignment location is closely matched by the observed average  $18.91^\circ$  shift.

Table 14. Measurement of the effects of incorrect spindle speed.

Meas.	Assumed: 4.0 RPM Actual: 4.0 RPM			Assumed: 4.0 RPM Actual: 4.2 RPM		
	Misalign. ( $\mu\text{m}$ )	Location (deg)	$\Delta$ Location (deg)	Misalign. ( $\mu\text{m}$ )	Location (deg)	$\Delta$ Location (deg)
1	50.49	312.20	-	49.19	207.49	-
2	50.42	312.30	0.10	48.42	186.80	-20.69
3	50.48	312.20	-0.10	49.32	169.40	-17.4
4	50.47	312.20	0.00	50.03	150.76	-18.64
Avg.	50.47	-	0.00	49.24	-	-18.91

A final note about spindle speed operator input error is that these errors are relative to the assumed speed. In other words, the same shift in misalignment location observed for assumed and actual speeds of 2.0 and 2.1 RPM is expected for assumed and actual speeds of 8.0 and 8.4 RPM. This fact makes it possible to understand how close the actual spindle speed should be to the specified.

More testing would have to be done to determine the amount of spindle input error that would result in the alignment process not working due to the three complications listed at the beginning of this section. There is a 2.4% difference in Table 14 between the misalignment values at the correct spindle speeds when compared to those at the correct speed, so even this difference in spindle speed (4.0 and 4.2 RPM) could result in Thumper II incorrectly believing that the part is aligned.

#### 4.1.7 Tip settling time

When the tip first contacts the workpiece at the beginning of a measurement cycle, the tip will rebound slightly, and it will take a finite amount of time to rest against the part. To ensure that the measurement points of the workpiece are valid, the tip must be in contact with the workpiece before measurement begins.

This settling time was investigated with the experimental set-up in Figure 13. Figure 66 shows the rail position over a 500 ms time span for two forces applied with the VCA; 2.20 N and 4.40 N. After 20 mm of displacement, the tip contacts a stationary block and settles quickly. Even with the 4.40 N load, the tip settles in about 25 ms after contacting the block.

The measurement preload force used in Thumper II is 2.20 N. After the force is first applied, the device waits 2 seconds before beginning to take measurements. As indicated in Figure 66, 2 seconds as an ample amount of time for the tip to contact the part and settle.

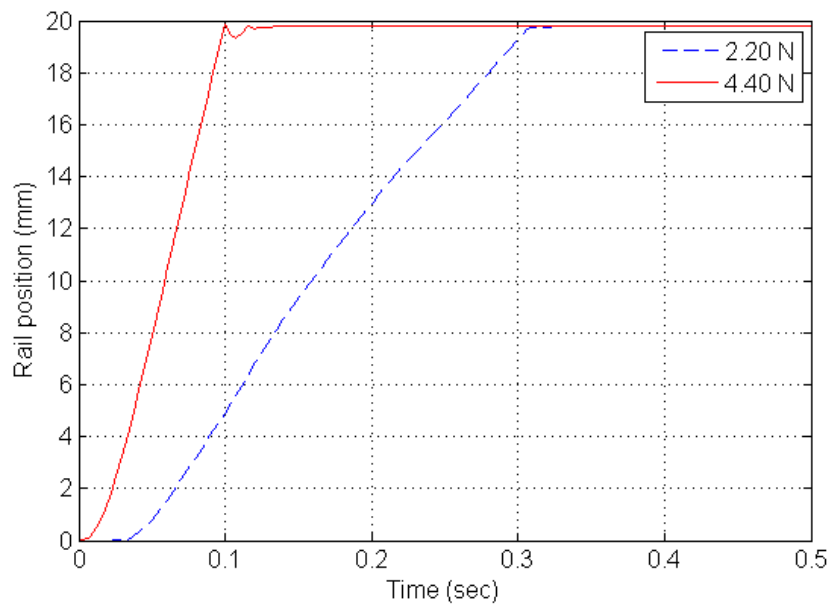


Figure 66. Tip settling time with measurement type forces.

#### 4.1.8 Wear of Thumper II tip

Since the tip of Thumper II is part of the metrology scale being used to measure the workpiece, it is important to consider how the tip wears during measurement. To ensure accurate part measurement, the tip should wear much less than the misalignment goal of 2.5  $\mu\text{m}$  during a single measurement.

Equation (36) shows Archard's wear equation. Equation (36) states that the volumetric wear  $V_w$  ( $m^3$ ) is proportional to the wear rate  $k_w$  ( $m^2/N$ ) and the product of the normal force  $F_n$  and sliding distance  $d_s$ .

$$V_w = k_w F_n d_s \quad (36)$$

Figure 67 shows the experimental set-up used to investigate tip wear during a measurement. It shows a tip from Thumper II being held against a part via a spring force, and the force being directed with the aid of a linear bearing. The tip is contacting a flat surface, making it analogous to the set-up for an IC chuck measurement. The spring in Figure 67 supplies a normal force  $F_n$  between a plastic tip and the part. The force was determined by multiplying the spring rate by the deflection of the spring. The spring rate was measured over the stroke by placing known masses on top of the spring and measuring deflection. The spring rate was shown to be linear. No change in spring rate was measured during the experiments.

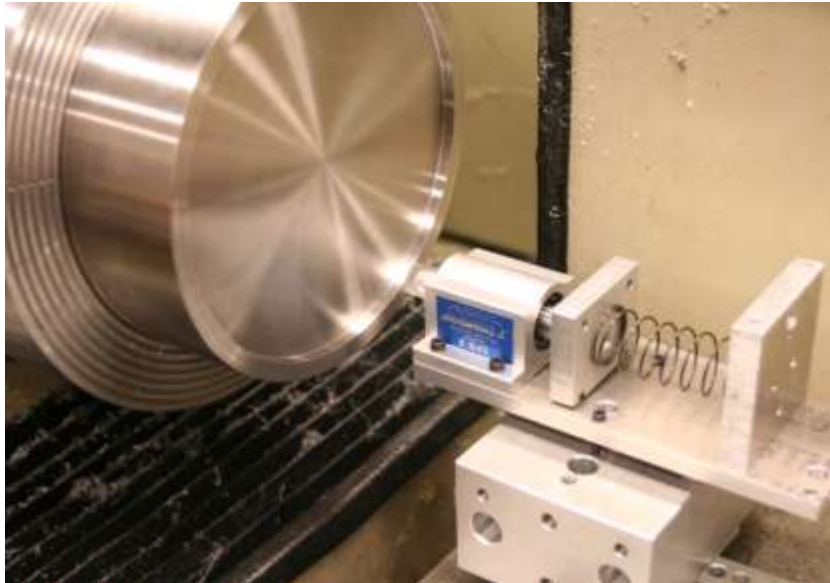


Figure 67. Set-up for tip wear experiment.

The experimental procedure involves rotating the part at a known speed and allowing the spring to apply the normal force for a specific amount of time. The sliding distance  $d_s$  is easily calculated by knowing the circumference of the part and the number of spindle revolutions. Figure 68 shows the profilometer trace over the center of a worn spherical tip. The plastic tip is pushed against a nominally flat surface so it will flatten the end of the spherical tip.

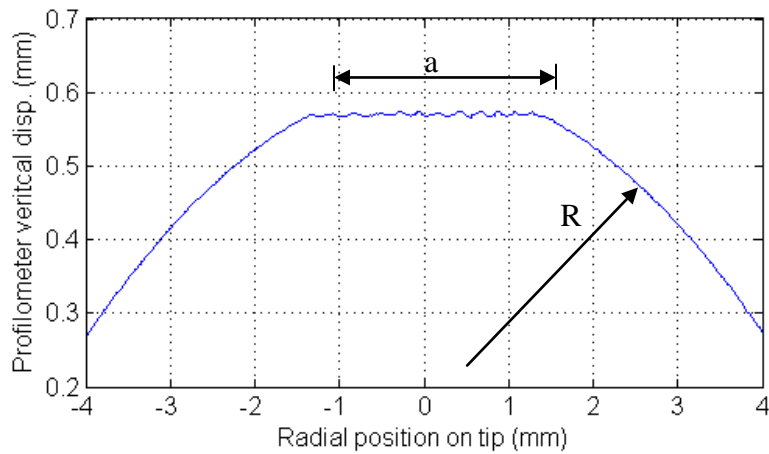


Figure 68. Profilometer trace over worn Acrylic tip.

Since the spherical tip is worn to a flat (Figure 68), it is possible to use Equations (37) to determine the volume of removed material  $V_w$ . The variable  $a$  refers to the radius of the worn flat area, and the variable  $R$  refers to the radius of the base sphere (i.e. radius of the tip) as defined in Figure 69. The tip radius is known as it was diamond turned to a precise radius of 25 mm. The radius  $a$  however must be measured.

$$V_w = \frac{1}{6}\pi h(3a^2 + h^2) \quad (37)$$

$$(R - h)^2 + a^2 = R^2$$

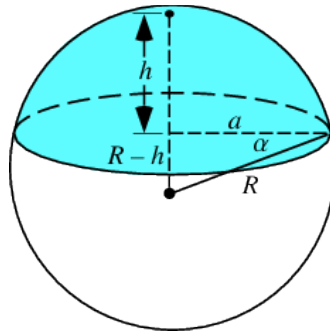
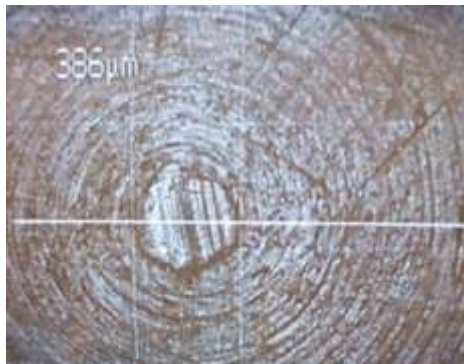
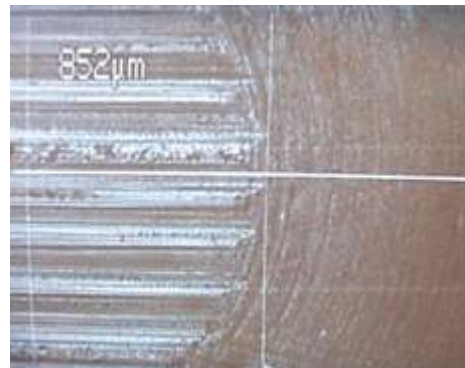


Figure 69. Geometry of spherical cap [25].

The radius  $a$  is found using a microscope as the profilometer trace would only give the correct value if the trace were to go through the center of the worn area. Figure 70 shows images of worn tips taken from a microscope. The worn area is clearly visible, and the direction of sliding can even be seen.



(a)



(b)

Figure 70. Microscope image of wear areas for (a) Nylon and (b) Acrylic tip.

Table 15 shows the key results from the wear experiments where different combinations of surface speed, sliding distance, normal force, and tip material were studied. A new tip was used for each condition. The acrylic tip has an observed wear rate of 100 – 1,000 times

greater than the nylon tip. Thus, nylon is selected for the Thumper II tip material due to its superior wear characteristics. The values for nylon in Table 15 are much smaller than published wear rates of nylon on steel:  $1.8\text{E-}8 \text{ mm}^2/\text{N}$  [26] and  $1.0\text{E-}8 \text{ mm}^2/\text{N}$  [27].

Table 15. Results from tip wear experiment

Material	RPM	# Rev	Normal Force (N)	Slide dist. (m)	Volume ( $10^{-5} \text{ mm}^3$ )	$k_w$ ( $10^{-8} \text{ mm}^2/\text{N}$ )
Acrylic	100	2,000	3.1	914	3,490	1.220
	100	1,000	3.2	457	1,510	1.050
	70	1,400	3.4	640	1,320	0.611
Nylon	100	1,100	3.3	503	13.8	0.0083
	100	2,000	2.4	914	4.1	0.0089
	70	1,750	3.3	800	88	0.0337

The results in Table 15 show that the wear of the thumper tip will have a negligible effect on Thumper II measurements. This conclusion is based on the amount of axial tip wear seen during the first 15 measurements with a new tip. Equations (36) and (37) can be used with the empirical wear rate for nylon to determine how much the tip wears during a single measurement cycle. The wear volume for a nylon tip with a 2.20 N normal load and sliding distance of 9.6 m is given in Equation (38). The sliding distance of 9.6 m is the sliding distance experienced for an 8" diameter workpiece during 15 measurement cycles.

$$V_w = \left( 0.0089 \times 10^{-8} \frac{\text{mm}^2}{\text{N}} \right) (2.20 \text{ N})(9.6 \text{ m}) = 1.88 \times 10^{-6} \text{ mm}^3 \quad (38)$$

Equations (37) can be solved for the height  $h$  of the worn volume as described by Figure 69 as a function of the wear volume  $V_w$  and base radius  $R$ . This relation is given in Equation (39).

$$V_w = \frac{1}{3} \pi h^2 (3R - h) = \frac{1}{3} \pi h^2 (3 * 25 \text{ mm} - h) \quad (39)$$

The height  $h$  that is worn during the first 15 measurements is  $13.3 \mu\text{m}$  as seen in Equation (40). The wear height of  $13.3 \mu\text{m}$ , compared to the smallest desirable measurable runout of  $2.5 \mu\text{m}$ , may seem a large enough number to cause issue with part measurement. However, it must be realized that this value for  $h_w$  is the value for a new tip. Due to the geometry in Figure 69, the  $h_w$  dimension will wear rapidly for a new tip.

The first 1,500 measurements, as compared to the first 15 measurements, show only a  $0.20 \mu\text{m}$  difference in the  $h_w$  dimension as compared. The wear height of  $13.5 \mu\text{m}$  in 1,500 measurements is an average of about 9 nanometer/measurement of wear in the  $h$  direction. This value of 9 nm is much smaller than the misalignment target of  $2.5 \mu\text{m}$  and thus it is concluded that tip wear for nylon is negligible to part measurement.

$$\begin{aligned} h_w &= 13.3 \mu\text{m} \text{ (first 15 measurements)} \\ h_w &= 13.5 \mu\text{m} \text{ (first 1,500 measurements)} \end{aligned} \tag{40}$$

## 4.2 Tap dynamics and coil motion

Equations (41) and (42) can be used to completely model the motion of the coil assembly during a tap. Equation (41) states that the applied voltage  $V_{app}$  across the coil is equal to the sum of a resistive voltage drop  $V_R$ , back electromotive force (i.e. back EMF) voltage  $V_B$ , and inductive voltage  $V_L$ . Equation (41) follows from the circuit diagram in Figure 71.

$$\begin{aligned} V_{app} &= V_R + V_B + V_L = iR + vK_B + L \frac{di}{dt} \\ V_{app} &= i * 9.2\Omega + v * 8.79 \frac{Vs}{m} + 0.0042H * \frac{di}{dt} \end{aligned} \tag{41}$$

The variables  $R$ ,  $K_B$ , and  $L$  in Equation (41) are the motor's data sheet values for resistance, back EMF constant, and inductance. The variable  $i$  is the current through the coil.

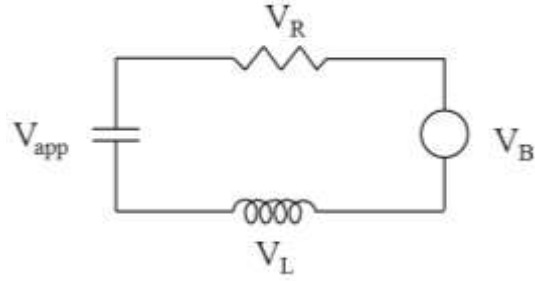


Figure 71. Electrical circuit for linear voice coil motor.

Equation (42) is the second equation used to describe coil assembly motion. It shows that the velocity of the coil  $v$  is a function of the acceleration  $a$  and the amount of time  $t$  the coil is accelerated. The acceleration is further defined as the ratio between the applied force and coil assembly mass  $m$ . Equation (42) relates the velocity of the coil to the moving mass, Lorentz force produced by the motor  $iK_F$ , and the resistive friction force  $F_f$  in the linear bearing.

$$v = at = \frac{iK_F - F_f}{m} t = \frac{i * 8.81 \frac{N}{A} - 1.40N}{m} t \quad (42)$$

The amplifier is used in Voltage mode and Equations (41) and (42) show why voltage mode lends itself to velocity control applications. If a voltage  $V_{app}$  is applied across the coil, a current will be induced due to Equation (41). This current produces a Lorentz force that accelerates the coil if the force is greater than the bearing friction. A velocity of the coil creates a back EMF voltage in Equation (41), and since  $V_{app}$  is constant in voltage mode, the current is reduced. Eventually the current is reduced to equal the bearing friction force, thus coil acceleration becomes zero and a terminal velocity is reached.

#### 4.2.1 Understanding coil dynamics in voltage mode

With the amplifier in voltage mode, the control parameters are the duration and magnitude of the voltage applied across the coil. Figure 72 shows a profile of voltage measured across the VCA lead wires as it is accelerated prior to a tap. To tap the part, the coil is fully-retracted

into the magnet, and a two-step voltage signal as seen in Figure 72 is applied to the coil. The 2-step voltage signal seen in Figure 72 is used for two reasons. First, there is not enough actuator stroke for a 0.50 m/s or greater impact velocity to be attained before the coil reaches the end of travel by simply applying a single voltage. Instead, the coil must be accelerated more rapidly so that the desired impact velocity can be attained in a shorter distance. Secondly, the low-step voltage could be eliminated and only the high-step voltage could be applied. However, this would require positioning the tip at a precise distance from the part such that the impact occurs just after the high-step voltage is finished.

To vary the impact velocity, there are three variables that are altered by Thumper II: high-step voltage value, low-step voltage value, and duration of the low-step voltage. To make the tap process consistent, the duration of the high-step voltage is the same for all tap magnitudes in Thumper II at 20 milliseconds. Careful selection of parameter values can yield precise repeatable impacts essential to automating part alignment.

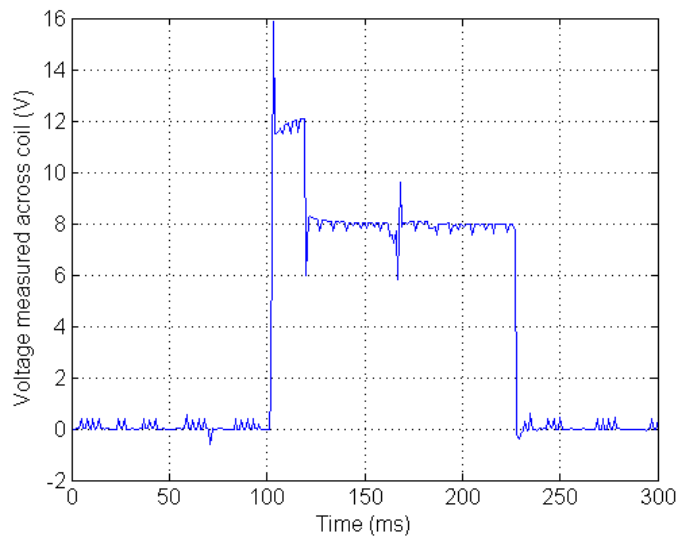


Figure 72. Voltage across coil with amplifier in voltage mode.

Simulations using Equations (41) and (42) can predict the terminal velocity given an input voltage profile. Figure 73 shows how the VCA current and coil velocity changes as the voltage command in Figure 72 is applied in the simulation. Figure 73 shows that the coil velocity reaches a nearly steady-state velocity of around 0.70 m/s after the high-step voltage is applied for 20 milliseconds.

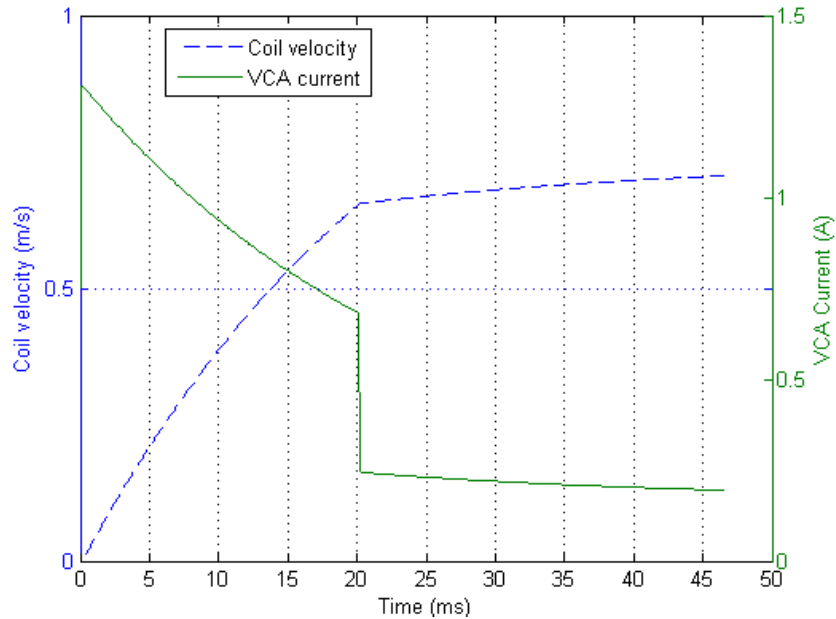


Figure 73. Simulated coil velocity and current at 12V high-step and 8V low-step.

Experimental data was collected and compared with the model in Figure 73. The position of the rail is recorded using the Thumper II encoder. Rail position is then differentiated to find velocity. The current is measured by using the 0-5V analog output signal on the amplifier that represents the supplied current. The current and position measurements are not synchronized in time since they are collected with different instruments. However, assuming the position and current begin to change when the voltage is initiated can provide a starting point for each.

The coil velocity rises in the first 20 ms and reaches a value just under 0.50 m/s. This is a significant difference between the 0.70 m/s final velocity in the simulated version of Figure 77. This could be due to the unknown behavior of the bearing friction at these velocities. The actual friction during a tap at 0.50 m/s could be greater than the static bearing resistance force of 1.40 N depending upon the nature of the ball bearing. Section 4.2.3 details how this empirical knowledge of coil dynamics is used to create a tapping scheme with Thumper II.

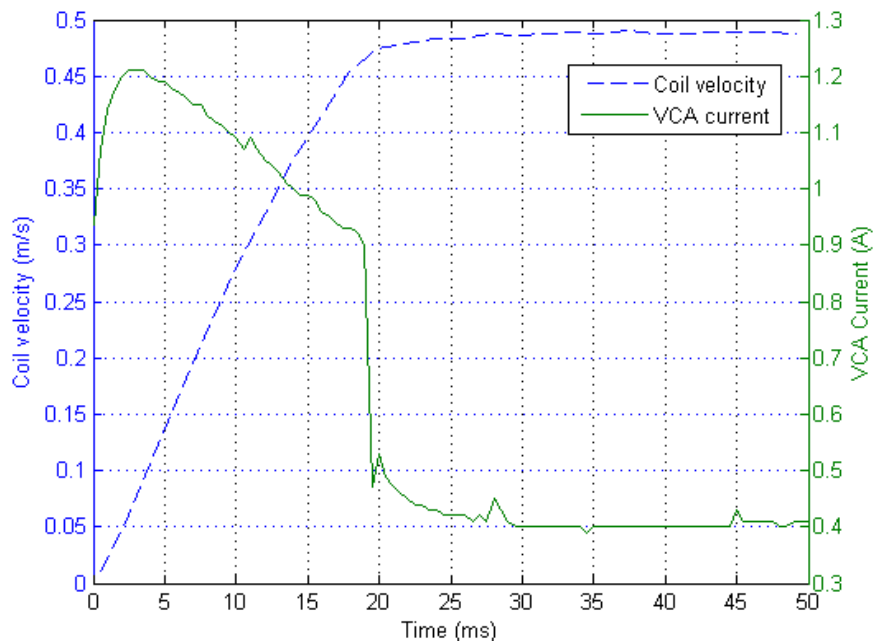


Figure 74. Measured coil velocity and current at 12V high-step and 8V low-step.

#### 4.2.2 Effect of bellows during tap

##### *Resistance force from bellows*

When Thumper II becomes fully extended, the bellows is positioned such that no force is applied to the moving mass. Table 16 shows the effect of the bellows during a tap. This test consisted of impacting a load cell (as in Figure 13) at a given impact velocity and noting the peak impact force. The peak force values in Table 16 are the average of three runs at the

given impact velocity. As seen in the table, the peak impact forces are less when the bellows is installed.

Table 16. Effect of bellows during tap.

Impact velocity (m/s)	Peak force (N)	
	Without bellows	With bellows
0.25	162.7	151.5
0.50	352.5	346.5
1.00	699.1	671.1

Figure 75 shows an average of a 3.5% decrease between the slopes of the best fit lines with the bellows installed compared to the bellows removed. This does not have a significant effect on the operation of Thumper II.

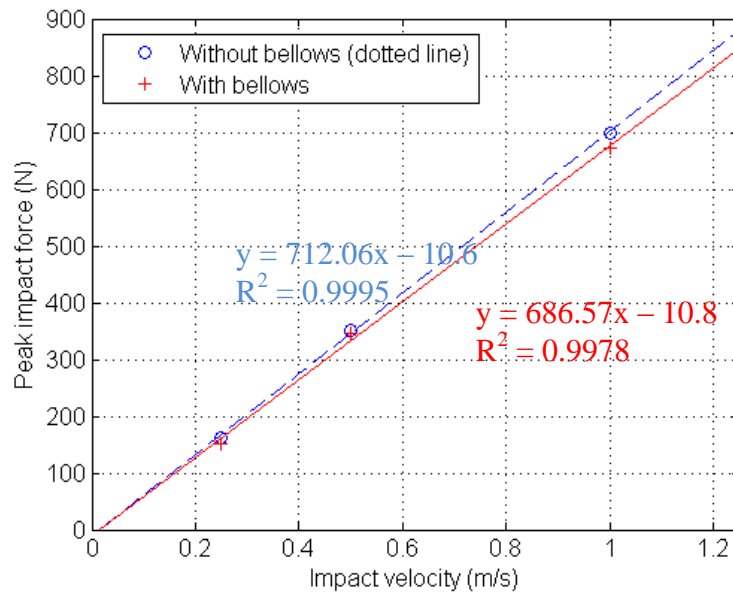


Figure 75. Impact force with bellows and without bellows installed.

### *Effect of vacuum created during tap*

When a tap occurs, the volume inside the bellows rapidly expands. Since Thumper II is nominally a closed volume (though it certainly has small voids at joints), it is expected that this rapid volume expansion will create a small vacuum inside the structure. If the vacuum is created, it will result in a resistive force on the coil-rail-tip assembly. Since the bellows is installed such that no visible force pulls the coil assembly inwards at full-extension, the creation of a vacuum could be the source of the 3.5% decrease in peak impact force seen in Table 16.

Table 17 shows experimental results that suggests the existence of this vacuum and also quantify its effect. In this test, Thumper II tapped a load cell at a given impact velocity and the peak force was recorded. For some tests the small plastic shield above the encoder readhead (see Figure 13) was removed while in others it was bolted in place. It is expected that the vacuum effect would be greater if this shield were bolted in place. The peak force values seen in Table 17 are the average from three individual taps at the specified impact velocity.

Table 17 shows that the peak impact forces are less when the shield is installed. This suggests that a small vacuum is created during a tap.

Table 17. Effect of vacuum created in bellows during tap.

Impact Velocity (m/s)	Peak force (N)	
	Shield Off	Shield On
0.30	203.4	190.7
0.65	442.5	434.3
0.90	618.2	599.3
1.10	759.6	744.8

There is an average percent difference of 0.9% between the slopes of the best fit lines with the shield installed compared to the shield removed. The percent difference of 0.9% suggests that the vacuum effect contributes partly to the difference of 3.5% seen in Table 16. The decrease in the tap magnitude with the bellows installed as compared to the bellows removed can be contributed to the vacuum as well as the pullback force that the bellows exerts on the coil assembly.

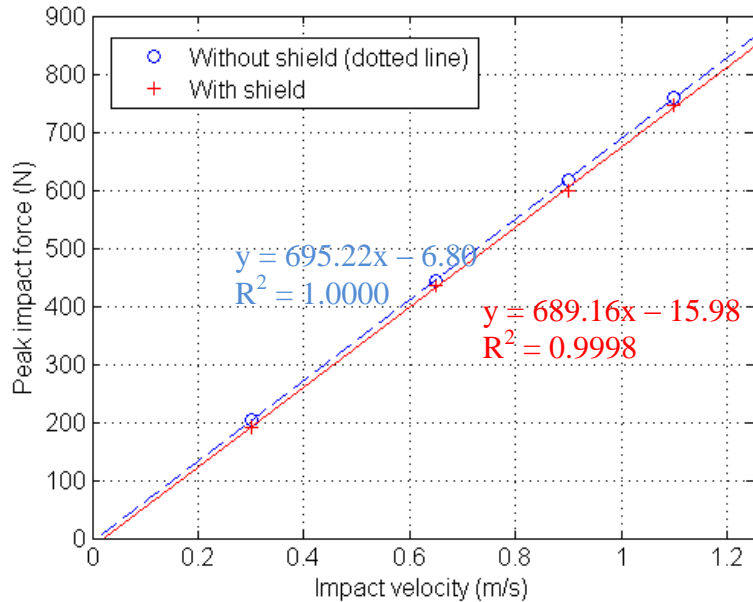


Figure 76. Impact force with shield and without shield installed.

### 4.2.3 Tapping scheme with Thumper II

The applied voltage signal in Figure 72 results in the impacting mass motion in Figure 77. It shows the position and velocity of the coil assembly during the acceleration phase of a tap. The velocity of the mass linearly increases during the 20 ms that the high-step voltage is applied. The 8V low voltage step offsets the back EMF and keeps the coil at 0.50 m/s until it impacts an end stop resulting in a sharp drop in velocity. The position of the coil increases parabolically for the first 20 ms and linearly in the constant velocity region.

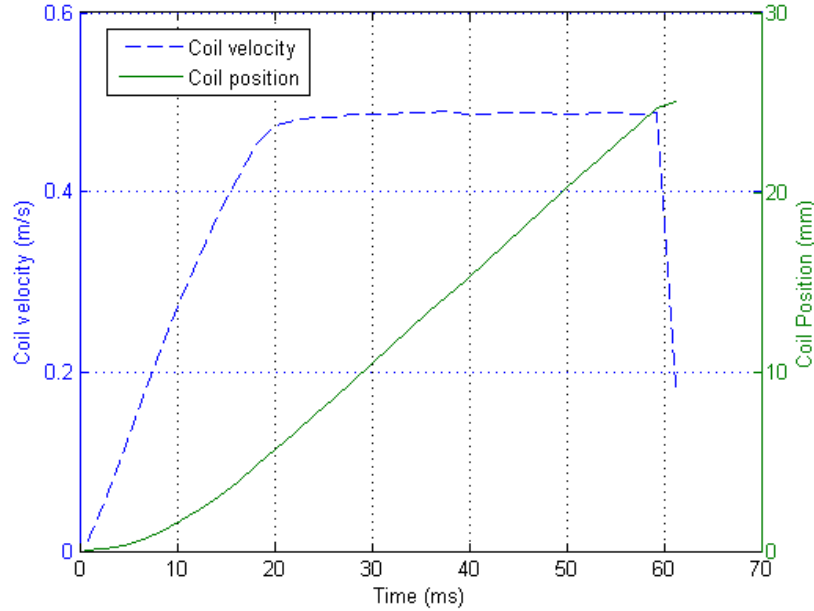


Figure 77. Measured position and velocity of coil-rail-tip in voltage mode.

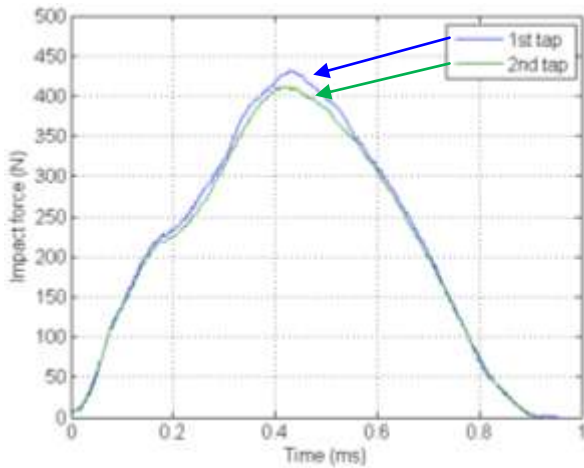
Thumper II uses empirical data to achieve a given impact velocity. The four values are: 1) the high-step voltage value, 2) low-step voltage value, 3) duration of the low-step voltage until impact for 20 mm stroke, 4) and the peak impact force. Thumper II impacts the workpiece over a speed range from 0.15 – 1.25 m/s in steps of 0.05 m/s as seen in Appendix C. Also, 0 shows that the voltage magnitudes for the high-step and low-step increase linearly with impact velocity. Thus, to determine the high-step and low-step voltages for a desired impact velocity, this linear relationship can be exploited and the predicted velocities values can be verified with testing.

#### 4.2.4 Tapping frequency – repeatable impacts

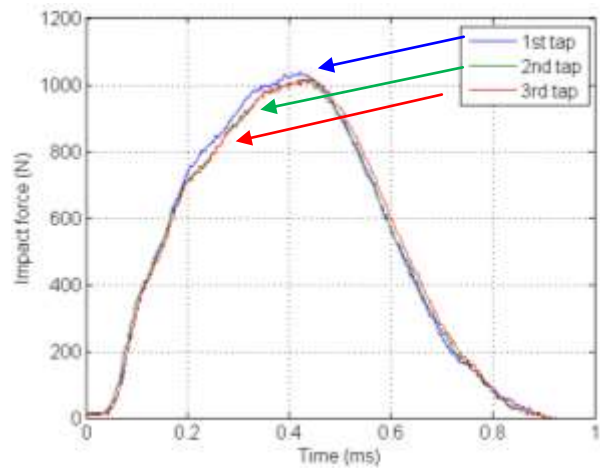
Thumper II is able to tap the part near the high spot up to 3 times in one revolution. Tapping multiple times per revolution allows Thumper II to align parts more quickly. If it is observed that the maximum impact velocity of 1.25 m/s yields a part displacement less than the new misalignment value, it may be useful to tap the part multiple times during one revolution at

1.25 m/s. It should be noted that 3 taps per revolution could be increased if desired, but it was determined that higher frequencies were not needed.

Figure 78 (a) shows force profiles for two 0.50 m/s impacts that occurred during 1 revolution and Figure 78 (b) shows three 1.25 m/s impacts. For any impact velocity, the consecutive impacts are spaced about 250 ms apart. Thus, three impacts occur in span of about 500 ms. Since the taps are spaced 250 ms apart, they are not visible on the time scale as recorded. Therefore, the force profiles have been shifted so that they line up and can be compared. As seen in Figure 78, tapping multiples times per revolution yields nearly identical impacts for a given impact velocity. The second and third impacts in Figure 78 (b) are so similar that they are hard to differentiate on the plot.



Force profiles for two impacts during 1 revolution for 0.50 m/s impacts



Force profiles for three impacts during 1 revolution for 1.25 m/s impacts

Figure 78. Multiple impacts per revolution.

### 4.3 The adaptive tap algorithm

The adaptive tap algorithm determines how hard, when, and how many times to impact the part during a given measurement cycle. This algorithm is executed after each measurement

before the part is tapped. Sections 4.3.1 and 4.3.2 explain the individual features of the adaptive tap algorithm for determining how hard and when to tap the part. Section 4.3.3 explains in detail how all of the features of the algorithm work together to reduce centering error.

#### **4.3.1 Algorithm features: How hard to tap the part**

The alignment algorithm has three ways that it determines how hard to tap the part. The first is to choose a velocity based on user inputs and a model-based prediction. This method is used for the first tap only. The second way is to choose from previously used tap velocities and observed part displacements. The third way is to use linear regression with impact velocity squared ( $v_{t1}^2$ ) and part displacement ( $\delta$ ) to determine the next velocity that should be used.

##### *1. Model-based prediction*

This feature of the alignment algorithm is used for the first tap. To choose a velocity, the program uses part weight and the initial measured runout to estimate an appropriate impact velocity. The estimate is based on theoretical and empirical relations between part displacement and part weight.

##### *2. TDVKA Table – Recording/Using previously used tap velocities and average displacements*

The most reliable method for choosing an impact velocity is to choose from taps that already occurred during the alignment process. To achieve this, data is saved on each tap and updated in a table titled the TDVKA table on the microcontroller. TDVKA represents: tap number (T), part displacement (D), impact velocity (V), impact velocity squared (K), and drop angle (A). Table 18 shows observed values for displacement and drop angle are recorded in the

TDVKA table for each impact velocity. This table was created during an alignment of part 1B on the OC chuck at 11.1 psi vacuum pressure.

The TDVKA table is created in the microcontroller code in the following way. The table is empty at the start of each alignment process. After the first tap cycle, the new part center location is measured and the part displacement magnitude is found. Then, the first row of the TDVKA table is filled. For the first tap, the T column equals the number of taps in the first tap cycle and the D column equals the part displacement. If tapped more than once in the first cycle, the average part displacement is the measured displacement divided by the number of taps. The V column is set equal to the impact velocity used. The drop angle is also calculated and entered into the TDVKA table.

Table 18. TDVKA table from an actual alignment process.

T	D	V	K	A
Number of Taps	Displacement (μm)	Velocity (m/s)	Velocity-square (m <sup>2</sup> /s <sup>2</sup> )	Drop angle (deg)
1	32.65	1.10	1.210	21
2	51.47	1.25	1.563	22
1	30.52	1.05	1.103	24
1	21.38	0.95	0.903	32
1	20.69	0.90	0.810	15
1	14.00	0.80	0.640	20
1	8.40	0.70	0.490	25
1	6.85	0.65	0.423	21
1	5.18	0.60	0.360	26

Subsequent taps are added to the TDVKA table as follows. First, the average part displacement is measured for the most recent tap cycle is calculated. If the velocity for this tap cycle has not been used, it is added to a new row with the method described for the first tap. If the velocity for this tap cycle has been used, then its displacement is averaged with the displacement value already in the table. The TDVKA table is updated after every tap until the

part is aligned. This table is extremely useful as it provides a direct and observed link between impact velocity and part displacement.

### 3. Linear regression of impact velocity and part displacement data

Linear regression is used to predict what impact velocity will yield a desired part displacement. In general, this linear fit is not as reliable as using a velocity directly from the TDVKA table. However, if the displacements recorded in the TDVKA table cannot be used to displace the part towards the center efficiently, it will be necessary to choose a new velocity with which to impact the part.

To perform the linear regression, observed data is fit to Equation (43) where  $m$  is the slope of the best fit line and  $b$  is the  $y$  axis intercept. In this case, the  $y$  data is the part displacement and the  $x$  data is the square of the velocity of the Thumper II mass at impact. Although Equations (52) and (53) suggest the  $y$  intercept should equal zero in Equation (43), it must be realized that Equations (52) and (53) are only valid once static friction is exceeded. Thus, the  $y$  intercept is non-zero and testing showed that assuming an intercept of zero yields an erroneous regression.

$$y = mx + b \quad (43)$$

A simple technique for linear regression is outlined by [28]. To perform the linear regression, the five parameters seen in Equation (44) must first be calculated. The  $x_i$  term indicates a data point in the velocity-squared data set, and the  $y_i$  term indicates a data point in the part displacement data set.

$$S_x = \sum x_i \quad S_y = \sum y_i \quad S_{xx} = \sum x_i^2 \quad S_{yy} = \sum y_i^2 \quad S_{xy} = \sum x_i y_i \quad (44)$$

Then,  $m$  and  $b$  are given by Equation (45) as a function of the terms in Equation (44).

$$m = \frac{nS_{xy} - S_x S_y}{nS_{xx} - S_x^2} \quad b = \frac{1}{n} S_y - m \frac{1}{n} S_x \quad (45)$$

With  $m$  and  $b$  of the best fit line, the Thumper II alignment algorithm can calculate a required impact velocity for a desired part displacement.

Figure 79 shows data collect during four alignment processes of part 1B (see 0) on the OC chuck at 11.3 psi vacuum, where different shapes represent different alignment processes. The values for part displacement were taken directly from the TDVKA table after the process was complete. The curve fit to the data in Figure 79 with a regression value of 0.981 shows how well the linear assumption fits the data. Appendix D shows that the linear relation also holds for other parts, as well as for the IC chuck.

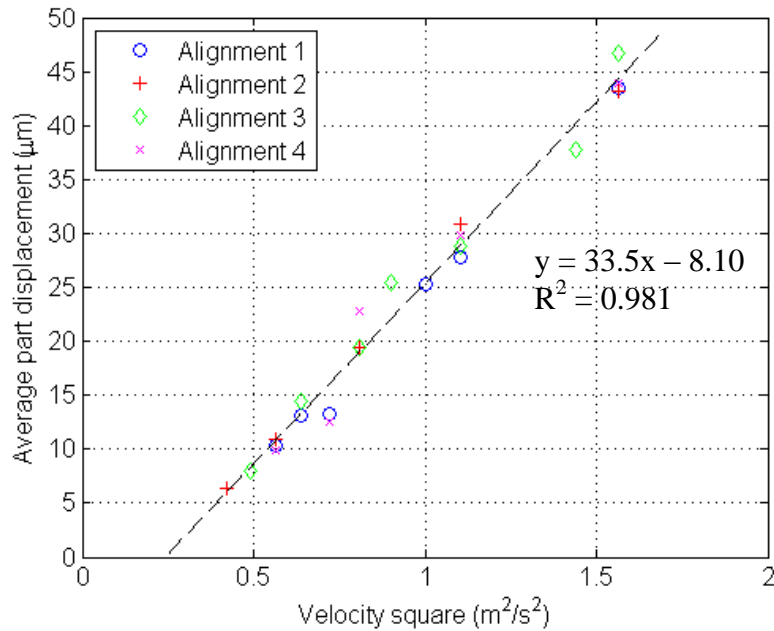


Figure 79. Observed linear displacement-velocity squared relationship.

*Other notes*

Despite the variations due to direction reversal hysteresis seen in Figure 29 – Figure 31, the alignment algorithm does not take into account reversal effects. The alignment algorithm could take the hysteresis effects into account by tapping the part with a different magnitude if the part center goes through the center of rotation. However, the alignment algorithm showed no problem converging without reversal consideration. This could be partly due to the fact

that the 2D displacement experienced by the part on a vertical chuck from a horizontal tap does not easily induce the pure reversal case as in Furst's experiments [2].

### **4.3.2 Algorithm features: Where to tap the part**

Typically, Thumper II taps the high spot when it is aligned with the tip. However, the device taps the part in different locations when necessary. To correctly position the Thumper II for multiple taps in a single revolution correctly, the part must be tapped at slightly different times to compensate for the amount of spindle rotation during the acceleration phase of the tap. Also, the part can be tapped at a different location to compensate for large drop angle values.

#### *Ensuring correct tap timing*

Multiple taps during one revolution of the part require timing compensation to ensure the taps occur as close as possible to the high spot or other desired location. It is important to note that the time for a single tap is about 250 ms (see Section 4.2.4 for more detail). One cycle includes retracting the coil into the magnet, accelerating the coil to the desired impact velocity and impacting the part. Thus, if the part is being tapped twice in one revolution, then the first tap will occur 125 ms before the desired location and the second tap 125 ms past the desired location. If the part is being tapped three times in one revolution, then the first tap will occur 250 ms before the desired location, the second tap at the location, and the third tap 250 ms after the location.

#### *Drop angle consideration*

To understand how the alignment program uses drop angle information, it is important to understand the geometry of the drop angle as it relates to Thumper II. Figure 34 in Section 1.2.5 introduced the basic geometry for the drop angle and this figure is repeated below in Figure 80.

Figure 80 illustrates the geometry of the drop angle. Figure 80 (a) shows a mass horizontally impacting the part when the highspot (i.e. workpiece center location) is next to the impacting tip. Figure 80 (b) shows a solid circle for the workpiece before the tap and a dotted circle after the workpiece finishes sliding. The drop angle is defined as the angle that the vector between the final and initial part center locations (points 1 and 2 in Figure 80 (b) respectively) forms with the horizontal axis of the rotational coordinate system. From Figure 80 it is clear that the drop angle can be defined with Equation (29) as the arc-tangent of the quotient of the vertical and horizontal displacements. This relation is used in the alignment algorithm to determine the drop angle value.

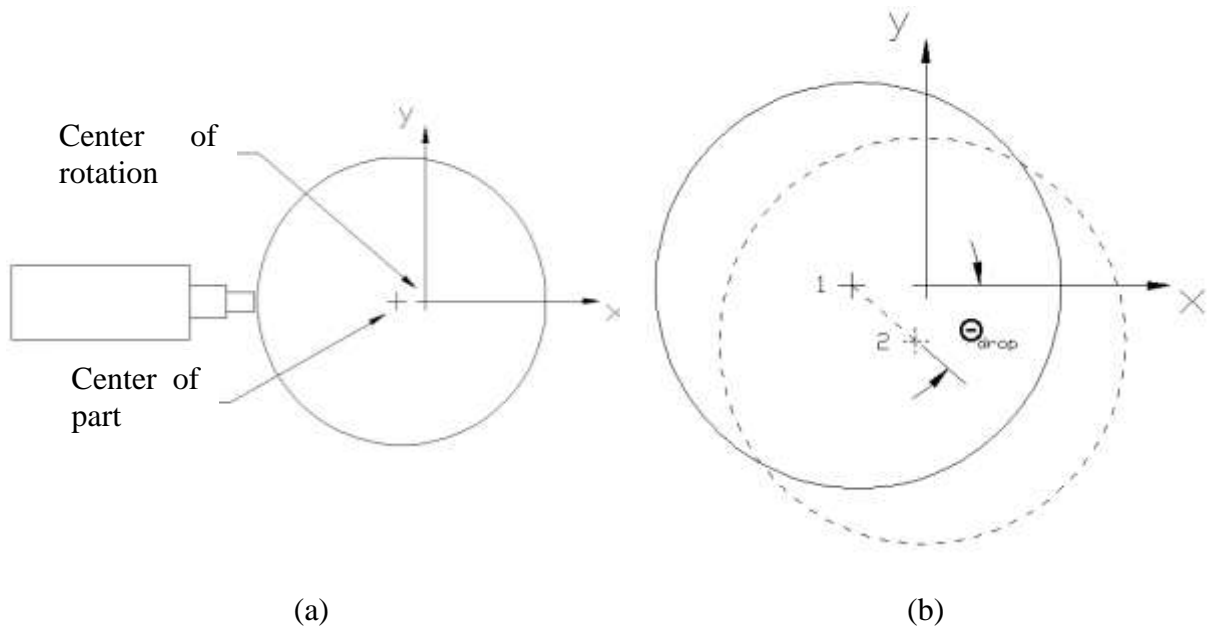


Figure 80. Basic geometry of the (a) coordinate system and (b) drop angle.

Figure 81 shows how Thumper II uses known values to determine the drop angle for a given tap. Figure 81 (a) indicates that a part was tapped when the workpiece center (of 100  $\mu\text{m}$  misalignment) was next to the Thumper II tip (see Figure 80 for Thumper II location). The misalignment after the tap was 100  $\mu\text{m}$  but in a different location. The part moved with a

drop angle of  $45^\circ$  as defined by Figure 80. Even though the high spot location in polar (R- $\theta$ ) coordinates changes by  $\alpha = 90^\circ$ , the drop angle was  $45^\circ$ .

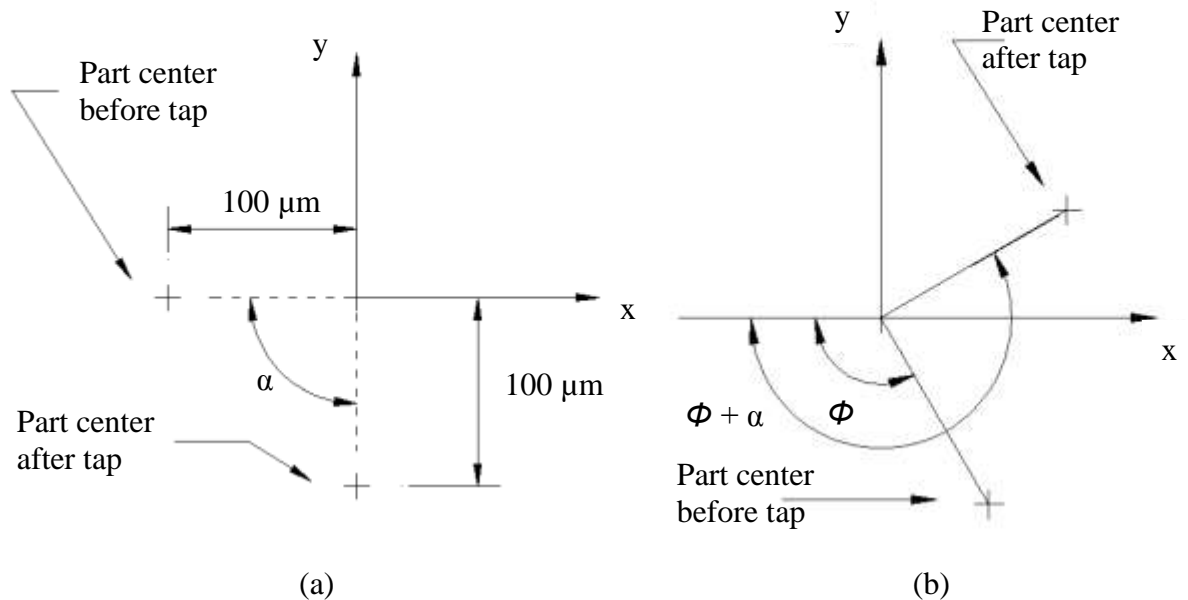


Figure 81. Drop angle geometry (a) for tapping highspot and (b) as used in microcontroller.

To compensate for the drop angle, Thumper II will tap the part when the high spot is above the x-axis seen in Figure 81. More specifically, Thumper II will impact the part when the angle between the vector connecting the highspot and rotation center is rotated clockwise by the amount of the drop angle in Figure 81. In other words, if the highspot is at  $180^\circ$  and the drop angle is  $45^\circ$  as in Figure 81 (a), then the part will be tapped when the highspot is rotated  $45^\circ$  clockwise about the rotational center from the Thumper II tip as seen in Figure 80 (a).

In the actual alignment program, Thumper II must manipulate measured values for high spot location to derive the drop angle. This is illustrated in Figure 81 (b). Figure 81 (b) shows that the part center before the tap will have an arbitrary angular position associated with it in the fictitious coordinate system defined by  $\phi$ . Thus, to correctly calculate the drop angle, both

part centers are rotated about the origin by  $\phi$ , and then Equation (29) in Section 1.2.5 can be applied correctly.

Thumper II handles drop angles in an adaptive manner as follows. Any time a new impact velocity is selected, the high spot of the part is tapped such that the drop angle geometry is easily measured as in Figure 81 and to avoid complications from drop angle variation with impact magnitude as described in Table 6. It is clear from Table 6 that large differences in observed drop angle are possible during one alignment process due to different impact magnitudes being used. The calculated drop angle value is then added to the TDVKA table along with the measured displacement. A tap will take the drop angle into consideration if the velocity has already been used (thus drop angle known) and the drop angle is greater than  $20^\circ$ .

#### *Critical drop angle*

It is possible to determine what size of drop angle significantly affects Thumper II's ability to align a part by just tapping the high spot. Figure 82 shows geometry used to determine the critical drop angle value. The critical drop angle is defined as the angle that makes it impossible to align a part by simply impacting the high spot with an algorithm that selects an impact velocity whose associated part displacement is equal to or near the misalignment value. The  $MA$  parameter in Figure 82 is the misalignment before the tap and the  $\delta$  parameter is the distance the part moves due to the tap.

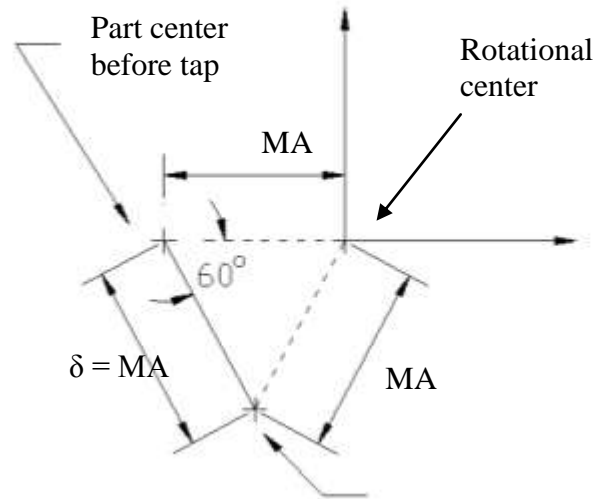


Figure 82. Geometry to determine critical drop angle for tapping high spot.

The critical drop angle is shown to be  $60^\circ$  with the following reasoning:

If the part displacement  $\delta$  equals the misalignment and the drop angle is  $60^\circ$ , then due to the geometry in Figure 82 the misalignment after the tap will be of the same value  $MA$ , it will simply be in a different angular location. This process will repeat indefinitely and the part will never be aligned without compensation for the gravitational effect.

$$\theta_c = 60^\circ \quad (46)$$

The importance of tapping when the high spot is above the horizontal axis in Figure 82 is clear when drop angles are near  $60^\circ$ . Tapping when the high spot is above this axis allows the part to fall due to gravity towards the center. However, even with smaller drop angles, it is important to tap away from the high spot to improve algorithm convergence and to make the alignment process quicker. Section 5.4 details an issue that intermediate drop angle values (around  $30^\circ - 40^\circ$ ) create with the Thumper II algorithm.

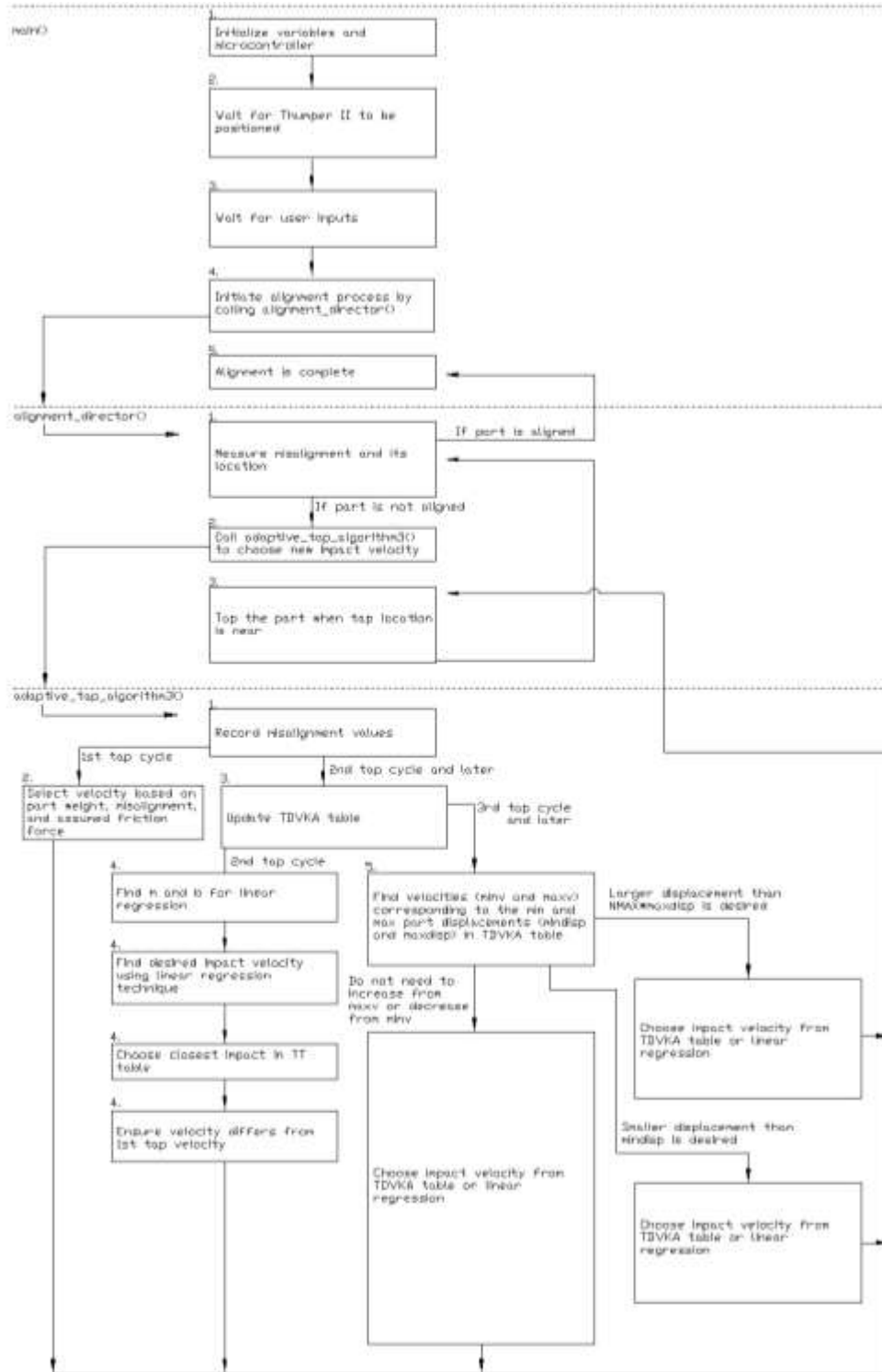


Figure 83. Flow chart for alignment process.

### 4.3.3 How the algorithm features work together

The adaptive tap algorithm must use the features described in Sections 4.3.1 and 4.3.2 properly if the alignment program is to converge successfully. The methodology of the adaptive tap algorithm is important to understand and it is different depending on the number of tap cycles that have already occurred. The basic logic of the algorithm can be understood with the aid of the flow charts in Appendix K in Figure 83. However, the algorithm is explained here in detail.

#### *Selecting impact velocity for the 1<sup>st</sup> tap cycle*

First, the misalignment location  $(R,\theta)$  from the first measurement is entered into an array. For the first tap cycle, the impact velocity is selected using a model-based prediction as described in Section 4.3.1.

#### *Selecting impact velocity for the 2<sup>nd</sup> tap cycle*

The following steps are carried out to select the impact velocity for the 2<sup>nd</sup> tap cycle:

1. The center location  $(R,\theta)$  from the second measurement is entered into an array.
2. The drop angle and part displacement values are calculated using the two center locations that have been recorded. The values for part displacement and drop angle for the first tap are updated in the TDVKA table.
3. The linear regression values  $m$  and  $b$  are found using the impact velocity and part displacement from the first tap, as well as the assumed static friction point.
4. The linear regression values are used to determine an impact velocity that yields the desired part displacement.
5. The impact velocity in Table 27 that is closest to the value chosen in step 4 will be the impact velocity for the 2<sup>nd</sup> tap.
6. If the velocity chosen in step 5 is the same as the velocity for the 1<sup>st</sup> tap, then a tap that is 0.05 m/s greater (or smaller) will be selected for the impact velocity for the 2<sup>nd</sup>

tap. This is to ensure that after the 2<sup>nd</sup> tap, two different impact velocities have been used resulting in a more useful linear regression calculation after the 2<sup>nd</sup> tap.

*Selecting impact velocity for the 3<sup>rd</sup> tap cycle and later*

The complexity of the impact velocity selection process for the 3<sup>rd</sup> tap (and later) cycles is what makes Thumper II a robust alignment device. The following steps are carried out for choosing the impact velocity for the 2<sup>nd</sup> tap cycle:

1. The center location (R,θ) from the most recent measurement is entered into an array.
2. The drop angle and part displacement values are calculated using the two most recent center locations that have been recorded. The values for part displacement and drop angle for the most recent tap are updated in the TDVKA table.
3. The linear regression values  $m$  and  $b$  are found using the impact velocity and part displacement from all taps in the TDVKA table.
4. The minimum and maximum part displacements in the TDVKA table (as well as associated velocities) are determined. These values are used to determine if the impact velocity for the next tap cycle needs to increase from the maximum velocity in the TDVKA or decrease from the minimum.
5. The TDVKA table is scanned to see if any combination (1, 2, or 3 taps in a revolution) of a previously used tap impact velocity will be able to center the part.
6. If there are no suitable velocities in the TDVKA table, then a velocity (and number of impacts) will be selected using linear regression.
7. A check is performed to ensure that the selected velocity (if already present in the TDVKA table) is not less than 2 μm. This is an important step as the linear regression can sometimes select improper velocities. However, the TDVKA table can be used to validate a selection from linear regression.

## 5. Alignment Testing

### 5.1 Part alignment testing overview

Overall, Thumper II executes the part alignment procedure in a quick, precise, and consistent manner. Figure 59 shows Thumper II set-up for alignment on the OC and IC chucks. A list of all alignment tests carried out by Thumper II is in Table 26 Appendix B which includes the part and chuck that were used for each test, the process time, initial misalignment, and final misalignment.

The average process time for the five numbered parts in Table 26 is 1:36 (min:sec) with a final misalignment less than  $2.5 \mu\text{m}$  at a spindle speed of 16 RPM. The minimum and maximum times were 0:47 and 2:13 respectively. The average initial and final misalignment values for these tests are  $135.6 \mu\text{m}$  and  $2.06 \mu\text{m}$ . For all tests in this thesis, the process time includes about 10 seconds for operator input and initial data transfer between the UI and microcontroller. Recalling Table 11, the TIR measurement method is less robust than the LSC measurement at spindle speeds  $\geq 8$  RPM. Thus, only the LSC measurement is considered for all testing in Section 5.

### 5.2 Understanding the alignment process

Polar plots like Figure 84 are useful for analyzing the efficiency of the alignment process, as well as for observing some characteristics of aligning parts under different conditions. In Figure 84, each circle represents an individual measurement of the center location and a line connects one measurement to the next. The angular values are those that are determined by Thumper II during run-time.

For the alignments in Figure 84, the highspot is tapped each time (i.e. no correction for the drop angle is used). This means that the alignments take more iterations than if the drop angle were considered. However, tapping the highspot directly helps to develop a better understanding of part displacement behavior.

*Effect of part weight on alignment process (without drop angle compensation)*

Figure 84 shows a plot of the alignment process at a vacuum of 11.1 psi on the OC chuck for two parts of equal diameter but unequal weight. In both cases, the workpiece begins at a misalignment of about 150  $\mu\text{m}$  and ends with a final misalignment of about 3  $\mu\text{m}$ . The radial axis uses a logarithmic scale. The 1 lb part displaces in the direction of the center of rotation for each tap. The 30 lb part, however, follows a less direct path towards the center of rotation due to a larger drop angle. Thus, Figure 84 demonstrates the additional challenge of centering a heavy part on a vertical chuck face.

One interesting observation from Figure 84 is that the alignment process generally spends a significant amount of iterations around the target goal. This is to be expected as variations in friction and displacement direction make it challenging to precisely position a workpiece. It should be realized that the angle drop capability was turned off to make the plots in Figure 84 so that the effect of part weight on the alignment process could be better observed.

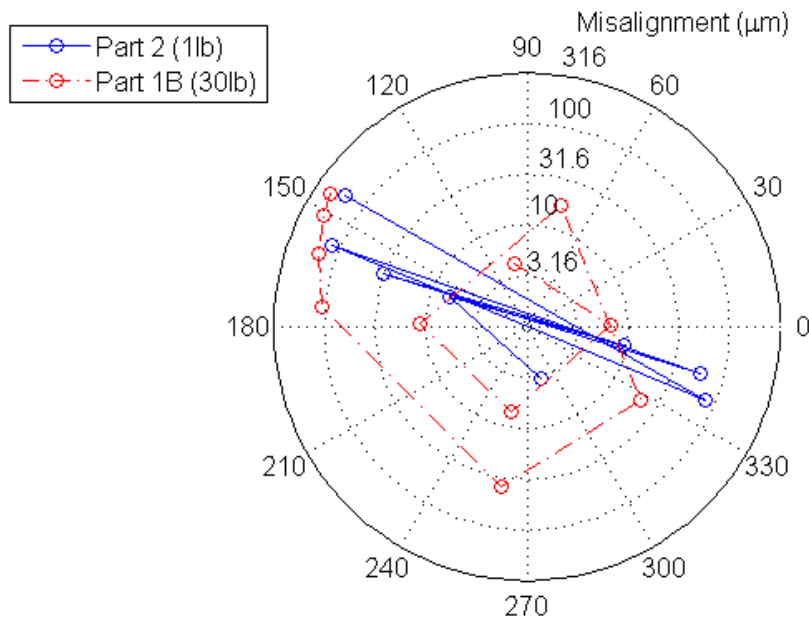


Figure 84. Polar plot of center locations during alignment at two part weights on a logarithmic radial scale.

### 5.3 Compensating for drop angles

If large drop angles are present, it may not be possible to align a part to 2.5  $\mu\text{m}$  precision by simply tapping the highspot. To achieve the target misalignment at high drop angles, it is necessary to tap the workpiece when the highspot is above the Thumper II tip, such that the part will fall towards the rotational center as well as displace horizontally.

Figure 85 shows a polar plot of part center locations for a case when the part is only tapped at the highspot, and a case when the part is tapped away from the highspot to facilitate proper displacement direction. For both cases, the alignment tests occurred at 8 RPM, using part 1B (30 lb) on the OC chuck at a vacuum of 10.2 psi. Figure 85 is for alignment on the OC chuck, however, the same behavior is witnessed for alignment on the IC chuck.

As seen in Figure 85, the workpiece could not be aligned by simply tapping the highspot. In five cycles of tapping only the highspot, the workpiece misalignment remained around 100  $\mu\text{m}$ . However, with five taps using drop angle compensation, the workpiece was aligned to 1.97  $\mu\text{m}$ . It is important to note that the first three measurements are about the same ( $\sim 100$   $\mu\text{m}$ ) for the case where drop angle compensation was used. This is because for the first and second tap, drop angle values were calculated and used in the third tap and later.

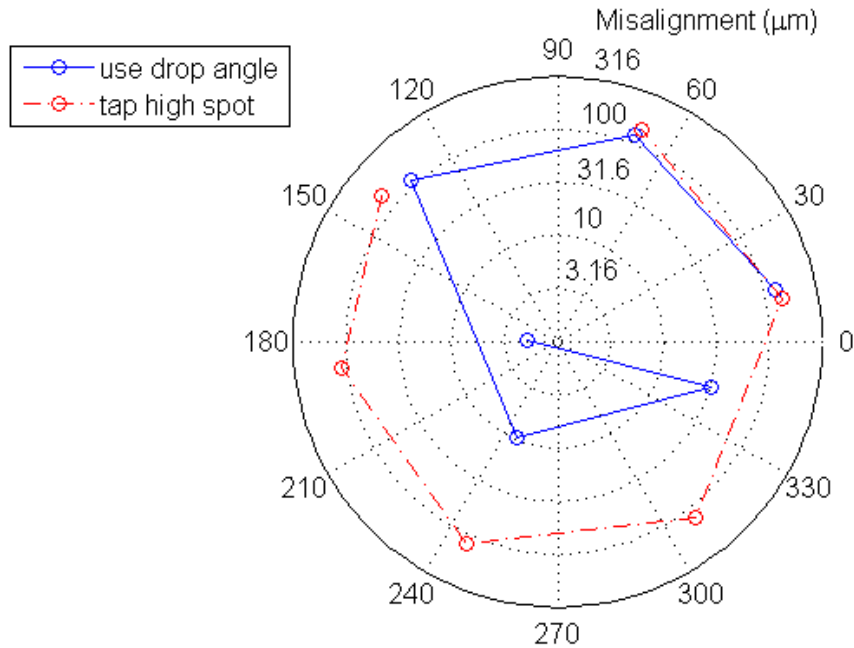


Figure 85. Thumper II overcoming large drop angle.

Table 27 shows the drop angle values observed for the alignments in Figure 85. These were the drop angle values populated in the TDVKA during the alignment process as described by Table 18. A range of  $51^\circ$  to  $67^\circ$  was observed. Another interesting note from Table 27 is that the drop angle increases with decreasing impact velocity which agrees with the prediction from the 2D part motion model. Thus, it can be useful to calculate a drop angle for each a new velocity used.

Table 19. Drop angle values for two alignments.

	Drop angle (impact velocity)		
Use drop angle	56° (1.10 m/s)	57° (1.05 m/s)	67° (0.70 m/s)
Tap highspot	51° (1.10 m/s)	62° (1.05 m/s)	-

## 5.4 Alignment at various vacuum pressures on OC and IC chucks

Thumper II has been tested and proven to be effective over a large range of vacuum pressures. The ability of Thumper II to quickly align various workpieces over these wide vacuum ranges indicates the adaptability of the device to operate effectively under a large range of conditions.

### 5.4.1 Varying vacuum pressures on the OC chuck

Table 20 shows three parts aligned on the OC chuck at various vacuum pressures. The values in Table 20 and Table 21 are averages for two runs at the specified vacuum pressure. The misalignment target was 5 µm for these tests at a spindle speed of 8 RPM. For parts 2 and 1A, Thumper II is able to align the part efficiently from about 5-11 psi. A smaller vacuum range was used for the 30 lb workpiece (part 1B) as this part falls off the chuck at a vacuum  $\leq$  10 psi. The process time includes about 10 seconds for operator input and initial data transfer between the UI and microcontroller.

Table 20. Alignment process at various vacuums on the OC chuck.

Part No.	Number of Measurement Cycles	Time (min:sec)	Vacuum (psi)	Misalignment	
				Initial ( $\mu\text{m}$ )	Final ( $\mu\text{m}$ )
2 (1 lb)	8	2:26	11.1	178.1	2.31
	13	2:09	7.6	233.8	2.58
	7	1:43	5.1	321.6	1.36
1A (14 lb)	6	1:48	11.1	164.2	3.37
	5	1:34	7.9	186.1	3.51
	14	4:04	5.2	228.2	3.59
1B (30 lb)	12	3:23	11.1	200.6	3.36
	8	2:15	10.2	151.8	2.60

#### 5.4.2 An alignment inefficiency and its solution

One interesting observation from Table 20 reveals inefficiency with the Thumper II algorithm. The effect of this inefficiency is seen in that the average misalignment time for part 1A at 11.1 psi and 7.9 psi are 1:48 and 1:34, while the average alignment time at 5.2 psi is significantly greater at 4:04. The reason for this occurrence, and a solution, can be clearly explained.

Table 28 and Table 29 in Appendix D helps show why this drastic change in alignment time is observed. First, Table 28 shows that 16 measurement cycles occurred, and that there are small (i.e. gradual) improvements on the misalignment between each measurement from measurements 6 – 16. These steps towards alignment are small and gradual due to the fact that a new velocity is used for nearly every tap, as seen in Table 29.

Recalling Section 4.3.2, each time a new velocity is used, the highspot is tapped and the drop angle is calculated for that velocity. Thus, for the alignment process in Table 28 and Table 29, the drop angle (an average of  $33.3^\circ$  for all velocities) is such that a new misalignment is slightly smaller than the previous misalignment. However, this decrease is large enough that a new velocity is selected for the next tap, leading to a small decrease in the misalignment due to the drop angle. This process repeats with small improvements until the part is

sufficiently aligned, but results in a longer than usual process time. The most important conclusion from this observation of inefficiency and the results in Table 20 is that the inefficiency can be eliminated by simply using a different vacuum pressure determined by trial and error.

### 5.4.3 Varying vacuum pressures on the IC chuck

Table 21 shows three parts aligned on the IC chuck at various vacuum pressures. The vacuum pressure was varied by loosening a fitting to introduce leakage into the vacuum hose. The initial misalignments are much larger on the IC chuck than the OC chuck because the raised area on the OC chuck limits the maximum possible initial misalignment (see Figure 2).

Table 21. Alignment process at various vacuums on the IC chuck.

Part No.	No. of Measurement Cycles	Time (min:sec)	Vacuum (psi)	Misalignment	
				Initial ( $\mu\text{m}$ )	Final ( $\mu\text{m}$ )
2 (1 lb)	7	1:56	10.3	877.5	2.47
	8	1:56	6.9	1,134.5	4.15
	8	2:19	4.7	975.3	2.01
3A (15 lb)	12	2:15	10.8	918.5	1.58
	13	2:27	7.1	1020.1	1.95
	14	2:27	3.4	998.4	0.96
3B (25 lb)	23	4:06	10.8	622.6	1.37
	13	2:20	7.1	808.1	1.46
	14	2:30	3.4	1030.6	0.89

Two key conclusions can be drawn from Table 20 and Table 21. First, that the Thumper II can be used under a wide range of conditions and that its adaptive algorithm is robust. One of the key aspects of the adaptive algorithm is the 0.05 m/s resolution for impact velocity. The ability for the device to effectively align 1 – 30 lb parts on the both chucks suggests that this velocity resolution is sufficient to align a wide range of parts.

The second conclusion is that the Thumper II, for certain parts, is significantly more effective at specific vacuum pressures. For example, for part 1A in Table 20, the alignment time of 1 – 2 minutes for vacuums of 11.1 psi and 7.9 psi is significantly better than the roughly 4 minute alignment time at the lowest vacuum pressure, 5.2 psi. However, part 2 in Table 20 was shown to be aligned quickest at the lowest vacuum pressure.

## 5.5 Alignment at various spindle speeds

Thumper II can operate at a variety of spindle speeds, though there is a range of speeds that corresponds to the most efficient and reliable alignment process. Slow spindle speeds (e.g. 4 RPM) have the problem that time is wasted waiting for the highspot after completion of a measurement cycle. Also, the measurement cycle at low spindle speeds takes considerably longer than at higher speeds. However, higher spindle speeds may be a challenge because of the higher surface speed and greater spindle rotation during part sliding.

Table 22 shows the time for alignment for three spindle speeds. Each alignment time is an average of three tests at the specified speed. As seen, the time it takes to align the part decreases as the spindle speed increases. This trend is also witnessed for alignment on the IC chuck. The shorter alignment times for 16 RPM show that this higher speed is more desirable for Thumper II.

Table 22. Alignment process time on the OC chuck at varying spindle speeds.

Part No.	Spindle speed (RPM)	Alignment time (min:sec)	Misalignment	
			Initial ( $\mu\text{m}$ )	Final ( $\mu\text{m}$ )
1A (14 lb)	4	2:42	129.3	2.25
	8	2:22	132.0	1.84
	16	1:02	132.4	1.88
1B (30 lb)	4	5:38	130.1	2.02
	8	4:02	126.6	2.05
	16	2:04	133.5	1.99

## 5.6 Final misalignment and process time

Thumper II continuously taps and measures until the measured misalignment is less than the target. In general, smaller target misalignment values result in a longer duration of alignment process. It is useful to know how the process time changes with misalignment target to aid in selecting the appropriate alignment target to use for a given application. Table 23 shows the time it takes for a part to be aligned from an average initial misalignment of about 135  $\mu\text{m}$  to a desired target misalignment. The values in Table 23 were from tests performed on the OC chuck at 11.1 psi and 16 RPM. Each time value is the average of three trials.

As indicated in Table 23, smaller target misalignments result in a longer process time. This is to be expected as friction and displacement direction variations are less important at larger misalignment targets.

Table 23. Process time (min:sec) and final misalignment.

Part No.	Run	Target misalignment value		
		10 $\mu\text{m}$	5 $\mu\text{m}$	2.5 $\mu\text{m}$
1A	1	0:47	0:50	1:53
	2	0:45	1:03	1:18
	3	0:48	1:31	2:02
	Average	0:47	1:08	1:44
1B	1	1:47	1:48	2:00
	2	1:18	1:22	2:11
	3	1:10	1:46	2:02
	Average	1:25	1:39	2:04

## 6. Conclusions and Future Work

### 6.1 Objectives & Summary

The objectives of this thesis were to design and develop an automated device capable of high precision part alignment on a vacuum chuck. The Thumper II design criteria are listed below.

- Measure and correct part runout of up to 2.5 mm on the IC chuck up to 250  $\mu\text{m}$  on the OC chuck.
- Center parts to a runout of less than 5 $\mu\text{m}$  (i.e. misalignment less than 2.5  $\mu\text{m}$ ).
- Align parts weighing 5-35 lbs with 6-8 inch nominal outer diameter.
- Automatic process with little operator interaction.
- No interaction with or control of machine spindle or axes.
- Align part in less than 4 minutes.

Thumper II meets all of the criteria, showing that a highly automated device can precisely align workpieces on a turning machine. The device is compact enough to fit inside of a diamond turning machine. The Thumper II tool is operated by an easy-to-use GUI running on a PC. This makes the task for the operator safe, simple, and effortless. The device is compact enough to fit in most large CNC turning machines. The low process times make it a viable solution for industrial automation of part centering, and its adaptability to arbitrary machines (i.e. no signal connection to the machine) makes it functional for many applications.

### 6.2 Results

On the OC chuck, the Thumper II device showed an average alignment time to 2.5  $\mu\text{m}$  at 16 RPM of 1:36 for all parts on the OC chuck. The minimum and maximum times on the OC chuck were 0:47 and 2:13 respectively. On the IC chuck, the Thumper II device showed an average alignment time of 2:26 minutes for all tests. For all tests, the process time includes

about 10 seconds for operator input and initial data transfer between the UI and microcontroller.

### **6.3 Improvements and Future Work**

Thumper II successfully shows that precise part alignment can be automated with a compact device, yet there are multiple improvements that could be made to the device.

#### *Device design*

Some parts of the Thumper II structure could be improved. One issue with the design is that the bolt in the connection between the coil and rail comes loose after aligning about 50–100 parts. This is problematic as the coil is no longer aligned in the magnet and can rub against the magnet. Another, less likely, problem with this loose bolt is that if the two connector pieces were to come apart, the top connector piece might not contact the stop and thus impact the encoder readhead. This problem was solved by adding Loctite to the bolt-nut connection. Redesigning this connector must take into account that if the rail is magnetic (which is true for the Thumper II), then there will be a strong magnetic force attracting the rail to the magnet when the coil and rail are close.

The Thumper II device was designed to be powerful enough to align a 35 lb part (with 2.5 mm initial runout) at high vacuum pressure to a final misalignment of 2.5  $\mu\text{m}$ . This fact led to the selection of a larger motor than Thumper I. A device with a smaller motor, but that taps at a higher frequency ( $>5$  Hz), could be used in lieu of Thumper II. The advantage here could be a smaller device.

Since Thumper II was designed for quickly aligning 35 lb workpieces with large vacuum pressure and runout, it would likely be too powerful to align light parts ( $\ll 1$  lb) at small vacuum levels. One simple solution would be to change the tip material. Recalling Figure 17, the tip material could be changed to result in a smaller peak force imparted to the part for a given impact velocity.

### *Alignment process*

There are also improvements that could be made to the alignment process and algorithm.

One modification to the algorithm would be to abandon the method of tapping the highspot and calculating a new drop angle every time a new impact velocity is used. Instead, the drop angle that has already been calculated from a different impact velocity could be used to ensure that the next tap occurs in a more appropriate position. Applying this method would require a more complicated geometrical interpretation to determine the new drop angle value.

One addition that could significantly speed up the alignment process in certain conditions is to skip measurement cycles. As seen earlier, under certain conditions, the location of the high spot changes little from one tap to the next when the runout is relatively large (e.g. Figure 84). The alignment algorithm could take this into account and skip measurement cycles when it is confident that the location of the high spot has not changed significantly due to the previous tap cycle.

Lastly, Thumper II operates on key operator inputs: spindle speed, part weight, and vacuum pressure. However, it is easy to imagine Thumper II operating with no operator inputs and simply starting the measurement-tapping routine when commanded. In this way, Thumper II could deduce the spindle speed by fitting the measurement data (such as in Figure 63) to a sine wave, and make initial taps based on a conservative starting point. The same algorithm for velocity prediction, drop angle, etc. could still be used. Making these minor modifications to Thumper II could result in a device that requires zero user input or interaction.

## References

- [1] R. G. Longoria, "Notes on LVDTs," 11 January 2012. [Online]. Available: <http://www.me.utexas.edu/~dsclab/labs/forcemotion/lvdt.html>. [Accessed 2012 26 February].
- [2] S. Furst, "Automatic Handling Technology for Precision Turning of Two-Sided Parts," Master's Thesis, North Carolina State University, Raleigh, NC, 2008.
- [3] Precitech, "Part Centering: Precitech Part Centering Accessory," 4 February 2011. [Online]. Available: <http://precitech.com/Brochures/Part%20Centering%20Accessory.pdf>. [Accessed 19 December 2011].
- [4] R. J. Roark, Formulas for Stress and Strain, New York, NY: McGraw-Hill, 1975.
- [5] M. & B. Shigley, "Mechanical Engineering Design: Tutorial 4-20: Hertz Contact Stresses," 5 January 2012. [Online]. Available: <http://www.scribd.com/doc/9724081/Hertz-Contact-Stresses>. [Accessed 2012 January 2012].
- [6] T.-R. Hsu, "Introduction to Finite Difference Method for Solving Differential Equations," 23 November 2009. [Online]. Available: <http://www.engr.sjsu.edu/trhsu/Chapter%209%20Intro%20to%20FDM.pdf>. [Accessed 18 July 2012].
- [7] MatWeb, "Overview of materials for Acrylic, Extruded," 19 April 2012. [Online]. Available: <http://www.matweb.com/search/DataSheet.aspx?MatGUID=632572aeef2a4224b5ac8fbd4f1b6f77>. [Accessed 19 April 2012].
- [8] MatWeb, "Overview of materials for Nylon 6, Impact Grade," 19 April 2012. [Online]. Available:

- <http://www.matweb.com/search/DataSheet.aspx?MatGUID=e88fcee0e24c49c7864b00d10642c5c9>. [Accessed 19 April 2012].
- [9] MatWeb, "Aluminum, Al," 24 April 2012. [Online]. Available: <http://www.matweb.com/search/DataSheet.aspx?MatGUID=0cd1edf33ac145ee93a0aa6fc666c0e0>. [Accessed 24 April 2012].
- [10] MatWeb, "Overview of materials for Stainless Steel," 24 April 2012. [Online]. Available: <http://www.matweb.com/search/DataSheet.aspx?MatGUID=71396e57ff5940b791ece120e4d563e0>. [Accessed 24 April 2012].
- [11] T. K. Kiong, L. T. Heng and H. Sunan, Precision Motion Control, 2nd Edition, London: Springer, 2008.
- [12] Y. Koren, "Control of Machine Tools," *Journal of Manufacturing Science and Engineering*, vol. 119, pp. 749-755, 1997.
- [13] G. Morel and S. Dubowsky, "The Precise Control Of Manipulators With Joint Friction: A Base Force/Torque Sensor Method," in *IEEE International Conference on Robotics and Automation*, Minneapolis, 1996.
- [14] C. Canudas de Wit, H. Olsson, K. J. Åström and P. Lischinsky, "A New Model for Control of Systems with Friction," *IEEE Transactions on Automatic Control*, vol. 40, no. 3, pp. 419-425, 1995.
- [15] B. Armstrong-Hélvoury, P. Dupont and C. Canudas De Wit, "A Survey of Models, Analysis Tools and Compensation Methods for the Control of Machines with Friction," *Automatica*, vol. 30, no. 7, pp. 1083-1138, 1994.
- [16] University of Washington, "Introduction to Tribology - Friction," 6 February 2007. [Online]. Available: <http://depts.washington.edu/nanolab/ChemE554/Summaries%20ChemE%20554/Intro>

uction%20Tribology.htm. [Accessed 26 April 2012].

- [17] C. Iurian, F. Ikhoulane, J. Rodellar and R. Griñó, "Identification of a system with dry friction," Reports of Institut d'Organització i Control de Sistemes Industrials, Catalunya, 2005.
- [18] BEI Kimco Magnetics, "Voice Coil Actuators: Applications and Product Selection Guide," 17 July 2009. [Online]. Available: <http://www.beikimco.com/pdf/VCA%20App%20Product%20Guide.pdf>. [Accessed 13 January 2012].
- [19] THK, "Caged Ball LM Guide: SSR," 14 April 2010. [Online]. Available: [https://tech.thk.com/upload/catalog\\_claim/pdf/212E\\_SSR.pdf](https://tech.thk.com/upload/catalog_claim/pdf/212E_SSR.pdf). [Accessed 27 January 2012].
- [20] K. Creath and J. C. Wyant, "Moiré and Fringe Projection Techniques," in *Optical Shop Testing, Second Edition*, John Wiley & Sons, 1992.
- [21] Renishaw, "Non-contact position encoders," 2007.
- [22] Advanced Motion Controls, [Online]. Available: <http://www.a-m-c.com/download/support/psselection.pdf>. [Accessed 24 December 2011].
- [23] G. Taubin, "Estimation of Planar Curves, Surfaces, and Nonplanar Space Curves Defined by Implicit Equations with Applications to Edge and Range Image Segmentation," *IEEE Transactions on Pattern Analysis and Machine Intelligence*, vol. 13, no. 11, p. 24, 1991.
- [24] N. Chernov, "Circle Fit (Taubin method)," 13 January 2009. [Online]. Available: <http://www.mathworks.com/matlabcentral/fileexchange/22678>.
- [25] "Spherical Cap," Wolfram MathWorld, 2012 2 July. [Online]. Available: <http://mathworld.wolfram.com/SphericalCap.html>. [Accessed 2012 2 July].

- [26] J.-X. Wang and M.-Y. Gu, "Wear properties and mechanisms of nylon and carbon-fiber reinforced nylon in dry and wet conditions," vol. 93, no. 2, July 2004.
- [27] J.-X. Wang and M.-Y. Gu, "Investigation of the Influence of CuO Filler and Carbon Fiber on Wear and Transfer Film of Nylon Composites," vol. 91, no. 4, May 2003.
- [28] Wikipedia, "Simple linear regression," 09 April 2012. [Online]. Available: [http://en.wikipedia.org/wiki/Simple\\_linear\\_regression](http://en.wikipedia.org/wiki/Simple_linear_regression). [Accessed 10 April 2012].

## Appendices

Appendix A. **Parts and chucks used for centering experiments**



Figure 86. Parts and chucks used for centering experiments.

Table 24. Parts used in Thumper II testing/development.

Part No.	Shape / Material / Weight (lb) / OD (in)	Details (See Figure 86)
1A	Cylinder / 304SS / 14.25 / 6	Labeled as 1A in Figure 86
1B	Cylinder / 304SS / 30 / 6	Part 1B is formed by bolting together part 1 and the adjacent cylindrical part.
2	Hollow hemishell / AL6061 / 1.25 / 6	Labeled as 2 in Figure 86
3A	Solid hemisphere / 304SS / 15 / 6	Labeled as 3A in Figure 86
3B	Solid hemisphere with added mass / 304SS / 25 / 6	Part 3B is formed by bolting together part 3A and the adjacent cylindrical pieces.

Table 25. Chucks used in Thumper II testing/development.

Chuck No.	Description Chuck type / Material	Picture
1	OC / AL6061	See Figure 2
2	IC / AL6061	See Figure 2

## Appendix B. Master list of centering tests

Table 26. List of all recorded centering tests.

Alignment #	Part #	Chuck #	RPM	Time (min:sec)	Vacuum (psi)	Initial MA ( $\mu\text{m}$ )	Final MAnt ( $\mu\text{m}$ )
120408-1	1A	1	8	1:55	11.3	143.7	4.76
120408-2	1A	1	8	1:40	11.3	144.1	2.91
120409-1	1B	1	8	-	11.3	128.7	3.91
120409-2	1B	1	8	-	11.3	172.4	2.10
120409-3	2	1	8	-	11.3	130.2	1.80
120409-4	2	1	8	1:00	11.3	148.2	3.94
120409-5	2	1	8	1:06	11.3	149.9	3.62
120409-6	1B	1	8	2:58	11.3	136.4	3.28
120409-7	1B	1	8	2:18	11.3	130.0	4.59
120419-2	2	2	8	1:44	10.5	160.6	3.00
120419-3	2	2	8	1:58	10.5	1084.0	3.68
120419-4	2	2	8	5:15	10.5	1953.1	3.30
120514-1	1A	1	8	1:44	11.1	162.3	3.38
120514-2	1A	1	8	1:52	11.1	166.1	3.36
120514-3	1A	1	8	1:32	7.86	212.1	3.88
120514-4	1A	1	8	1:36	7.86	160.0	3.13
120514-5	1A	1	8	2:40	5.84	202.6	2.77
120514-6	1A	1	8	2:40	5.84	209.0	2.83
120514-7	1A	1	8	4:35	5.16	294.3	3.26
120514-8	1A	1	8	3:33	5.16	162.0	3.92
120515-1	1B	1	8	3:33	11.1	176.6	2.41
120515-2	1B	1	8	3:13	11.1	224.6	4.31
120515-4	2	1	8	2:41	11.1	161.8	3.39
120515-5	2	1	8	2:12	11.1	194.3	1.23
120515-6	2	1	8	1:42	7.56	177.0	3.41
120515-7	2	1	8	2:36	7.56	290.6	1.75
120515-8	2	1	8	-	5.12	152.1	-
120515-9	2	1	8	1:43	5.12	321.6	1.36
120515-10	2	1	8	6:00	3.24	206.1	15.20
120515-11	2	1	8	1:56	3.24	424.9	3.69
120516-1	2	2	8	2:03	10.3	1162.5	2.72
120516-2	2	2	8	1:45	10.3	775.0	4.03
120516-3	2	2	8	2:00	10.3	695.5	0.66
120516-4	2	2	8	1:26	6.88	1197.2	3.83
120516-5	2	2	8	2:26	6.88	1072.5	4.47
120516-6	2	2	8	2:13	4.71	1044.4	3.23

120516-7	2	2	8	2:26	4.71	906.6	0.79
120517-1	1B	1	8	1:48	10.2	130.8	1.97
120517-2	1B	1	8	2:43	10.2	172.8	3.22
120529-1	1A	1	16	1:31	11.1	128.6	2.32
120529-2	1A	1	16	0:54	11.1	134.4	1.13
120529-3	1A	1	16	1:20	11.1	134.1	2.19
120529-4	1A	1	8	2:21	11.1	131.9	1.67
120529-5	1A	1	8	2:43	11.1	132.0	2.00
120529-6	1A	1	8	2:01	11.1	145.1	1.86
120529-7	1A	1	4	2:55	11.1	129.2	2.05
120529-8	1A	1	4	1:56	11.1	129.4	2.45
120529-9	1A	1	4	3:15	11.1	149.1	2.08
120529-10	1B	1	16	2:13	11.1	132.9	2.34
120529-11	1B	1	16	2:06	11.1	132.9	1.18
120529-12	1B	1	16	1:53	11.1	134.7	2.45
120529-13	1B	1	8	3:42	11.1	131.7	2.35
120529-14	1B	1	8	4:45	11.1	125.6	1.40
120529-15	1B	1	8	3:40	11.1	122.5	2.39
120529-16	1B	1	4	5:38	11.1	130.1	2.02
120611-1	1A	1	16	0:47	11.1	129.1	2.15
120611-2	1A	1	16	0:45	11.1	141.0	3.76
120611-3	1A	1	16	0:48	11.1	148.1	2.33
120611-4	1A	1	16	0:50	11.1	153.4	2.33
120611-5	1A	1	16	1:03	11.1	144.1	2.90
120611-6	1A	1	16	1:08	11.1	133.5	4.52
120611-7	1A	1	16	1:53	11.1	129.5	2.12
120611-8	1A	1	16	2:02	11.1	137.5	1.96
120611-9	1B	1	16	1:47	11.1	142.9	8.68
120611-10	1B	1	16	1:18	11.1	129.2	7.46
120611-11	1B	1	16	1:10	11.1	134.0	8.09
120611-12	1B	1	16	1:48	11.1	127.2	3.89
120611-13	1B	1	16	1:22	11.1	124.1	2.98
120611-14	1B	1	6	1:46	11.1	127.3	4.24
120611-15	1B	1	16	2:00	11.1	133.0	2.13
120611-16	1B	1	16	2:11	11.1	132.0	1.91
120611-17	1B	1	16	2:02	11.1	137.9	2.35
120705-1	3A	2	16	2:22	10.8	864.5	1.02
120705-2	3A	2	16	2:09	10.8	972.50	2.14
120705-3	3A	2	16	2:19	7.1	1014.30	2.37
120705-4	3A	2	16	2:35	7.1	1025.8	1.53
120705-5	3A	2	16	2:44	3.4	1050.8	0.78
120705-6	3A	2	16	2:10	3.4	945.9	1.15

120705-7	3B	2	16	3:41	10.8	672.7	2.01
120705-8	3B	2	16	4:32	10.8	572.4	0.72
120705-9	3B	2	16	2:24	7.1	756.0	1.45

## Appendix C. Parameters used by Thumper II for tapping

The values in Table 27 show the empirical values that Thumper II uses to create a tap. The highlighted columns are actually hardcoded onto the microcontroller and used for tapping, expect for the peak force which is used for sizing the first and second taps. Figure 87 shows the high-step and low-step voltages plotted against impact velocity.

Table 27. Empirical parameters for performing taps.

Velocity (m/s)	High voltage step		Low voltage step			Peak force (N)
	High voltage (V)	DAC value	Low voltage (V)	DAC value	time (ms)	
0.15	4.03	6600	3.48	5700	128	75
0.20	4.82	7900	4.24	6950	96	124
0.25	5.95	9750	4.88	8000	80	163
0.30	6.71	11000	5.64	9250	64	210
0.35	8.24	13500	6.41	10500	54	259
0.40	9.77	16000	7.02	11500	48	301
0.45	10.99	18000	7.71	12625	44	346
0.50	12.09	19800	8.24	13500	36	379
0.55	13.21	21650	9.00	14750	36	428
0.60	14.31	23450	9.55	15650	32	464
0.65	15.41	25250	10.16	16650	28	505
0.70	16.51	27050	10.68	17500	24	538
0.75	17.70	29000	11.59	19000	20	583
0.80	18.92	31000	12.51	20500	16	619
0.85	20.14	33000	13.42	22000	12	652
0.90	21.36	35000	14.34	23500	12	684
0.95	22.43	36750	15.11	24750	10	725
1.00	23.50	38500	15.72	25750	10	766
1.05	24.72	40500	16.33	26750	10	815
1.10	25.94	42500	16.85	27600	10	855
1.15	27.16	44500	17.40	28500	10	904
1.20	28.23	46250	17.94	29400	10	953
1.25	29.30	48000	18.46	30250	10	1010

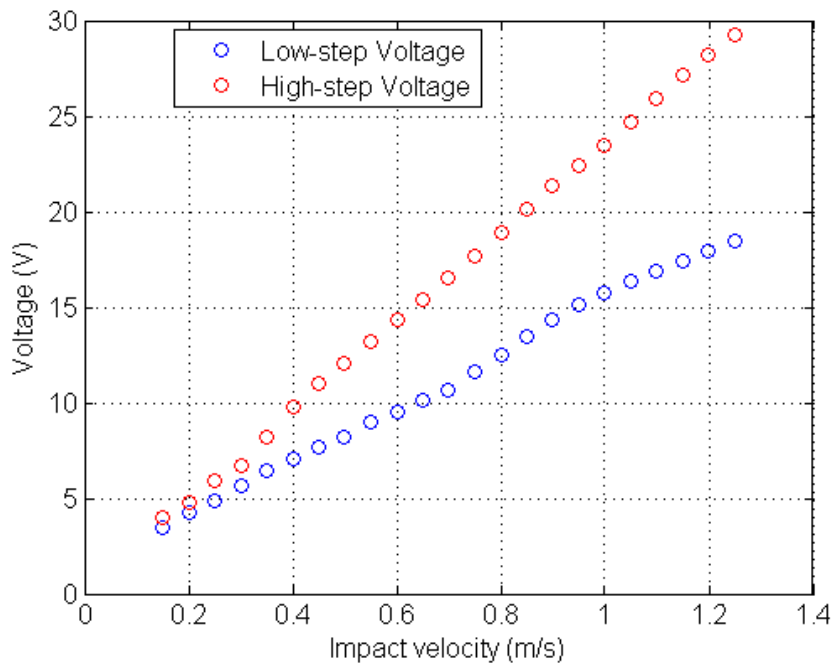


Figure 87. High-step and low-step voltages used for impacts.

## Appendix D. Linear relation data for adaptive algorithm

This appendix supports Section 4.3.1. Figure 79 and Figure 88 – Figure 90 show that the linear relation between part displacement and impact velocity squared holds for many conditions.

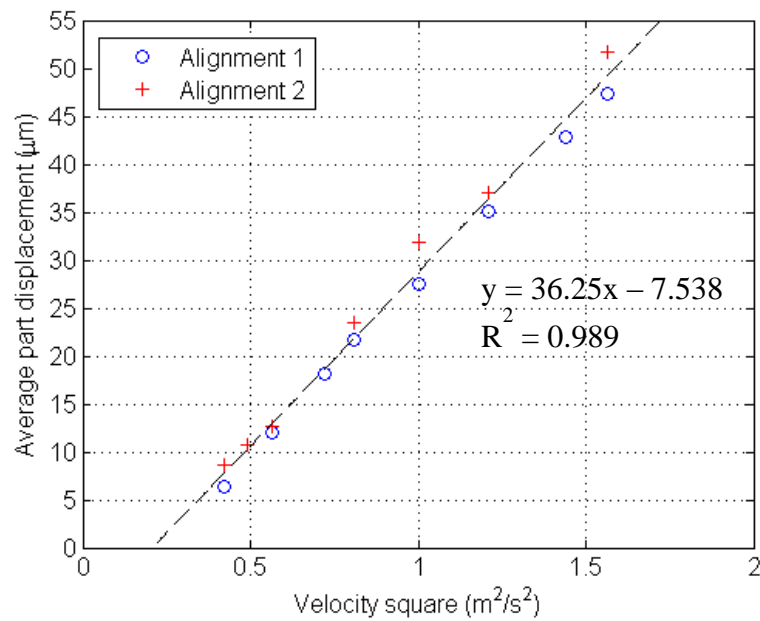


Figure 88. Values from actual TDVKA tables for part 2 on the OC chuck at 11.1 psi.

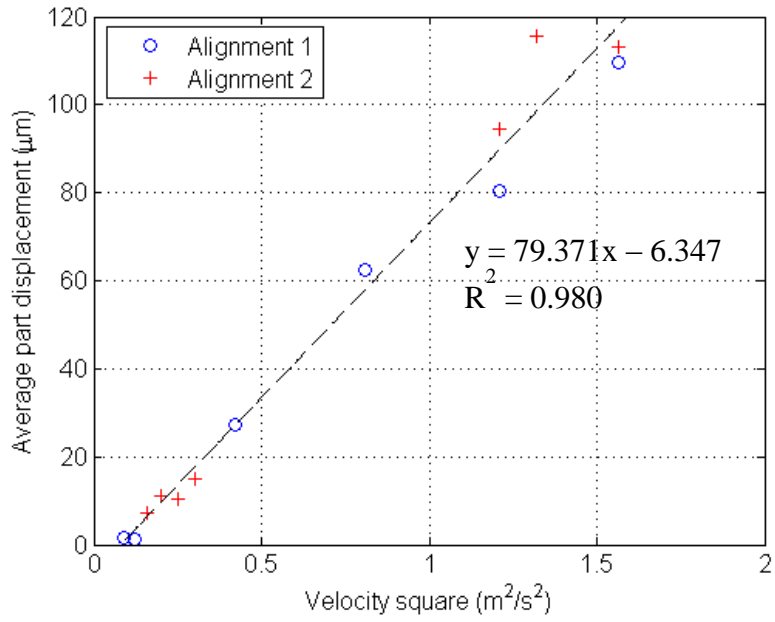


Figure 89. Values from actual TDVKA tables for part 3A on the IC chuck at 7.1 psi.

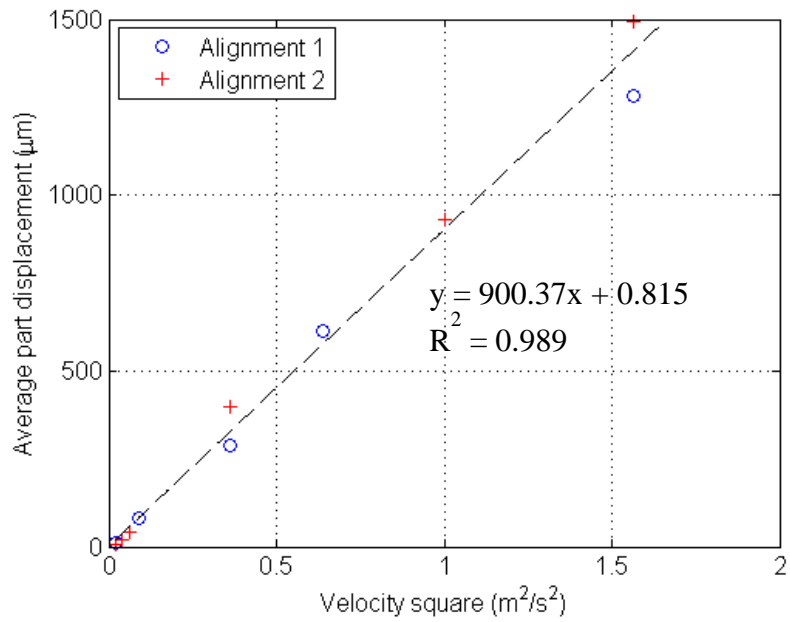


Figure 90. Values from actual TDVKA tables for part 2 on the IC chuck at 11.1 psi.

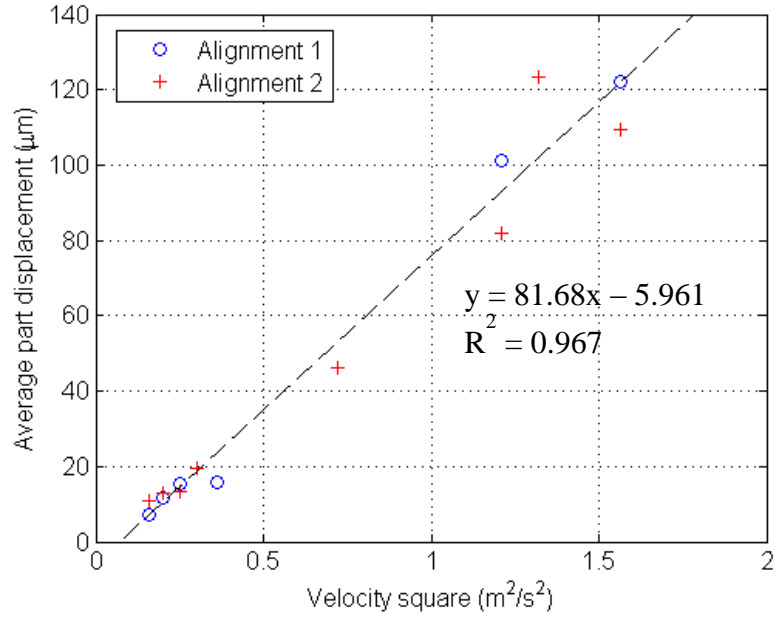


Figure 91. Values from actual TDVKA tables for part 3B on the IC chuck at 3.4 psi.

## Appendix E. **TDVKA tables detailing an algorithm inefficiency**

This appendix details inefficiency associated with the alignment algorithm as discussed in Section 5.4.

Table 28. Misalignment table for alignment of part 1A on OC chuck at 5.2 psi.

Measurement No.	Misalignment ( $\mu\text{m}$ )
1	294.3
2	197.9
3	137.4
4	96.3
5	86.1
6	59.4
7	48.2
8	32.9
9	32.0
10	20.8
11	16.8
12	12.1
13	7.83
14	6.69
15	5.14
16	3.26

Table 29. TDVKA table corresponding to test in Table 28.

T	D	V	K	A
Tap No.	Displacement (μm)	Velocity (m/s)	Velocity-square (m <sup>2</sup> /s <sup>2</sup> )	Drop angle (deg)
1	192.65	0.90	0.810	41.8
1	166.54	0.85	0.723	22.6
1	138.38	0.80	0.640	28.0
1	123.28	0.75	0.563	39.3
1	102.4	0.70	0.490	41.3
1	80.09	0.60	0.360	29.0
1	50.50	0.50	0.250	44.4
1	46.02	0.45	0.203	29.9
1	34.96	0.40	0.160	38.5
1	26.56	0.35	0.123	27.0
1	16.27	0.30	0.090	20.4
3	9.18	0.25	0.063	35.7

## Appendix F. Energy balance equations for part motion

This appendix details an energy balance approach to understanding part motion as it yields useful results, particularly for use in the alignment algorithm that determines how hard to tap the part to move it a desired distance. In the energy balance model, the impact between the impacting mass and the part is assumed to be instantaneous. Figure 92 describes the three key events in this model.

At Time 1, the impacting mass and part begin just in contact, with the part stationary ( $v_{p1} = 0$ ) and the impacting mass (with mass  $m_t$ ) moving into the part at a velocity  $v_{t1}$ . Just after impact, at Time 2, the impacting mass is moving in the opposite direction at a velocity  $v_{t2}$  and the part begins moving at a velocity  $v_{p2}$  as a result of the impact. Finally, at Time 3, the part has ceased sliding after traveling a distance  $\delta$  while being resisted by the nominal friction force  $F_f$ .

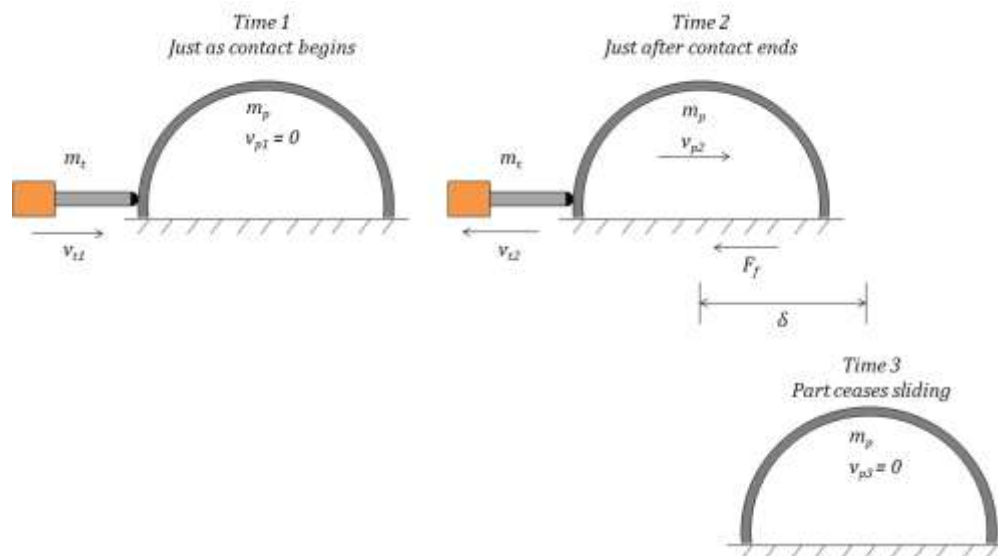


Figure 92. Energy balance and instantaneous impact model.

Equations (47) and (48) are used to determine the initial velocity prescribed to the part at time 2. Equation (47) is a conservation of momentum expression. Equation (48) defines the coefficient of restitution  $e$  as a function of the velocities of the impacting bodies just before and just after impact.

$$m_t v_{t1} + m_p v_{p1} = m_t v_{t2} + m_p v_{p2} \quad (47)$$

$$e = \frac{v_{p2} - v_{t2}}{v_{t1} - v_{p1}} \quad (48)$$

Equations (47) and (48) can be combined into Equation (49) to yield an expression for the initial sliding velocity of the part  $v_{p2}$  in terms of parameters typically known for an impact.

$$v_{p2} = \frac{(1 + e)m_t v_{t1}}{m_t + m_p} \quad (49)$$

The part will continue to slide at the velocity  $v_{p2}$  unless an external force acts on it. Equation (50) shows an energy balance used to describe the motion of part that has an initial velocity  $v_{p2}$ . The variable  $T$  represents the total energy of the part and the variable  $U$  represents the work done on the part between time 2 and 3. In this example, time 2 is just after impact (as seen in Figure 92) and time 3 is when the part comes to a rest due to friction, thus  $\sum T_3 = 0$ .

$$\sum T_2 + U_{2-3} = \sum T_3 \quad (50)$$

The work done on the part  $U_{2-3}$  is the product of a nominal resistive friction force  $F_f$  and part sliding distance  $\delta$ . Thus, Equation (50) yields:

$$F_f \delta = \frac{1}{2} m_p (v_{p2})^2 \quad (51)$$

One more substitution yields a direct relation between impacting velocity of the impacting mass and part displacement. The expression for  $v_{p2}$  in Equation (49) can be substituted into Equation (51) and the result solved for  $\delta$  yielding Equation (52) which defines the part sliding distance in terms of the key impact parameters.

$$\delta = \frac{m_p(1+e)^2 m_t^2 v_{t1}^2}{2F_f(m_t + m_p)^2} \quad (52)$$

The result in Equation (52) shows two important facts.

- 1) The part sliding distance is not directly proportional to the initial kinetic energy of the impacting mass. In fact, for a given realistic kinetic energy of the impacting mass, the part will displace further if the impacting mass is increased and the impacting velocity is decreased accordingly to maintain the same kinetic energy. As will be described in Section 2.2.2, this result is useful for selecting the appropriate size for the Thumper II impacting mass.
- 2) The part sliding distance is linearly related to the square of the impacting mass initial velocity. This is a useful result for selecting the impact velocity to correct a workpiece position error as stated in Equation (53).

$$\delta \sim v_{t1}^2 \quad (53)$$

## Appendix G. Summary of components for Thumper II

Table 30. List of components used for Thumper II.

Component	Manufacturer (Part No.)	Notes
Voice coil actuator	BEI Kimco (LA15-26-000A)	<ul style="list-style-type: none"> <li>• 44.5 peak force</li> <li>• 25.4 mm stroke</li> </ul>
Linear rail	THK (SSR15XV1SSC1M+92LYPMS)	<ul style="list-style-type: none"> <li>• Rail made to a custom length and custom hole positions.</li> </ul>
Encoder readhead	Renishaw (T1001-10A)	<ul style="list-style-type: none"> <li>• RGSZ/N20 readhead</li> </ul>
Encoder interpolator	Renishaw (TI0400A20A)	<ul style="list-style-type: none"> <li>• ToniC 20 MHz interpolator</li> </ul>
Encoder scale	Renishaw (A-9420-0003M)	<ul style="list-style-type: none"> <li>• 30mm long with reference mark in middle</li> <li>• Araldite AV 138M-1/HV 998 adhesive from Renishaw used on ends of scale</li> </ul>
Bellows	McMaster-Carr (9741K43)	<ul style="list-style-type: none"> <li>• This is the “Thermiseal Welded” bellows manufactured by Gortite and sold by McMaster-Carr</li> </ul>
Amplifier (for voice-coil motor)	Advanced Motion Controls (12A8)	<ul style="list-style-type: none"> <li>• DC Supply Voltage Range: 20-80V</li> <li>• DC Overvoltage Limit: 88V</li> <li>• Maximum peak output current: 12A</li> <li>• Maximum continuous output current: 6A</li> <li>• Includes output signal proportional to the load current</li> </ul>
Power supply (for amplifier)	Advanced Motion Controls (PS16L80)	<ul style="list-style-type: none"> <li>• DC Output Voltage: 80V</li> <li>• DC Output Current: 10A</li> <li>• AC supply voltage: 120 V</li> <li>• AC input frequency: 50-60Hz</li> <li>• Maximum continuous output current: 6A</li> </ul>
Microcontroller	TERN (586-Engine-P)	<ul style="list-style-type: none"> <li>• Includes a AC-to-DC power block</li> </ul>
Expansion board for microcontroller	TERN (P50)	<ul style="list-style-type: none"> <li>• Includes quadrature decoders</li> </ul>
Surge protector inside of electrical enclosure	360electrical (36050-011)	<ul style="list-style-type: none"> <li>• Has two power rotatable power outlets</li> </ul>

## Appendix H. **Tables for selection of rail mass**

Table 31 and Table 32 are used together and evaluate the tradeoff described in Section 2.2.2 for selecting the impacting mass. Table 31 shows the effect of increasing the impacting mass on part displacement for a 35 lb part at various vacuum pressures and a stroke of 20 mm. At 0.15 kg impacting mass, the maximum part displacement at 20 mm stroke for the selected VCA at 10 psi is 121  $\mu\text{m}$ . If the initial runout is 1.25 mm, then it would take about 10 taps to get the part nearly centered. This is not an unreasonable number of taps, and thus it is concluded that it is possible to achieved large enough displacements with a 0.15 kg (and larger) impacting mass.

Table 32 shows the effect of increasing the impacting mass on velocity sensitivity for a 5 lb part. For the 0.35 kg mass in Table 32, an impact velocity of 0.240 m/s yields 4.0  $\mu\text{m}$  of part displacement and an impact velocity of 0.214 yields 0.5  $\mu\text{m}$  of part displacement. This is a velocity change of only 0.026 m/s. For the same values of part displacement, a 0.15 kg mass would need a velocity change of 0.081 m/s. Thus, Table 32 shows that adding mass to the linear rail to make it 0.35 kg could have undesirable results. The small velocity sensitivity (0.026 m/s between the velocities to achieve 0.5  $\mu\text{m}$  and 4.0  $\mu\text{m}$ ) suggests that a lighter impacting mass is more desirable.

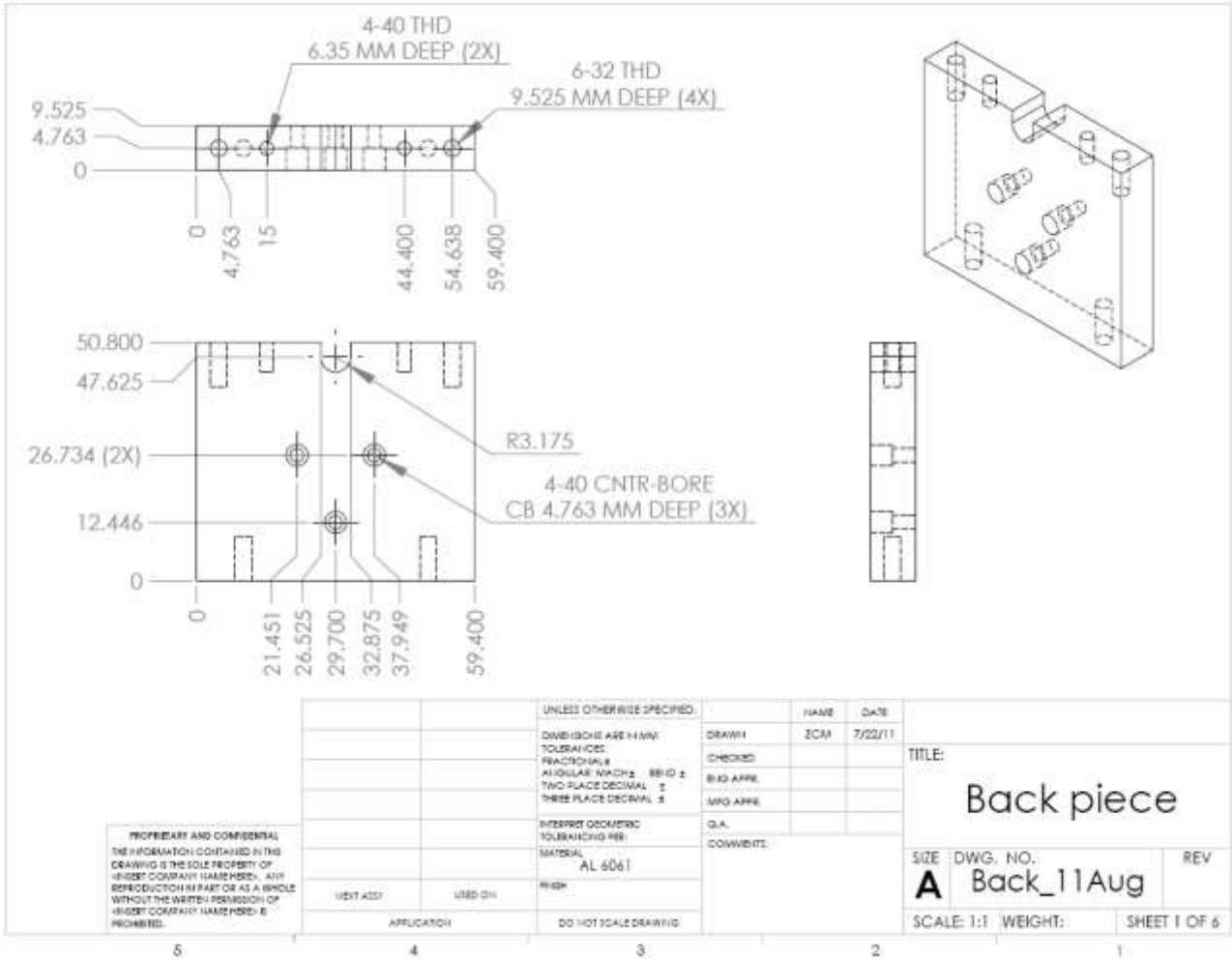
Table 31. Selection of impacting mass: increasing mass increases part displacement.

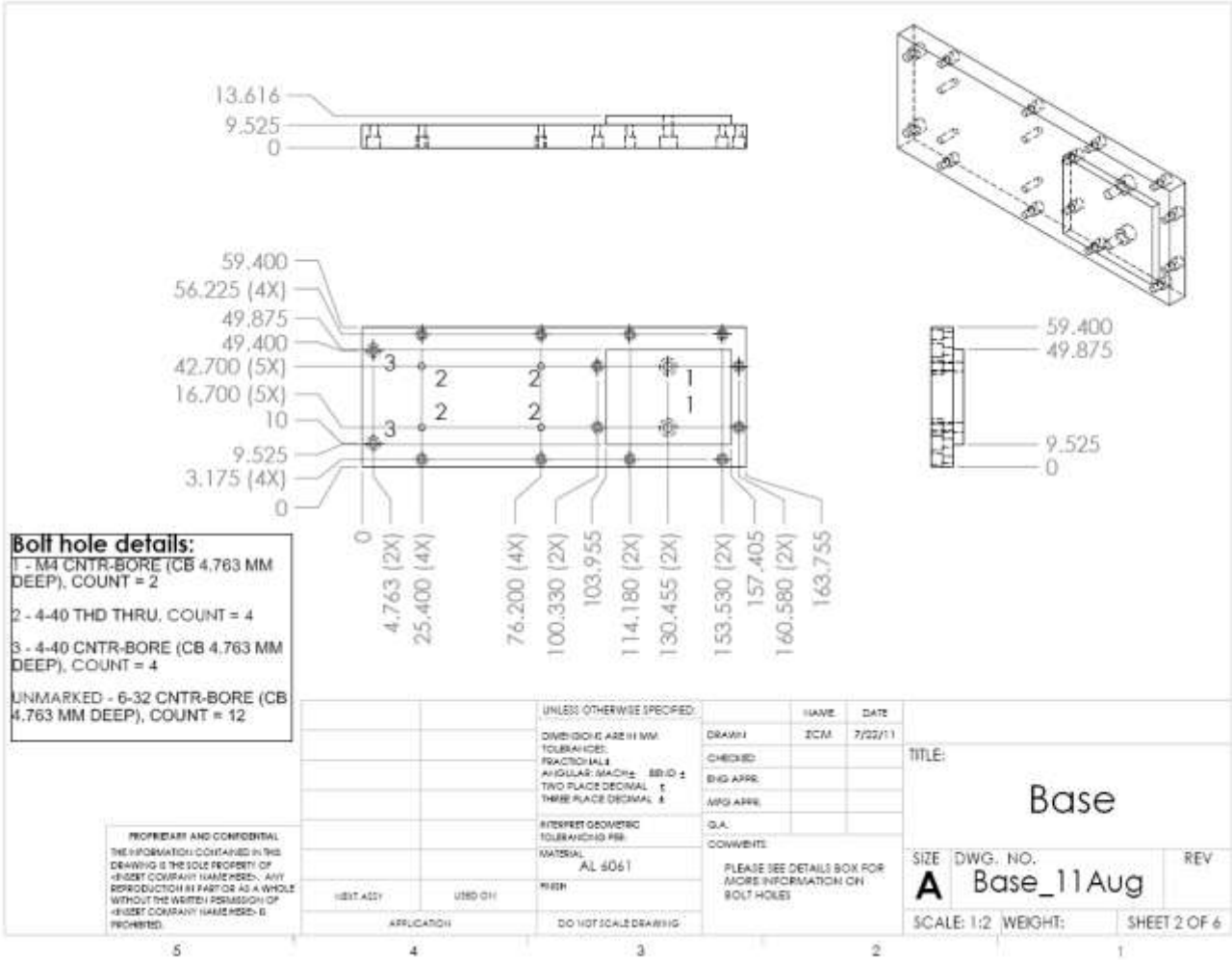
Impacting mass (kg)	Part weight (lb)	Vacuum (psi)	Max disp. with 20 mm stroke ( $\mu\text{m}$ )
0.15	35	7.50	162
		10.0	121
		12.5	97
0.25	35	7.50	268
		10.0	201
		12.5	161
0.35	35	7.50	370
		10.0	277
		12.5	222

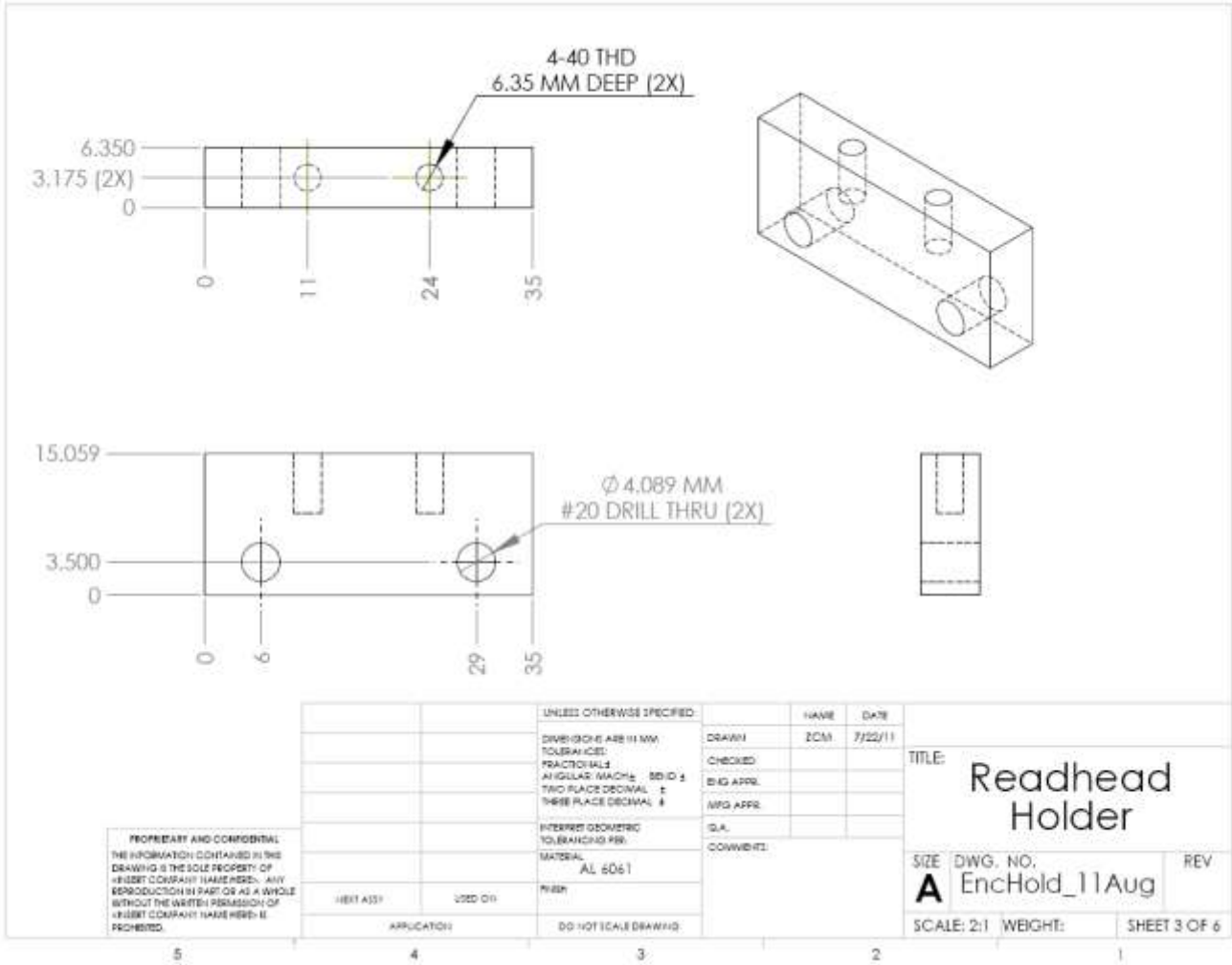
Table 32. Selection of impacting mass: decreasing mass improves velocity resolution.

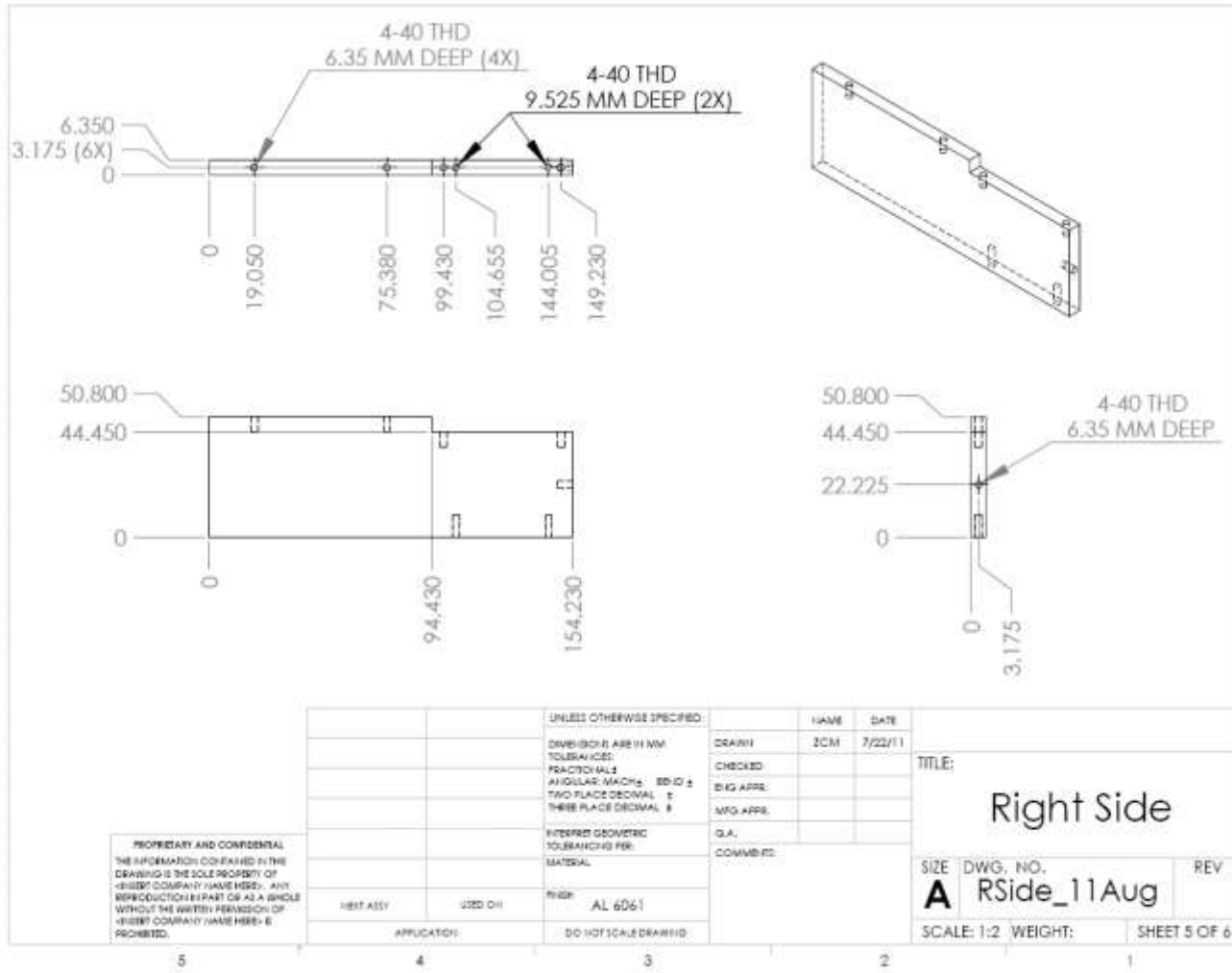
Impacting mass (kg)	Part weight (lb)	Vacuum (psi)	Displacement ( $\mu\text{m}$ )	Velocity (m/s)	Velocity (m/s)
0.15	5	7.50	0.5	0.338	
		7.50	4.0	0.418	0.081
		7.50	6.0	0.454	0.036
		10.0	0.5	0.423	
		10.0	4.0	0.511	0.088
		10.0	6.0	0.552	0.041
0.25	5	7.50	0.5	0.256	
		7.50	4.0	0.297	0.042
		7.50	6.0	0.318	0.020
		10.0	0.5	0.322	
		10.0	4.0	0.367	0.045
		10.0	6.0	0.389	0.023
0.35	5	7.50	0.5	0.214	
		7.50	4.0	0.240	0.026
		7.50	6.0	0.254	0.014
		10.0	0.5	0.270	
		10.0	4.0	0.297	0.027
		10.0	6.0	0.313	0.015

Appendix I. **Shop drawings for Thumper II structure**





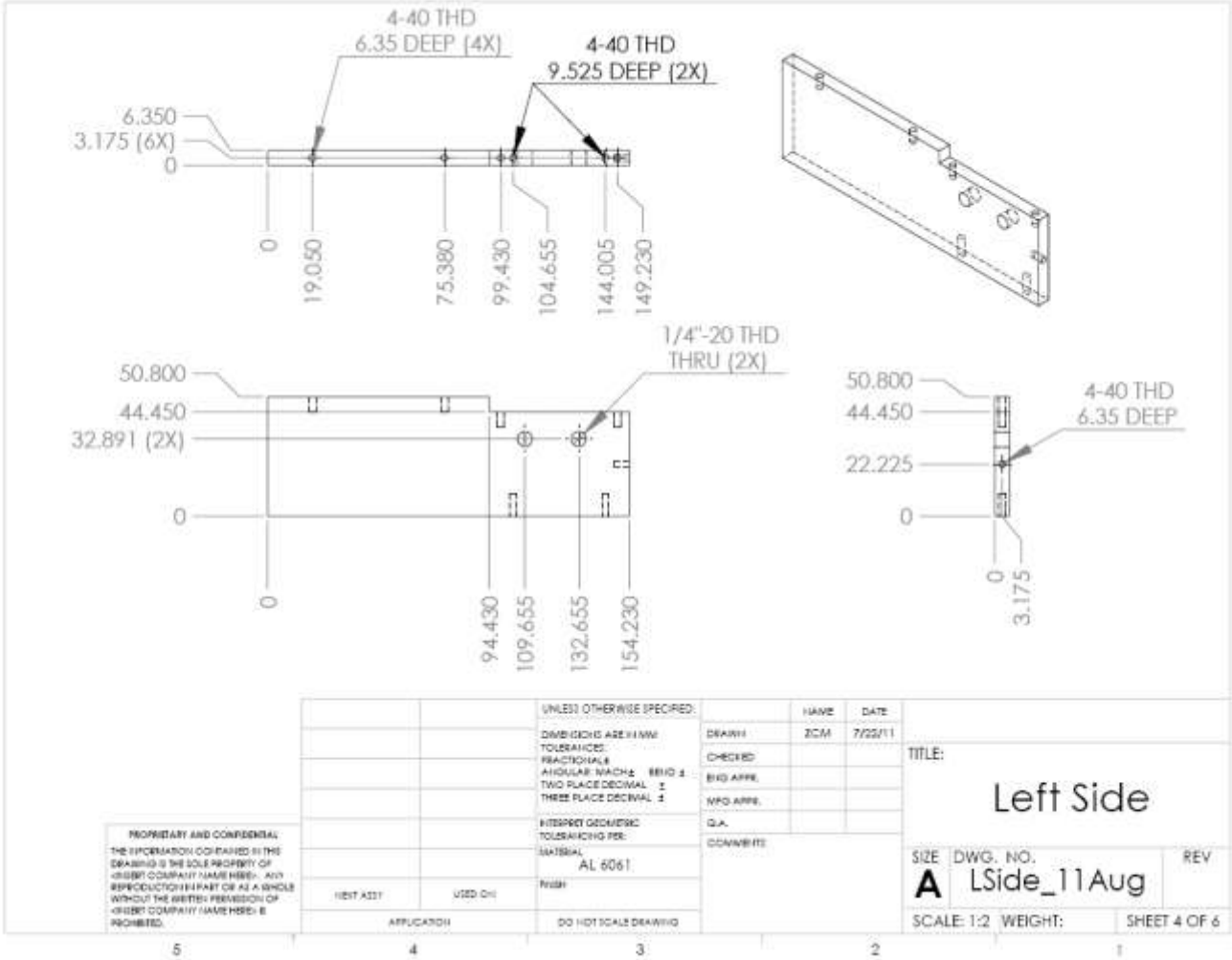


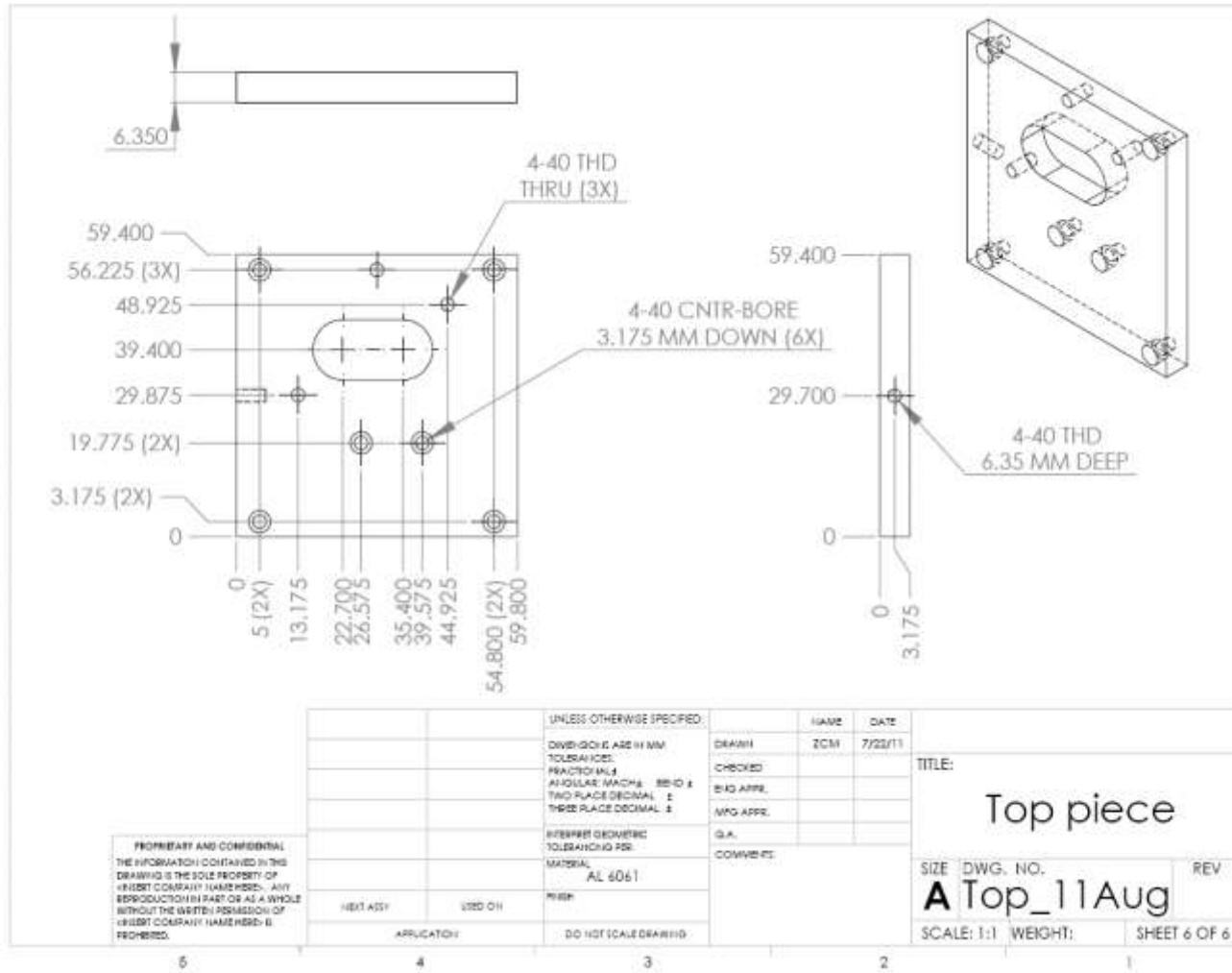


PROPRIETARY AND CONFIDENTIAL  
 THE INFORMATION CONTAINED IN THIS  
 DRAWING IS THE SOLE PROPERTY OF  
 [INSERT COMPANY NAME HERE]. ANY  
 REPRODUCTION IN PART OR AS A WHOLE  
 WITHOUT THE WRITTEN PERMISSION OF  
 [INSERT COMPANY NAME HERE] IS  
 PROHIBITED.

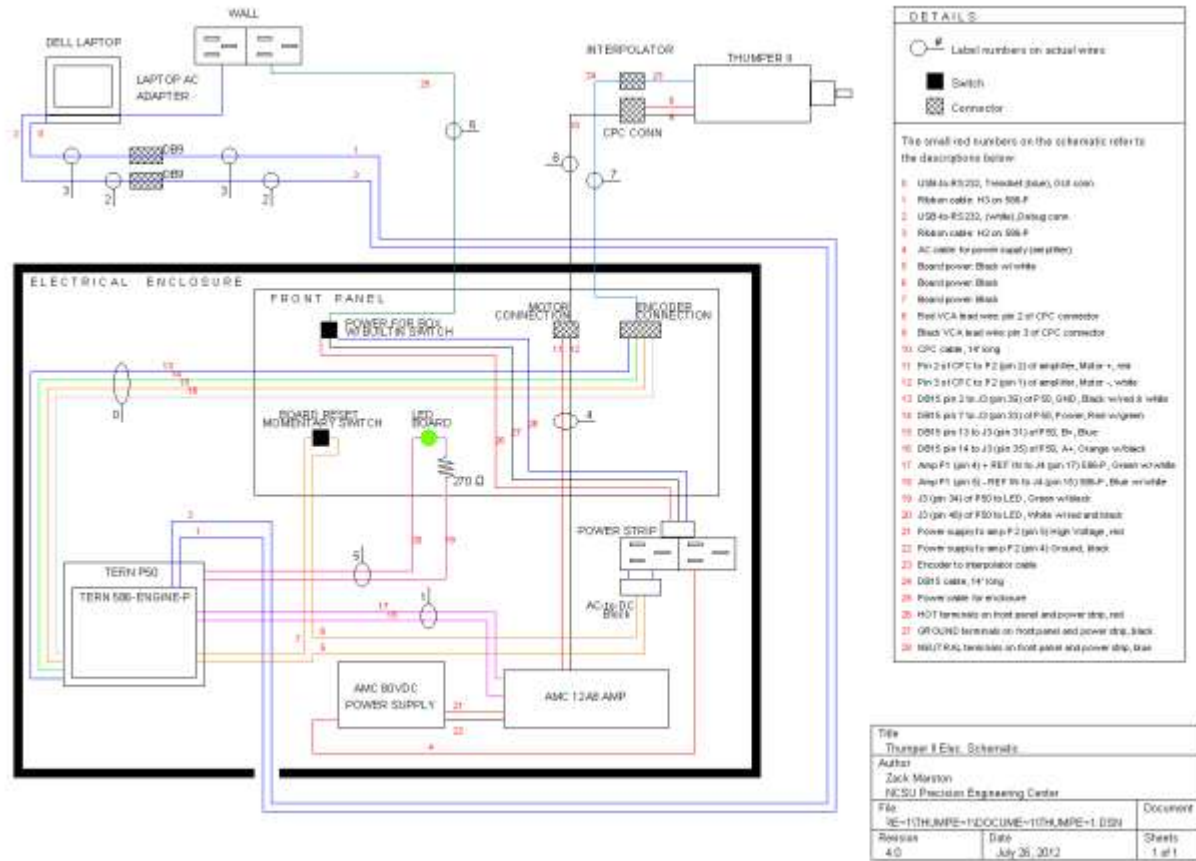
UNLESS OTHERWISE SPECIFIED:		NAME	DATE
DIMENSIONS ARE IN MM	TOLERANCES:	DRAWN	ECM
FRACTIONAL	ANGULAR: MAXIMUM ±	CHECKED	
TWO PLACE DECIMAL	TWO PLACE DECIMAL	ENG APPR.	
THREE PLACE DECIMAL	INTERPRET GEOMETRIC TOLERANCING PER MATERIAL	MFG APPR.	
		Q.A.	
		COMMENTS:	
SHEET ASSY	USED ON		
APPLICATION:	DO NOT SCALE DRAWING		

TITLE:		
Right Side		
SIZE	DWG. NO.	REV
A	RSide_11Aug	
SCALE: 1:2	WEIGHT:	SHEET 5 OF 6

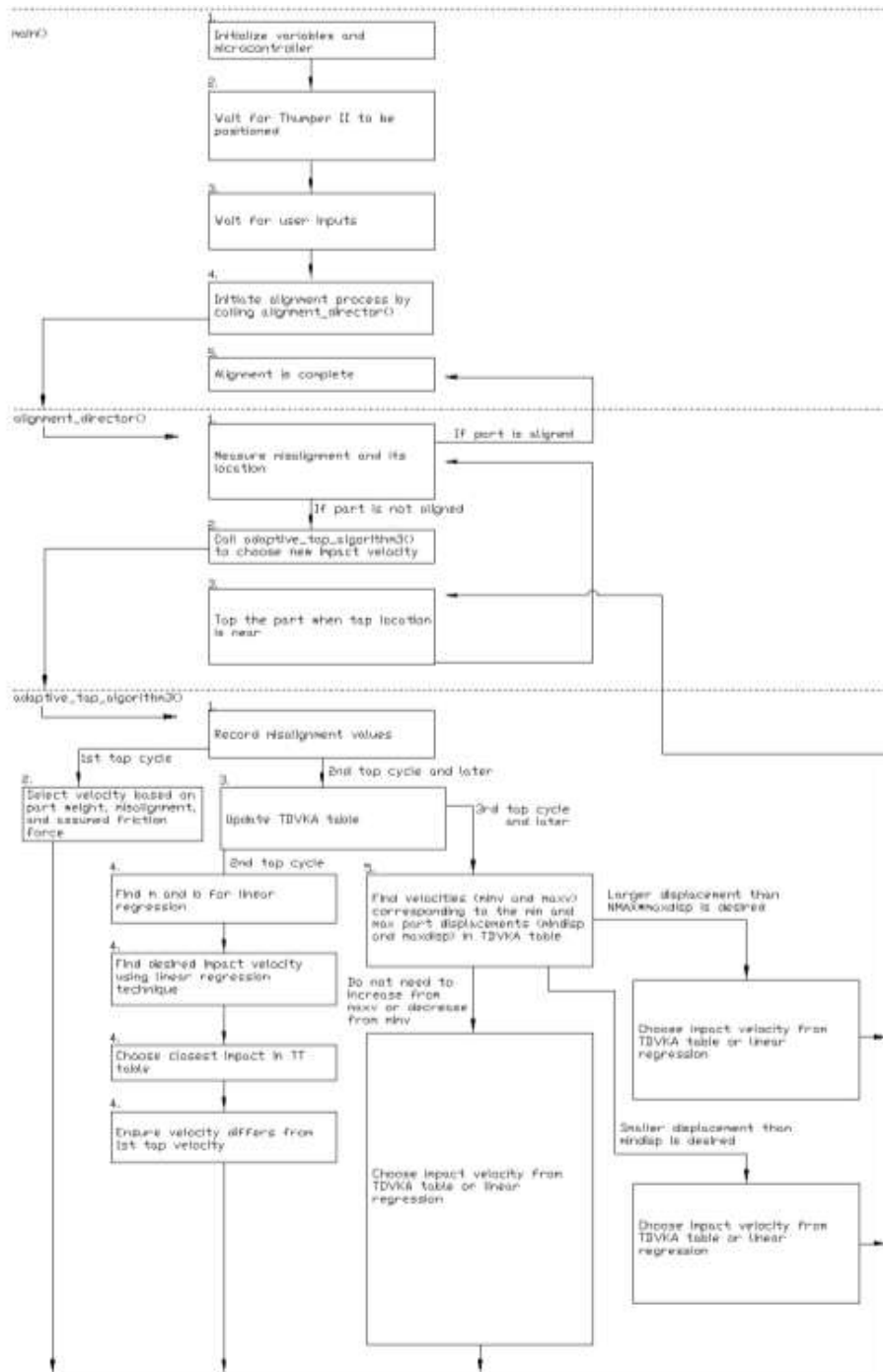


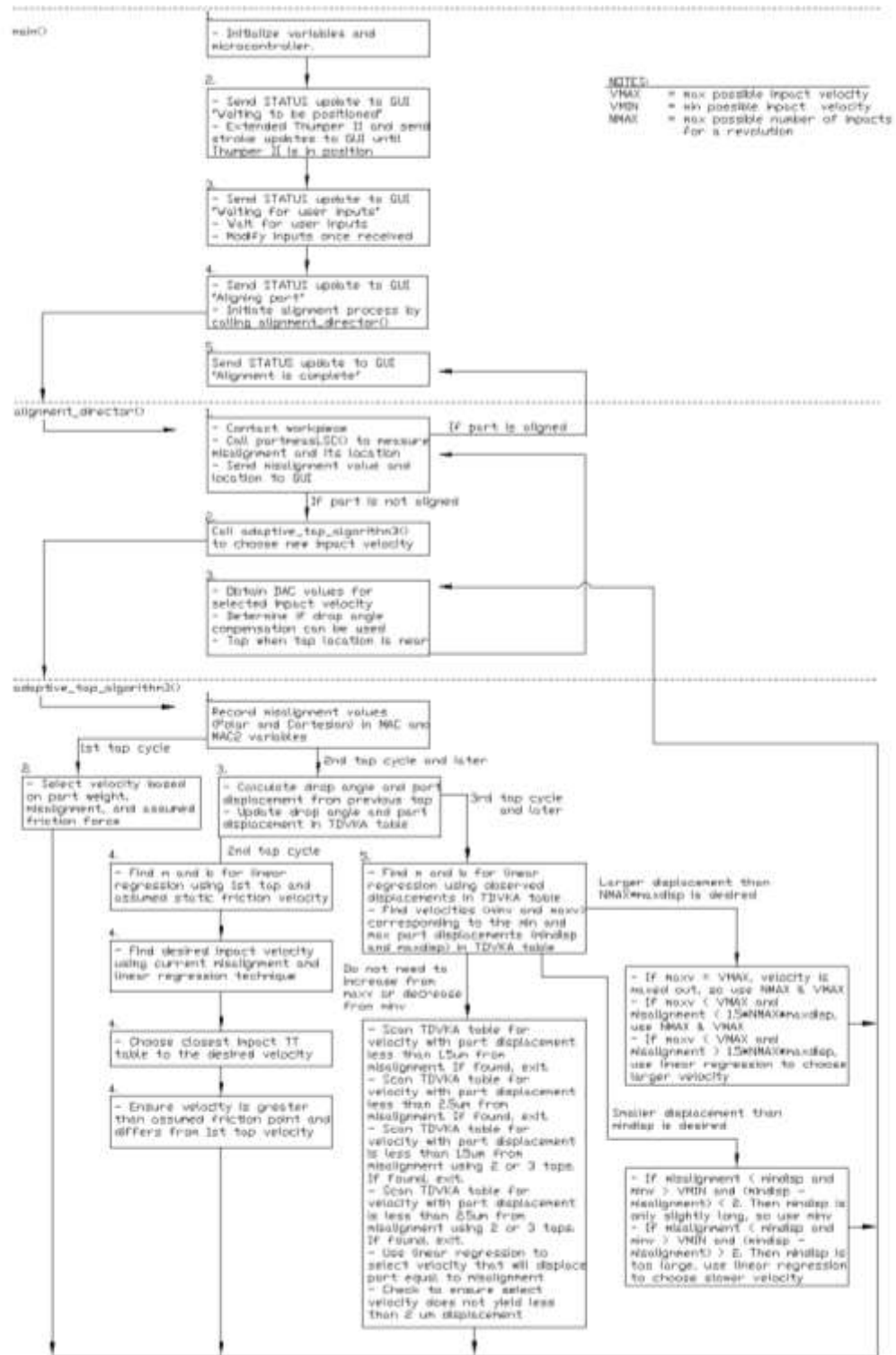


## Appendix J. Electrical schematic for electrical enclosure



## Appendix K. Code & Adaptive Algorithm Flow Chart





## Appendix L. Operate Thumper II (from User's Manual)

This section explains how to set-up and use Thumper II. Figure 93 shows Thumper II installed on a 2-axis lathe. The radial and axial axes can move in this machine.



Figure 93. Thumper II setup.

The following steps should be completed before beginning part alignment and running the GUI.

1. Thumper II should be fully assembled as seen above.
2. Thumper II should be securely mounted in the machine as seen in Figure 93.
3. For radial runout, seen in Figure 93 (a), the vertical location and axial location of the device can be set visually. For radial runout, the radial location of Thumper II will be set with the aid of the GUI.
4. For axial runout, seen in Figure 93 (b), the vertical location and radial location of the device can be set visually. For axial runout, the axial location of Thumper II will be set with the aid of the GUI.
5. Ensure all electrical connections are in place as described.

6. The electrical enclosure should be switched on and the LED on the front panel should be green.
7. The GUI should be loaded by clicking the program on the desktop called “ThumperII\_GUI” having the following icon: 
8. The steps for using the GUI should be completed as described with Figure 94 – Figure 98.

The GUI can be started by selecting the shortcut on the desktop called “”. Figure 94 – Figure 98 illustrate how to properly use GUI.

The five possible statuses for the GUI are:

1. Searching for controller connection
2. Waiting to be positioned
3. Waiting for operator input
4. Aligning part
5. Part alignment complete

The GUI is ready to begin operation when the screen in Figure 94 is seen. The two important sections of the GUI for this step are outlined in red. The current status should be “Waiting to be positioned”. If the status is “Waiting for controller connection” then the board should be turned on or reset. It will be necessary to restart the GUI and reset the microcontroller using the front panel on the electrical enclosure if runout values are in the GUI from a previous alignment.

**To complete this step, the user must jog the axis such that the Thumper II stroke value is  $20\text{ mm} \pm 0.25\text{ mm}$ .** The ‘Position Thumper II’ box shows the stroke and how far the device should be moved. This step can be skipped by checking the box ‘Skip positioning procedure’. Skipping this procedure if the device is in an invalid place could result in the device not working.

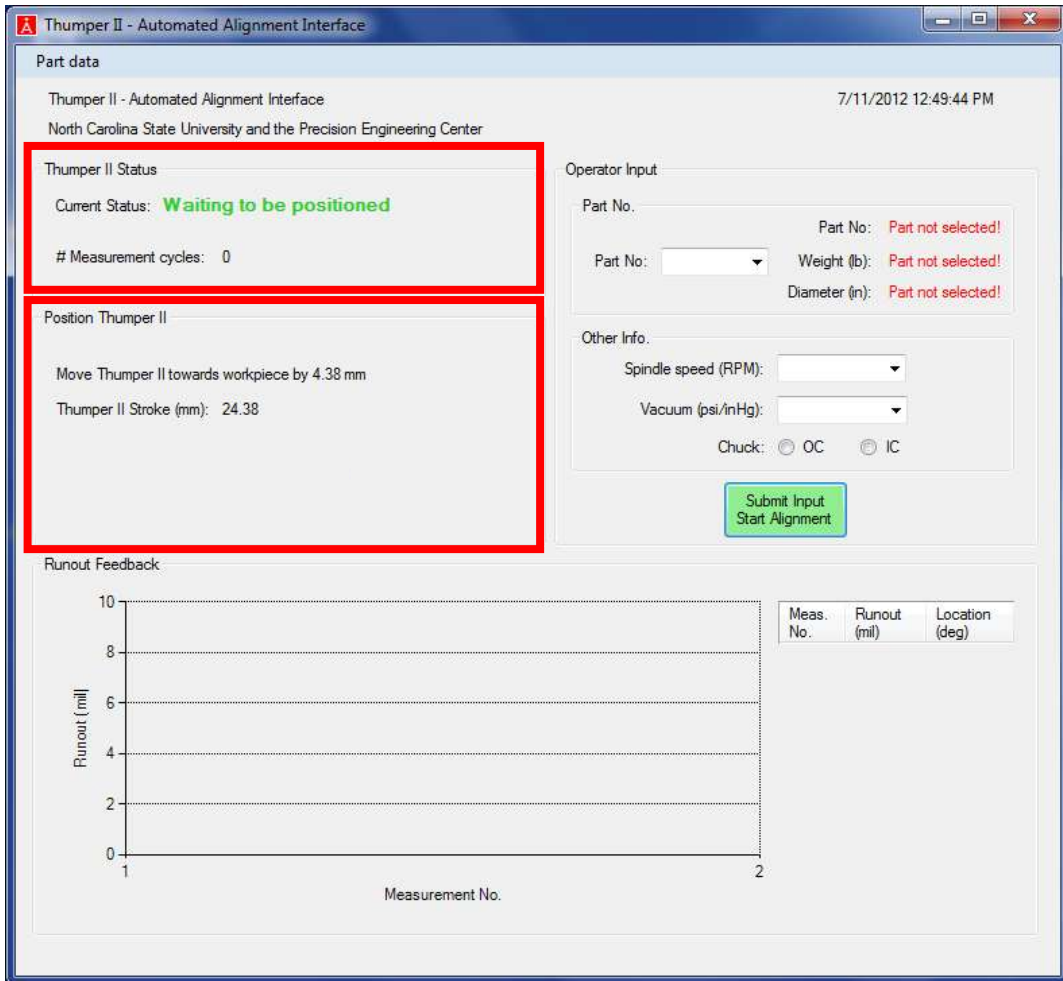


Figure 94. GUI Step 1.

After the device has been moved into position the screen in Figure 95 should be present. A message box indicating the device is in position will pop-up. Also, the status will change to “Waiting for operator input”.

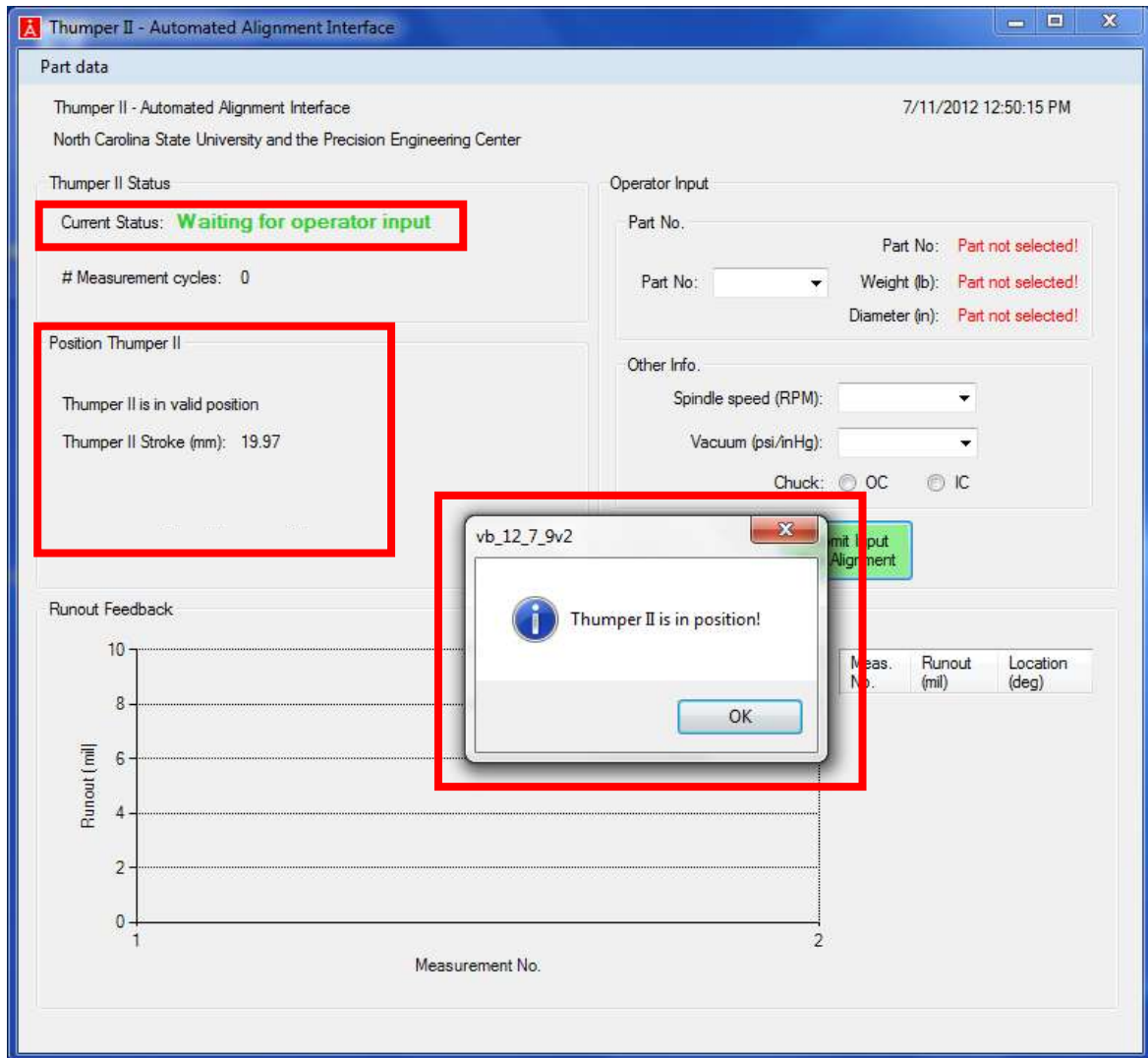


Figure 95. GUI Step 2.

Once Thumper II is properly positioned and the message box is clicked, the screen in Figure 96 will be present. **At this point, the operator must input four values for the microcontroller to use: spindle speed, part number, vacuum pressure, and chuck.**

The spindle speed must be a whole number between 1 and 16. The vacuum pressure must be selected from the values in the drop-down box as well as the part number. Once these values are properly entered, clicking on the green button 'Submit Input Start Alignment' will begin the alignment process.

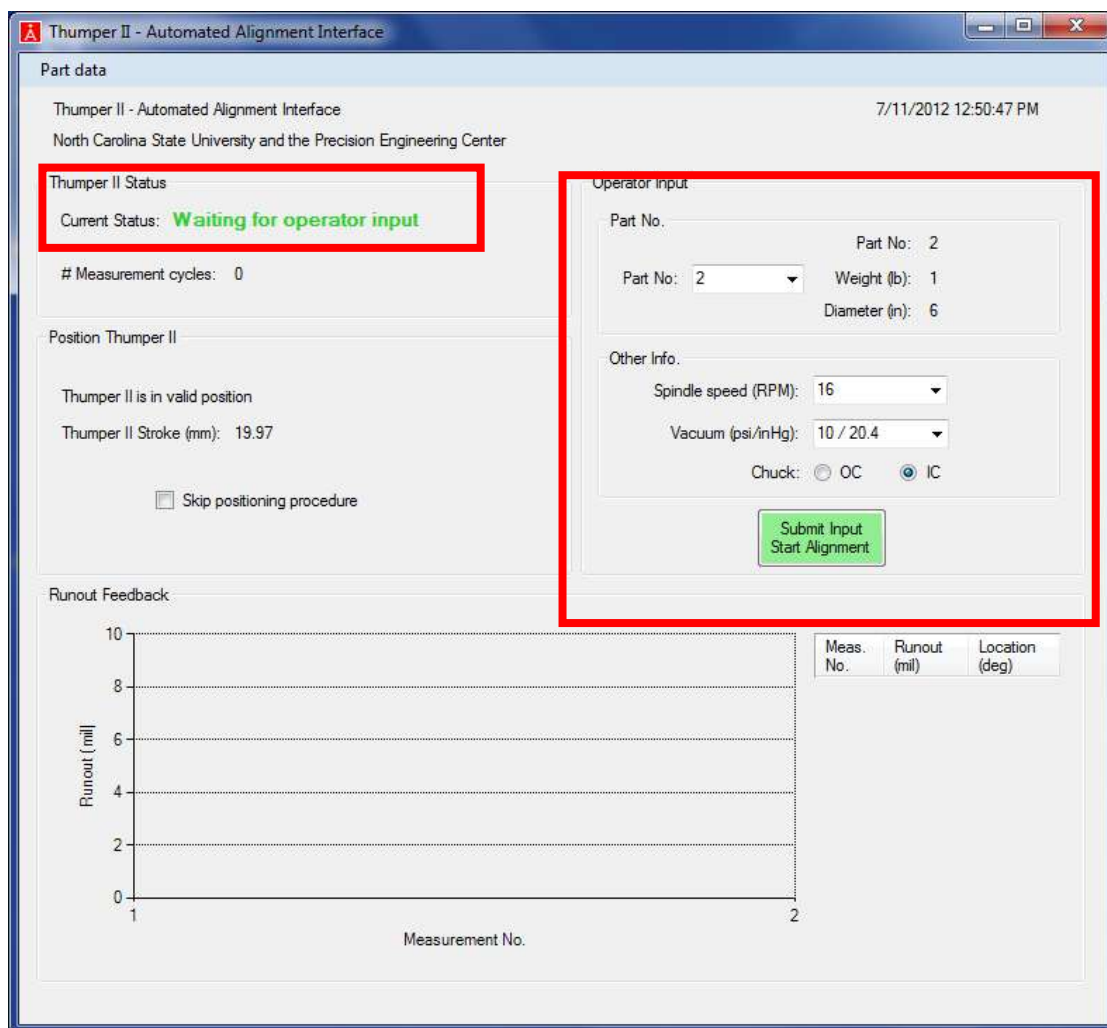


Figure 96. GUI Step 3.

Once the operator successfully submits the inputs, the status will change to ‘Aligning part’ and the screen will look as in Figure 97 but with different runout values. **The operator’s work with Thumper II is done and the values in the ‘Runout Feedback’ section will be updated for each new measurement** (about once every 8–10 seconds for 16 RPM spindle speed). The target runout for Thumper II is 5 micrometers, or 0.20 mils. Thus, values for runout will update automatically until this target is reached.

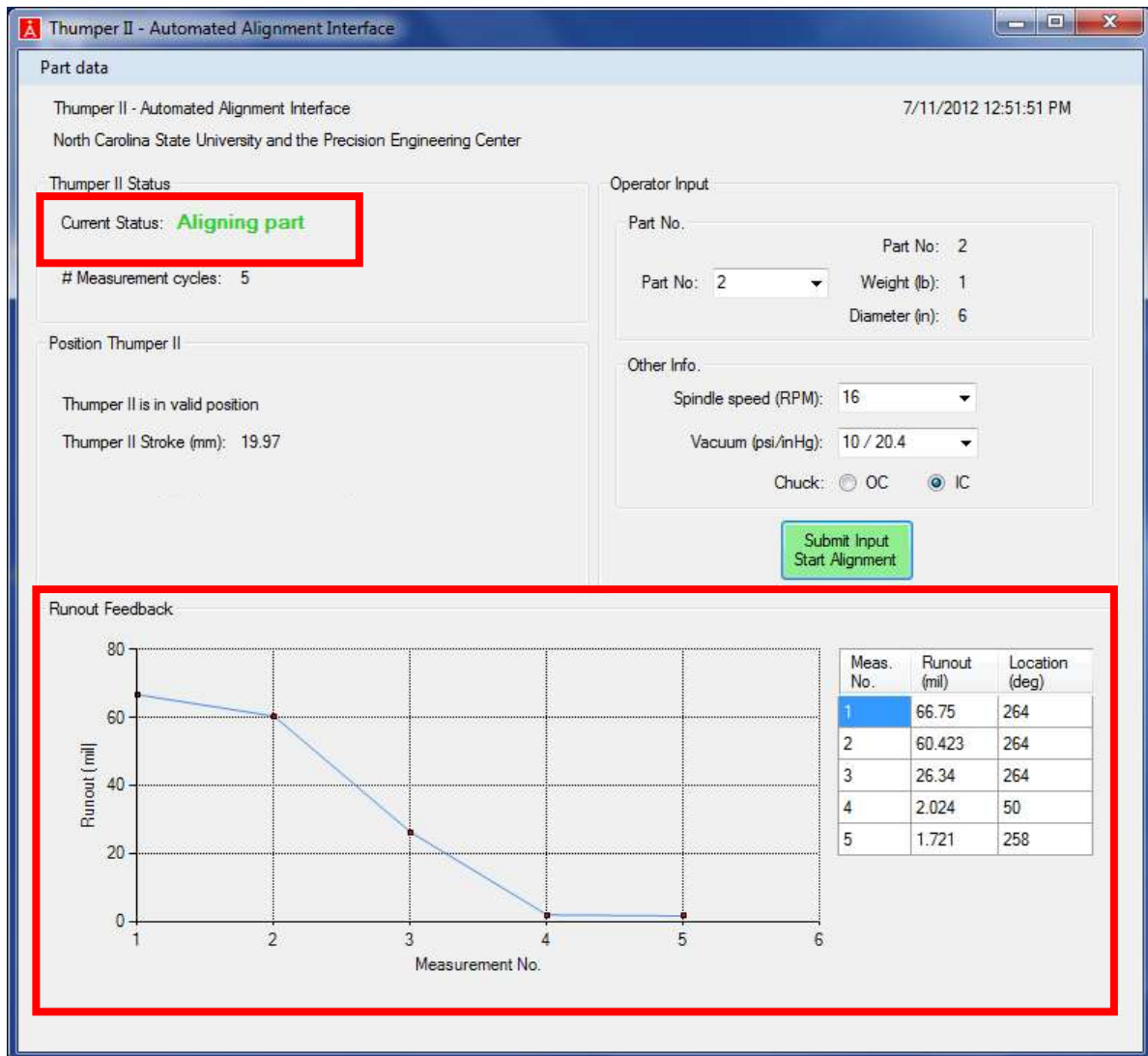


Figure 97. GUI Step 4.

Once the runout target is less than 5 micrometer (or 0.20 mil), the screen seen in Figure 98 will appear indicating the part alignment process is complete. To align another part, it will be necessary restart the GUI and reset the microcontroller using the front panel on the electrical enclosure.

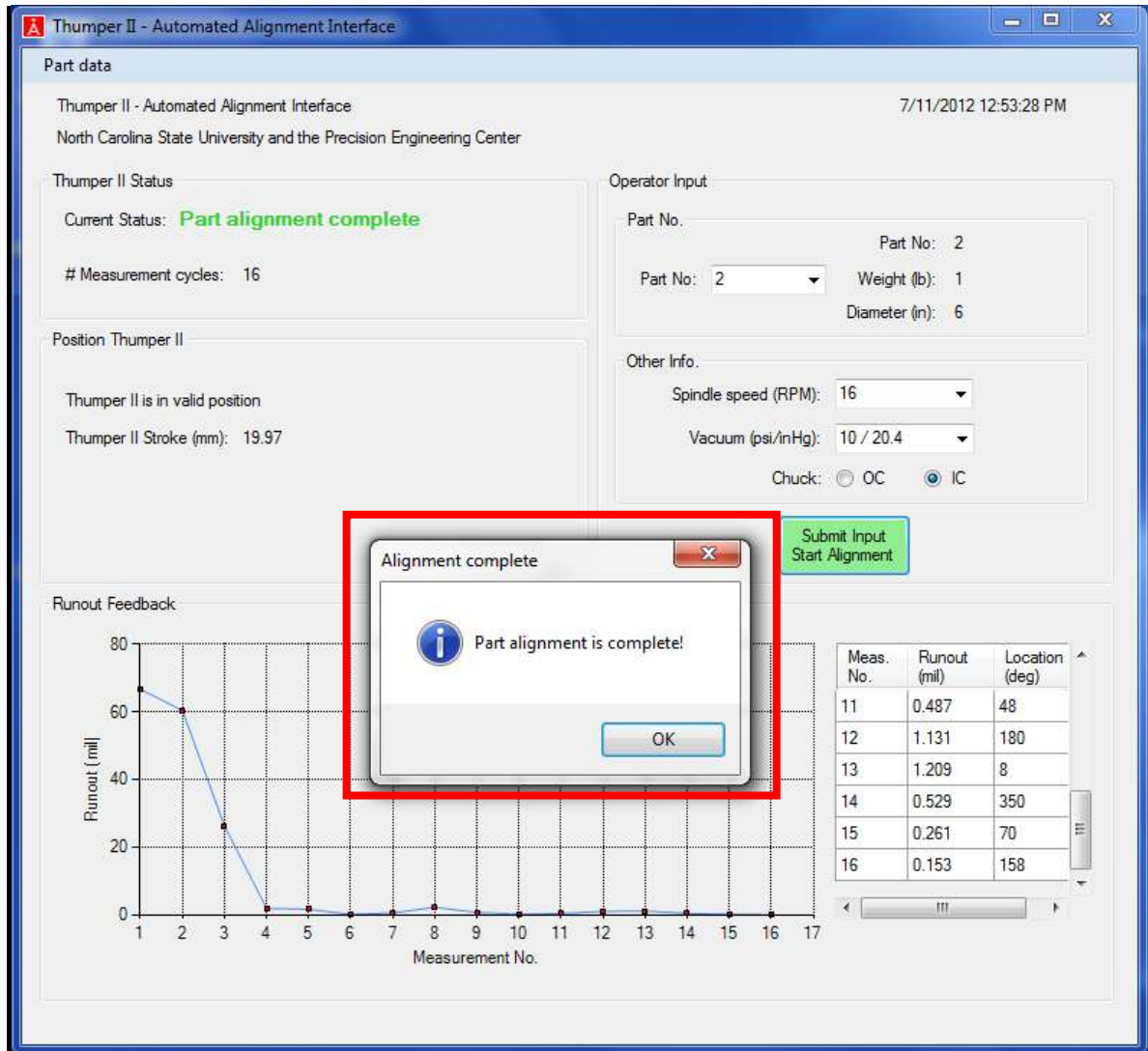


Figure 98. GUI Step 5.